

**HIGH-AMPLITUDE, ULTRASHORT STRAIN
SOLITONS IN SOLIDS**



Universiteit Utrecht

HIGH-AMPLITUDE, ULTRASHORT STRAIN SOLITONS IN SOLIDS

INTENSE, ULTRAKORTE DRUK-SOLITONEN IN VASTE STOFFEN

(met een samenvatting in het Nederlands)

PROEFSCHRIFT

TER VERKRIJGING VAN DE GRAAD VAN DOCTOR AAN
DE UNIVERSITEIT UTRECHT OP GEZAG VAN DE RECTOR
MAGNIFICUS, PROF. DR. W. H. GISPEN, INGEVOLGE
HET BESLUIT VAN HET COLLEGE VOOR PROMOTIES
IN HET OPENBAAR TE VERDEDIGEN OP MAANDAG
22 MAART 2004 DES MIDDAGS TE 16.15 UUR

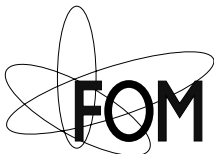
DOOR

Otto Lambert Muskens

GEBOREN OP 3 FEBRUARI 1977 TE WINTERSWIJK

PROMOTOR: PROF. DR. J. I. DIJKHUIS

FACULTEIT DER NATUUR- EN STERRENKUNDE
UNIVERSITEIT UTRECHT



The work described in this thesis was supported by the “Stichting voor Fundamenteel Onderzoek der Materie (FOM)”, which is financially supported by the “Nederlandse Organisatie voor Wetenschappelijk Onderzoek (NWO)”.

CIP-DATA KONINKLIJKE BIBLIOTHEEK, DEN HAAG

Muskens, Otto Lambert

HIGH-AMPLITUDE, ULTRASHORT STRAIN
SOLITONS IN SOLIDS

Otto Lambert Muskens – Utrecht: Universiteit Utrecht,
Faculteit der Natuur- en Sterrenkunde

Thesis Universiteit Utrecht – with a summary in Dutch
ISBN 90-393-3627-X

CONTENTS

1	Introduction	11
1.1	Historical perspective	11
1.2	Picosecond Ultrasonics	13
1.3	Scope and outline of this thesis	16
	Bibliography	19
2	Theory of strain solitons	21
2.1	Introduction	21
2.2	Nonlinear elasticity theory	22
2.2.1	General formulation	22
2.2.2	Reduction to single dimension	25
2.3	Microscopic model	27
2.4	The KdV initial-value problem	28
2.4.1	Single-soliton solution	29
2.4.2	Multi-soliton solutions	30
2.5	Shock-wave development	34
	Bibliography	35
3	Detection of modelocked strain wavepackets by Brillouin scattering	37
3.1	Introduction	37
3.2	Experimental details	39
3.3	Experiments in lead molybdate	40
3.3.1	Acoustic power spectrum	40
3.3.2	Spectral mode-structure	40
3.3.3	Relation between spatial and spectral width	43
3.3.4	Propagation of a single strain component	46

3.4	Conclusions	48
	Bibliography	48
4	High-amplitude, ultrashort, longitudinal strain solitons in sapphire	49
4.1	Introduction	49
4.2	Experimental setup	50
4.3	Numerical simulations	51
4.4	Experiments at a single strain component	52
4.4.1	Propagation at room temperature	52
4.4.2	Temperature dependence	53
4.4.3	Propagation at low temperature	54
4.5	Interpretation	55
4.6	Conclusions	57
	Bibliography	58
5	Inelastic light scattering by soliton trains in sapphire	59
5.1	Introduction	59
5.2	General observations	60
5.2.1	Polarization dependence	60
5.2.2	Strain calibration	61
5.3	Experiments at different frequency components	61
5.4	Discussion	62
5.5	Development of the soliton spectrum	65
5.6	Conclusions	70
	Bibliography	70
6	Coherent interactions of terahertz strain solitons and electronic two-level systems in photoexcited ruby	71
6.1	Introduction	71
6.2	Experiments along the a axis	72
6.2.1	Detection in crystal	73
6.2.2	Propagation through an additional excited zone	74
6.2.3	Propagation through a collinear zone	75
6.3	Coherent, impulsive interaction model	76
6.4	Conclusions	80
	Bibliography	80

7	Strain solitons and the 29-cm⁻¹ ruby phonon spectrometer	83
7.1	Introduction	83
7.2	Theory of spectral-hole refilling	84
7.3	Experiments along the <i>c</i> axis	89
7.3.1	Method	89
7.3.2	Detection at endface	89
7.3.3	Discussion	91
7.4	Properties of the soliton-TLS interaction	93
7.4.1	Magnetic field dependence	94
7.4.2	<i>N</i> * and pump-power dependence	96
7.4.3	Discussion	98
7.5	Conclusions and prospects	101
	Bibliography	101
8	Ultrafast pump-probe reflectometry of strain wavepackets	103
8.1	Introduction	103
8.2	Theory of ultrafast elasto-optic strain detection	104
8.3	Experimental setup	105
8.3.1	Introduction	105
8.3.2	Principle of operation	107
8.3.3	Setup	109
8.3.4	System performance	111
8.4	Experiments	112
8.4.1	Characterization of strain pulses	112
8.5	Conclusions and Prospects	117
	Bibliography	118
A	Numerical modelling of the KdV-Burgers equation	119
A.1	Introduction	119
A.2	Constant volume method, three-level time scheme	120
A.3	Fourth-order composite Runge-Kutta algorithm	122
A.4	Simulated wavepacket propagation in sapphire	124
	Bibliography	125
B	Transition matrix element of the ruby spectrometer	127
B.1	Introduction	127
B.2	Ligand field calculation	128

B.3 Resonant phonon mean-free path	132
Bibliography	133
C Estimates for the role of the rarefaction tail	135
C.1 Introduction	135
C.2 Brillouin scattering contributions	135
C.3 TLS-excitation by the dispersive tail	137
Bibliography	139
Samenvatting	141
Dankwoord	145
Publications and Conference Visits	149
Curriculum Vitae	151

CHAPTER 1

INTRODUCTION

Abstract

We introduce the field of picosecond ultrasonics, sketch its development and explain the underlying principle of operation. The application of short strain packets is addressed in diverse research areas such as semiconductor technology, nano-imaging, and fundamental condensed-matter physics. A new and unconventional way to generate and detect coherent, longitudinal acoustic wavepackets of high amplitude and with terahertz-frequency components is presented and will be the topic of this thesis.

1.1 Historical perspective

Ever since the early days of mankind, short strain pulses have been used to mold and characterize condensed matter [1]. Starting with pieces of stone, craftsmanship readily evolved with the discovery of metals and alloys, which allowed for plastic deformations without losing their internal strength. The products of this evolution can still be admired in museums all over the world. On the other hand, materials characterization by simply tapping has evolved into a wide range of sophisticated echoscopic methods, that find their application in fields as diverse as seismology, underwater navigation, medicine, and nondestructive testing [2, 3].

The spectrum of sound waves covers a window of over 15 orders of magnitude. Figure 1.1 shows this acoustic frequency spectrum together with some important applications in technology and everyday life. As the acoustic frequency scales up, the corresponding wavelength shifts down to regimes that are of interest for modern technological applications. Next to the separation in frequency, one can distinguish sources of sound by their degree of coherence. Similar to the difference between a laser and a light bulb in optics, a coherent packet of sound

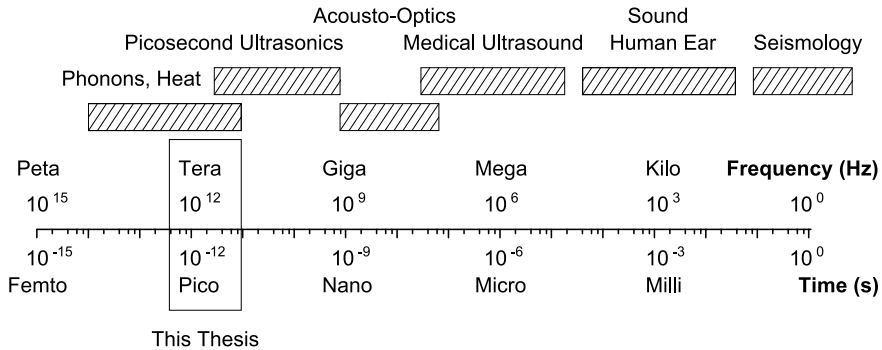


FIGURE 1.1 Acoustic-wave spectrum between 10^0 and 10^{15} Hz, with corresponding time scale in seconds. Shaded blocks denote the typical application windows of sound waves in technology and everyday life. Rectangle denotes the frequency range of the picosecond acoustic pulses that form the topic of this thesis.

will have properties that are fundamentally different from an incoherent spectrum of vibrations. In this thesis we will limit ourselves to the generation mechanisms for coherent longitudinal acoustic waves, and more specifically the formation of short, stable acoustic pulses.

For many years, the frequency limits for coherent acoustic pulse generation have been merely technological. The development of high-frequency acoustic vibrations can be traced back to the discovery of the piezoelectric effect by Pierre Curie [4]. After many years of research of acoustics in liquids, the first applications of ultrasound in condensed matter were developed by Sokolov [5]. The field of solid-state ultrasonics was greatly accelerated by the development of high-quality piezoelectric transducers [6], and was extended into the gigahertz regime by Bömmel and Dransfeld [7] using microwave cavities. Although frequency generation up to 114 GHz has been reported [8], the conventional electro-acoustic methods reach their practical limit around several tens of gigahertz. In 1975, Grill and Weis [9] reported surface generation of coherent phonons in the terahertz range using direct absorption of infrared laser radiation by a piezoelectric crystal. Although these results were not reproduced, it showed that other avenues exist to generate coherent terahertz phonons.

Among the variety of methods, one avenue of research deserves some special attention by its close connection to the experiments described later on in this thesis. This involves the interactions between high-frequency acoustic waves and the

electronic levels of impurity atoms embedded in the host lattice. The interaction between ultrasonic waves and the Zeeman-split ground-state levels of paramagnetic impurity ions was developed experimentally by Shiren [10], and described theoretically by Jacobsen and Stevens [11]. Tucker [12] showed that, after inversion of the electronic system, it may release its energy in the form of stimulated emission of phonons. An important step forward was made by replacing the paramagnetic ions with transition metal ions [13], which have excited-state levels that are connected through a single-phonon transition at terahertz frequencies. Several experiments were performed on stimulated phonon-emission in various systems [13–16], but most of them could be explained by incoherent rate-equations. The question of coherence of the emitted terahertz phonons was only addressed by Overwijk *et al.* [17], who managed to switch between incoherent and coherent phonon emission by changing the concentration of excited impurity ions.

A completely new field of ultrasonics was opened up by the introduction of picosecond pulsed lasers [18, 19], allowing for relatively direct generation of pressure pulses in an absorbing material. For application as a transducer material, metallic films are very suitable because of their short optical absorption length and the fast response of the lattice via the thermoelastic mechanism. Strain wave-packets are ultimately limited in width by this skin depth, that corresponds to an acoustic frequency spectrum up to several hundreds of gigahertz [19, 20]. However, the finite electronic transport and heat diffusion during the first moments after excitation [21–23] limit the generation of these high-frequency components to only the thinnest of metallic films.

1.2 Picosecond Ultrasonics

As an extension of conventional ultrasonics into the nanometer size-regime, the method of picosecond ultrasonics has found wide application as an imaging tool in scientific and industrial environments [20–33]. The small width of the strain pulses sets a limit to the spatial resolution that can otherwise only be achieved using x-ray radiation. Most of the early publications in this field used thin metal films for the generation and detection of picosecond strain pulses. A brief overview of the experimental work on different metallic transducers can be found in Ref. [28].

Compared to the extensive studies of metal films, the field of acoustic-pulse formation in semiconductor materials is relatively new and unexplored. Ultrafast

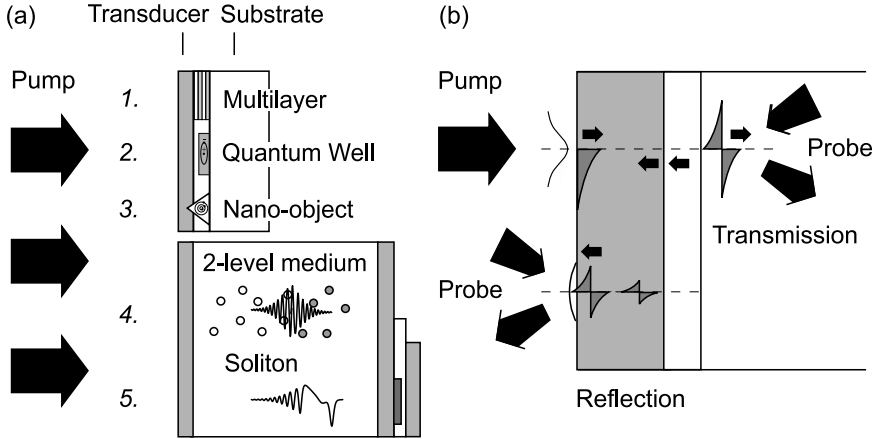


FIGURE 1.2 (a) Possible applications of picosecond strain pulses in the analysis of thin films and nanostructures. Numbers correspond to topics in text. (b) Principle of picosecond ultrasonics, using ultrafast optical excitation and detection of either the reflected echoes or the transmitted wavepacket.

excitation of quantum wells and multilayer structures has nevertheless demonstrated the formation of localized (‘Zone Folded Phonons’) and extended coherent acoustic vibrations at terahertz frequencies [34–40]. One of the main advantages of using epitaxially grown structures for terahertz-phonon experiments is the atomic-scale flatness of the interfaces inside the grown structures.

Now that picosecond ultrasonics has become an accepted and well-developed tool, some initial explorations have been made to find out whether it can be applied on a much broader scale. Figure 1.2(a) shows some perspectives for the application of ultrashort strain pulses, categorized according to the following subjects:

1. **Analysis of thin-film and nanostructured media:** Currently this is the principle research area that is actively being studied. Next to the analysis of one-dimensional multilayer structures (‘nano-seismology’), attempts have been made to characterize the acoustic behavior of composite and nanostructured media [25–27]. Additionally, the shape of the generated strain pulses is used to deduce the electron dynamics [22, 23, 28], and to study the wavelength-dependent elasto-optic coupling parameters [29] of the metal film.

2. **Embedded structures and Quantum wells:** Picosecond strain pulses allow for the characterization of buried layers inside an epitaxially grown structure [34]. Piezoelectric quantum wells hold promise as a novel source for coherent terahertz phonons [40, 41], and conversively, are likely to produce electromagnetic terahertz-radiation under ultrafast strain modulation. Magnetically doped quantum-wells form a sensitive probe for phonon dynamics and may be used to detect ultrashort strain pulses [42].
3. **Imaging of single nano-objects:** The combination of ultrafast probing and confocal or near-field microscopy [43, 44] allows for a detailed study of the dynamics of small structures and their mechanical coupling to the environment [45, 46]. The development of combined techniques for imaging on the nanometer-scale with subpicosecond time resolution is a very active area since many technologies are nowadays operating in this range, close to the fundamental limits of the material excitations.
4. **Coherent phonons in two-level media:** Coherent electron-phonon interactions and amplification of the strain field are accessible using local two-level systems embedded in a host matrix [47–50]. One of the challenging goals of this direction of research may be the construction of the acoustical analogue of the optical LASER, resulting in a high-intensity terahertz phonon source.
5. **Long-distance propagation and far-field imaging:** Propagation of strain pulses over long distances can yield invaluable information on fundamental material properties like phonon dispersion, ultrasonic attenuation and lattice anharmonicity [30, 32, 33]. Additionally, propagation of high-amplitude pulses over long distances results in pulse distortion and soliton formation [31, 51], which will be the topic of this thesis. After this special nonlinear development, the pulses may again be used to excite embedded structures or surface layers on the other side of the crystal, or excite two-level systems. Finally, special far-field techniques are being developed to map out the diffraction of a reflected pulse from a nano-object [52], allowing for the full 2-dimensional reconstruction of the image.

All the above examples rely on the concept of nanometer-sized strain wave-packets generated by ultrashort optical pulses. The principle of operation is shown in Fig. 1.2(b). The optical pulses are used to excite the electron gas via intra- or

interband absorption in the first few nanometers of the metal film. The excess energy in the promoted electrons is redistributed over the other carriers via electron-electron interactions within tens of femtoseconds, and subsequently transferred to the lattice through electron-phonon coupling within less than a picosecond. Depending on the exact mechanism involved, either thermo-elasticity for metals or nonthermal bond-switching processes for semiconductors [53], this energy is converted into a coherent compression or expansion of the lattice. In the case of a metal film, the local changes in electron density set up a coherent, longitudinal contraction in the absorption layer. When the area of excitation is much larger than the optical skin depth, a plane-wave compressional wave is launched in both directions perpendicular to the surface. The part travelling to the stress-free surface is reflected with a phase change, resulting in a release wave following the compression, which pulls the lattice back to its initial state. At an interface or embedded objects inside the material, part of the bipolar wavepacket is reflected back in the direction of the surface. These acoustic echoes can be detected at the surface using time-resolved reflectometry or interferometry and yield information on the internal structure, even if the material is optically opaque. Since the early work at Brown University [18, 19], various elegant methods have been developed to detect surface vibrations in the time domain. The most popular one is the method of transient reflectometry, where the absolute change in reflectivity of a film is detected during the passage of a strain pulse. The signal obtained in this way is usually dominated by the elasto-optic effect, and may depend on the optical probe-wavelength [26, 29]. An early approach to study the actual surface motion was made using probe-beam deflection measurements [21], where the strained region produces locally a tilting of the surface, that can be detected by measuring the angle of reflection using a quadrant photodetector. This method was soon after replaced by more advanced, interferometric techniques, that allow for the separate measurement of both phase and amplitude modulation of the reflected signal for a plane surface displacement [33, 54].

1.3 Scope and outline of this thesis

When these picosecond acoustic pulses were allowed to travel over millimeter distances at low temperatures, it was discovered that the pulses became severely distorted by the dispersion of the crystalline lattice [30, 31]. Thus, for the first time, it seems that the limit for high-frequency acoustic wavepackets is set by

fundamental physics rather than technological issues. However, there exists a regime in which even shorter coherent strain pulses are made, that can travel over long distances without distortion by the phonon dispersion. This mechanism is explained below.

In a high-amplitude, coherent strain pulse of very short duration, the deformation of the lattice will be so large that the velocity of sound starts to depend significantly on the local pressure. Most solids show an increase in sound velocity with applied pressure, resulting in a nonlinear propagation effect called *self-steepening*. Effectively, this means that the peak of the strain pulse travels faster than and eventually overtakes the leading edge of the pulse, resulting in a shock-wave. It was already predicted by Breazale and Ford [55] that, for a piezoelectrically generated ultrasonic wave in the gigahertz regime, such a discontinuity would only develop after a travelled distance of about 500 cm. However, for a picosecond strain pulse containing frequency components around 100 GHz, this condition for the critical distance drops dramatically and experiments are well within reach.

The combination of high strain values on short length scales sets the stage for a range of striking nonlinear acoustic phenomena. When the picosecond strain pulse steepens and eventually forms a shock wave by the nonlinearity, high-frequency strain components are generated at the shock front. At this point, the phonon dispersion takes over and delays these new, high-frequency components with respect to the lower frequencies in the wavepacket, causing a strong disruption of the shock wavefront. The combined action of dispersion and nonlinearity in the wavepacket development now sets up a system in which stable, *solitary waves* are formed [56]. These soliton wavepackets are intrinsically stabilized by the balance between nonlinearity and dispersion and thus are extraordinary robust to weak external disturbances.

In a conventional picosecond ultrasonics setup, only a minute fraction of the intensity of an optical laser pulse (typically 0.1 mJ/cm^2) is converted to a coherent acoustic strain of the order of 10^{-5} , depending on the transducer used. At these low strains nonlinear effects are of no importance unless the strain pulse is allowed to propagate over long distances. In a pioneering series of experiments in large crystals at low temperatures, Hao *et al.* [32] demonstrated that indeed a propagation distance of millimeters is sufficient to convert a relatively low-strain wave packet into a soliton and an oscillating tail. These results were shown to be consistent with simulations based on the Korteweg-de Vries (KdV) equation in one dimension, signifying that the lattice itself provides sufficient dispersion for

soliton development.

As we will show, extension to higher strains leads to the development of solitons after propagation over much shorter distances, as well as the generation of extremely fast solitons and soliton trains [51]. In water basins and liquid-gas mixtures, breakup of long-wavelength disturbances has been demonstrated experimentally into soliton trains of considerably higher frequencies [57, 58]. Until now, no attempts have been made to explore similar phenomena in the field of ultrashort acoustic pulses in solids. Recent experiments have shown atomic motion under high impulsive strain [59–61] and the development of shock waves in metal films [62, 63]. However, those experiments only focused on the propagation over micrometer distances, much too short to obtain ultrafast soliton trains.

In this thesis, we present experiments that are aimed at understanding the development of ultrashort strain solitons over a long propagation distance. We increase the amplitude of the strain pulses relative to those in picosecond ultrasonics by almost two orders of magnitude using optical excitation by mJ optical pulses from an amplified Ti:sapphire laser. Further, new and unconventional techniques, at least for the field of picosecond ultrasonics, are introduced to monitor the wavepacket development in the *bulk* of a transparent crystal. After the introduction of the theory behind ultrashort strain solitons in Chapter 2, we use for the first time a Brillouin scattering setup to detect modelocked strain wavepackets in lead molybdate in Chapter 3. Subsequently, the same method of Brillouin scattering is applied in Chapters 4 and 5 to monitor the development of gigahertz strain components of a high-amplitude, picosecond acoustic wavepacket as it evolves into a train of ultrashort strain solitons in sapphire. In another series of experiments, presented in Chapters 6 and 7, the coherent interactions between ultrashort strain solitons and terahertz electronic two-level systems is investigated in optically excited ruby. Finally, in Chapter 8, we present the details of our developed low repetition-rate pump-probe setup for ultrafast reflectometry and transmission experiments.

Next to the main line presented in the chapters, we have chosen to separate some specialized themes in the form of three appendices. Appendix A is dedicated to the numerical simulations that were performed to explain our results on Brillouin scattering in sapphire in Chapter 4. Appendix B is used to introduce some of the physics of the phonon-induced electronic transition of the ruby phonon spectrometer and to obtain an estimate for the transition matrix element. Finally, in Appendix C we estimate the role of the rarefaction part, that does not produce

solitons but does contain terahertz frequency components, on the experiments in this thesis.

References

- [1] W. J. Andrefsky, *Lithics* (Cambridge University Press, 1998).
- [2] P. Fish, *Physics and Instrumentation of Diagnostic Medical Ultrasound* (Wiley, 1990), 1st ed.
- [3] J. Krautkramer and H. Krautkramer, *Ultrasonic Testing of Materials* (Springer Verlag, 1990), 4th ed.
- [4] J. Curie and P. Curie, C. R. Acad. Sci. **91**, 294 (1880).
- [5] S. Y. Sokolov, Tech. Phys. **2**, 1 (1935).
- [6] G. R. Ringo, J. W. Fitzgerald, and B. G. Hurdle, Phys. Rev. **72**, 87 (1947).
- [7] H. E. Bömmel and K. Dransfeld, Phys. Rev. Lett. **1**, 234 (1958).
- [8] J. Ilukor and E. H. Jacobsen, Science **153**, 1113 (1966).
- [9] W. Grill and O. Weis, Phys. Rev. Lett. **35**, 588 (1975).
- [10] N. S. Shiren, Phys. Rev. **128**, 2103 (1962).
- [11] E. H. Jacobsen and K. W. H. Stevens, Phys. Rev. **129**, 2036 (1963).
- [12] E. B. Tucker, Phys. Rev. Lett. **6**, 547 (1961).
- [13] W. E. Bron and W. Grill, Phys. Rev. Lett. **40**, 1459 (1978).
- [14] P. Hu, Phys. Rev. Lett. **44**, 417 (1980).
- [15] D. J. Sox, J. E. Rives, and R. S. Meltzer, Phys. Rev. B **25**, 5064 (1982).
- [16] J. G. M. van Miltenburg, G. J. Jongerden, J. I. Dijkhuis and H. W. de Wijn, in *Phonon Scattering in Condensed Matter*, ed. W. Eisenmenger, K. Laßman and S. Döttinger (Springer-Verlag, 1984), p. 130.
- [17] M. H. F. Overwijk, J. I. Dijkhuis, and H. W. de Wijn, Phys. Rev. Lett. **65**, 2015 (1990).
- [18] C. Thomsen et al., Phys. Rev. Lett. **53**, 989 (1984).
- [19] C. Thomsen, H. T. Grahn, H. J. Maris, and J. Tauc, Phys. Rev. B **34**, 4129 (1986).
- [20] C. Zhu, J. Tauc, and H. Maris, Phys. Rev. B **44**, 4281 (1991).
- [21] O. B. Wright and K. Kawashima, Phys. Rev. Lett. **69**, 1668 (1992).
- [22] G. Tas and H. J. Maris, Phys. Rev. B **49**, 15046 (1994).
- [23] O. B. Wright, Phys. Rev. B **49**, 9985 (1994).
- [24] See for example <http://www.rudolphtech.com/>.
- [25] K. E. O'Hara, X. Hu, and D. Cahill, J. App. Phys. **90**, 4852 (2001).
- [26] C. A. C. Bosco, A. Azevedo, and L. H. Acioli, Phys. Rev. B **66**, 125406 (2002).
- [27] G. A. Antonelli, H. J. Maris, S. G. Malhotra, and J. M. E. Harper, J. of Appl. Phys **91**, 3261 (2002).
- [28] T. Saito, O. Matsuda, and O. B. Wright, Phys. Rev. B **67**, 205421 (2003).
- [29] A. Devos and C. Lerouge, Phys. Rev. Lett. **86** (2001).

- [30] H.-Y. Hao and H. J. Maris, Phys. Rev. Lett. **84**, 5556 (2000).
- [31] H.-Y. Hao and H. J. Maris, Phys. Rev. B **64**, 064302 (2001).
- [32] H.-Y. Hao and H. J. Maris, Phys. Rev. B **63**, 224301 (2001).
- [33] J.-Y. Duquesne and B. Perrin, Phys. Rev. B **68**, 134205 (2003).
- [34] J. J. Baumberg, D. A. Williams, and K. Köhler, Phys. Rev. Lett. **78**, 3358 (1997).
- [35] A. Bartels, T. Dekorsy, H. Kurz, and K. Köhler, Phys. Rev. Lett. **82**, 1044 (1999).
- [36] O. B. Wright, B. Perrin, O. Matsuda, and V. E. Gusev, Phys. Rev. B **64**, 081202 (2001).
- [37] Ü. Özgür, C.-W. Lee, and H. O. Everitt, Phys. Rev. Lett. **86**, 5604 (2001).
- [38] A. Kent, N. M. Stanton, L. Challis, and M. Henini, Appl. Phys. Lett. **81**, 3497 (2002).
- [39] N.-W. Pu and J. Bokor, Phys. Rev. Lett. **91**, 076101 (2003).
- [40] J. S. Yahng et al., Appl. Phys. Lett. **80**, 4723 (2002).
- [41] C.-K. Sun, J.-C. Liang, and X.-Y. Yu, Phys. Rev. Lett. **84**, 179182 (2000) **84**, 179 (2000).
- [42] A. V. Scherbakov et al., Phys. Rev. B **60**, 5609 (1999).
- [43] T. Guenter et al., Phys. Rev. Lett. **89**, 057401 (2002).
- [44] M. Achermann, U. Siegner, L.-E. Wernersson, and U. Keller, Appl. Phys. Lett. **77**, 3370 (2000).
- [45] A. Vertikov, M. Kuball, A. Nurmikko, and H. Maris, Appl. Phys. Lett. **69**, 2465 (1996).
- [46] Y. Sugawara et al., Phys. Rev. Lett. **88**, 185504 (2002).
- [47] N. S. Shiren, Phys. Rev. B **2**, 2471 (1970).
- [48] J.-Y. Prieur, J. Joffrin, and K. Lassman, Physica **B316-317**, 125 (2002).
- [49] L. G. Tilstra, A. F. M. Arts, and H. W. de Wijn, Phys. Rev. B **68**, 144302 (2003).
- [50] O. L. Muskens, A. V. Akimov, and J. I. Dijkhuis, Phys. Rev. Lett. **92**, 335503 (2004).
- [51] O. L. Muskens and J. I. Dijkhuis, Phys. Rev. Lett. **89**, 285504 (2002).
- [52] N. C. R. Holme, M. T. Myaing, and T. B. Norris, Appl. Phys. Lett. **83**, 392 (2003).
- [53] V. E. Gusev and A. A. Karabutov, *Laser optoacoustics* (AIP Press, 1993), 1st ed.
- [54] D. H. Hurley and O. B. Wright, Opt. Lett. **24**, 1305 (1999).
- [55] M. A. Breazale and J. Ford, J. Appl. Phys. **36**, 3486 (1965).
- [56] G. B. Whitham, *Linear and Nonlinear Waves* (Wiley, 1974), 1st ed.
- [57] D. A. Horn, J. Imberger, and G. N. Ivey, J. Fluid Mech. **434**, 181 (2001).
- [58] V. V. Kuznetsov, V. E. Nakoryakov, B. G. Pokusaev, and I. R. Schreiber, J. Fluid Mech. **85**, 85 (1978).
- [59] D. A. Reis et al., Phys. Rev. Lett. **86**, 3072 (2001).
- [60] A. Cavalleri et al., Phys. Rev. Lett. **85**, 586 (2000).
- [61] C. Rose-Petruck et al., Nature **398**, 310 (1999).
- [62] K. T. Gahagan et al., Phys. Rev. Lett. **85**, 3205 (2000).
- [63] R. Evans et al., Phys. Rev. Lett. **77**, 3359 (1996).

CHAPTER 2

THEORY OF STRAIN SOLITONS

Abstract

We review some of the concepts of nonlinear elasticity that are the basis of the theory of strain solitons. The governing equations are derived from the starting point of continuum elasticity. It is shown for one dimension and for moderate strains that the multidimensional formulation of finite strain lattice dynamics reduces to the well-known Korteweg-de Vries equation. The soliton solutions for this equation, as well as the formation of soliton trains from an initial disturbance, are examined in the context of the experiments in this thesis.

2.1 Introduction

In this chapter we present a short overview over the classical theory of nonlinear elasticity for finite deformations. In contrast to the theory of infinitesimal elasticity, that was already well-developed in the beginning of the twentieth century [1], extension to intermediate strains was taken up seriously in the early fifties [2]. Closely related to the theory of fluid mechanics, solid-state models have been developed in the continuum limit and in the language of the bulk elasticity parameters. This results in a dispersionless theory, and lattice dispersion can only be included a posteriori, in an artificial way. Therefore we also present as an *intermezzo* a path to the nonlinear dispersive wave equation starting from a microscopic picture. Then, after transformation to travelling coordinates, we readily arrive at the well-known Korteweg-de Vries (KdV) equation, that has stable solutions in the form of *solitary waves* [3, 4]. It is shown that an initial compressional strain pulse breaks up into a train of such solitons. For this purpose, we briefly introduce the idea behind the inverse scattering theory, without going deeply into

the mathematical details. Rather, some expressions are presented that are directly applicable to our experiments on picosecond strain pulses in sapphire. Finally, we consider the effect of temperature on the wavepacket development and briefly present the theory for shock waves using the Burgers equation.

2.2 Nonlinear elasticity theory

2.2.1 General formulation

In this overview of nonlinear elasticity theory we follow the derivation and nomenclature as presented in the review of Wallace [5]. First, a set of curvilinear coordinates is introduced and the local deformation and strain variables are derived in this basis. Throughout the text we will be using the Einstein summation convention.

Let us consider an undeformed solid in which a point is denoted by the vector $\vec{r} = r_j \vec{a}_j$ with respect to the basis $\{\vec{a}_j\}$ of the crystal. In an arbitrary deformed state, the position of the vector changes to $\vec{r}' = \vec{r} + \vec{u}(\vec{r}, t)$, with $\vec{u}(\vec{r}, t)$ the local displacement vector corresponding to the deformation [see Fig. 2.1]. The above definitions also allow for transformations that do not distort the internal material structure, like uniform translation and rotation. A good definition of local deformation that filters out these simple transformations is the length change, or deformation Δ , of a local vector $\Delta\vec{r} = \vec{r}_2 - \vec{r}_1$ [c.f. Fig. 2.1]:

$$\begin{aligned} \Delta &= |\Delta\vec{r}'|^2 - |\Delta\vec{r}|^2 \\ &= 2\eta_{ij} \Delta r_i \Delta r_j . \end{aligned} \quad (2.1)$$

The right hand side of Eq. (2.1) has been obtained by expanding the squared terms using $\vec{u}(\vec{r}_2, t) - \vec{u}(\vec{r}_1, t) = \nabla\vec{u}(\vec{r}, t) \Delta\vec{r}$. The matrix connecting the initial configuration \vec{r} to the deformation Δ is called the strain matrix η , and follows from Eq. (2.1) as

$$\eta_{ij} = \frac{1}{2}(u_{ij} + u_{ji} + u_{ik}u_{kj}) , \quad (2.2)$$

where

$$u_{ij} = \frac{\partial u_i}{\partial r_j} \quad (2.3)$$

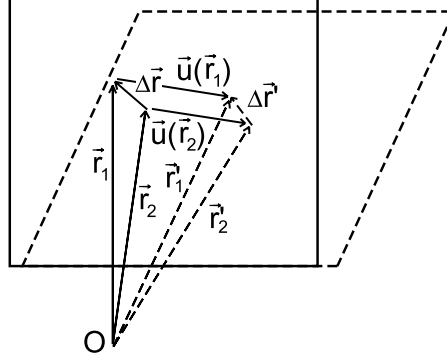


FIGURE 2.1 Representation of arbitrary deformation of an elastic solid. Definition are shown of vectors $\{\vec{r}, \Delta\vec{r}\}$ and $\{\vec{r}', \Delta\vec{r}'\}$ in undeformed and deformed state, respectively, and local transformation vector \vec{u} .

describes the displacement gradient matrix elements. The above description holds as long as variations in the displacement gradients take place on a length scale much larger than the differential elements $\Delta\vec{r}$. In practice this means that the strain must be smooth on the scale of the interatomic distances in the solid.

The important consequence of Eq. (2.1) is that related quantities like the free energy at finite strain can be expressed in terms of the undeformed coordinates \vec{r} and the strain matrix η . For example, one can expand the internal energy Φ per unit of mass in terms of strain according to

$$\rho\Phi_S(\vec{r}, \eta) = \rho\Phi_0 + C_{ij}\eta_{ij} + \frac{1}{2}C_{ijkl}\eta_{ij}\eta_{kl} + \frac{1}{6}C_{ijklmn}\eta_{ij}\eta_{kl}\eta_{mn} + \dots \quad (2.4)$$

Here ρ is the mass density and the subscript S denotes that the deformation takes place at constant entropy, i.e. under adiabatic conditions. The constants C are the elasticity constants of first, second and third order, respectively, defined by the first- and higher-order partial derivatives of the internal energy to the strain elements, $C_{ij} = \partial\Phi_S / \partial\eta_{ij}$, $C_{ijkl} = \partial^2\Phi_S / \partial\eta_{ij}\partial\eta_{kl}$, etc.

For a simple, one dimensional spring, one can calculate the force resulting from a compression by taking the derivative of the internal energy to the displacement (Hooke's law). On a similar vein, one can calculate the induced stresses from the strain in the material using simple thermodynamic considerations. According to the second law of thermodynamics, for a process at constant entropy

$\rho d\Phi_S = dW$. The work dW in a deformed state can be derived by applying an additional infinitesimal, homogeneous change in strain $\Delta\eta_{ij}$. Thus, in simple terms the stresses can be obtained by calculating the derivative of the work to the strain in the deformed coordinates. For the general formalism we refer again to Wallace [5], and give the resulting stress-strain relation for a stress-free initial state:

$$T_{ij} = \rho \frac{\partial \Phi_S(\vec{r}, \eta)}{\partial \eta_{ij}} . \quad (2.5)$$

The equation of motion for finite strains can now be formulated in terms of this stress tensor and the mass density ρ . The Euler-Lagrange equations of motion for the generalized coordinates $\vec{r}'(\vec{r}, t)$ in the independent variables \vec{r} and t read

$$\frac{\partial}{\partial t} \frac{\partial L}{\partial \dot{r}'_i} + \frac{\partial}{\partial r_k} \frac{\partial L}{\partial \alpha_{ik}} = 0 , \quad (2.6)$$

with the abbreviation $\alpha_{ik} = \partial r'_i / \partial r_k$. The Lagrangian density can be written as the difference of kinetic and potential energy, which for adiabatic deformation gives

$$L = \frac{1}{2} \rho \dot{r}'_i \dot{r}'_i - \rho \Phi_S(\vec{r}, t) . \quad (2.7)$$

Combining Eqs. (2.6) and (2.7), one arrives at the equation of motion

$$\rho \dot{r}'_i = \rho \frac{\partial}{\partial r_k} \left(\frac{\partial \Phi_S}{\partial \eta_{lm}} \right) \frac{\partial \eta_{lm}}{\partial \alpha_{ik}} . \quad (2.8)$$

Using the relation $\partial \eta_{lm} / \partial \alpha_{ik} = \delta_{il} \delta_{km}$ for a stress-free initial state [5], one can simplify the equation of motion, Eq. (2.8), to a generalized form of Newton's law

$$\rho \ddot{u}_i = \frac{\partial}{\partial r_k} T_{ik} . \quad (2.9)$$

Here we have replaced the higher order derivative of \vec{r}' by that of the displacement vector \vec{u} , which is allowed by its definition in Eq. (2.1). With the combination of Eq. (2.9), the stress-strain relation Eq. (2.5), and the free energy expansion Eq. (2.4), we now have all the ingredients to compose a nonlinear acoustic wave equation. Keeping only terms up to second order in derivatives of u , this equation of motion can be rearranged into the form

$$\rho \ddot{u}_i = \frac{\partial u_{jk}}{\partial r_l} (C_{ijkl} + u_{pq} A_{ijklpq}) . \quad (2.10)$$

It should be noted that the term A_{ijklmn} contains a combination of third-order *and* second order elastic constants:

$$A_{ijklpq} = C_{jlpq} \delta_{ik} + C_{ijql} \delta_{kp} + C_{jkql} \delta_{ip} + C_{ijklpq} . \quad (2.11)$$

The second-order coefficients in this expression are a consequence of the presence of the quadratic term in the definition of strain, Eq. (2.2). Therefore, these contributions to the nonlinear term in the propagation equation, Eq. (2.10), are sometimes referred to as the *geometrical* nonlinearity, whereas the third order constants are called the *physical* nonlinearity. One may convert the elastic constants in Eq. (2.10) to tabulated values in Voigt notation [6] by the reduction of pairs of indices according to $11 \rightarrow 1, 22 \rightarrow 2$, and so on.

2.2.2 Reduction to single dimension

In the case of one-dimensional propagation along an axis of high symmetry z , the equation of motion, Eq. (2.10), reduces to the simple form

$$\rho u_{tt} = \gamma u_{zz} + \alpha u_z u_{zz} , \quad (2.12)$$

where the subscripts denote differentiation. The last term on the right side is the quadratic nonlinearity, owing to the geometric nonlinearity and the cubic terms in the inter-atomic potential. The nonlinearity coefficient α depends only on the propagation direction in the crystal. For the [0001]-direction in a trigonal crystal like sapphire, the two constants of Eq. (2.12) take on the form

$$\gamma = C_{33}, \quad \alpha = (3C_{33} + C_{333}) , \quad (2.13)$$

where the coefficients C_{33} and C_{333} are the second- and third-order elastic moduli in the [0001]-direction. For most solids, the contribution of the third order modulus is larger than the geometric term and has a negative sign, yielding an $\alpha < 0$.

Up to this point we have not taken into account any dispersion in the equation of motion. In the case of longitudinal acoustic lattice vibrations (LA phonons) in a trigonal crystalline solid in the direction of the c axis ([0001]), the dispersion due to discreteness of the lattice can be written as [7]

$$\omega = \sqrt{\frac{4C_{33}}{M}} \sin |ka/2|. \quad (2.14)$$

As we will be dealing with vibrations of small wavevector, i.e. in the center of the Brillouin zone, it is sufficient to approximate this dispersion relation by its first two nonzero expansion terms

$$\begin{aligned} \omega &= c_0 k - \beta k^3 \\ \beta &= \frac{c_0 a^2}{24} = \frac{c_0^3}{6\omega_{max}^2}, \end{aligned} \quad (2.15)$$

where $\omega_{max} = (4C_{33}/M)^{1/2}$ is the LA angular frequency at the edge of the Brillouin zone, and $c_0 = (C_{33}a^2/M)^{1/2}$ denotes the sound velocity. This dispersive correction can be put into Eq. (2.12), leading to a fourth order spatial derivative (see e.g. Ref [8]). At this point it is convenient to switch from the displacement coordinate u to a uniaxial component of the acoustic strain, further denoted as s . This is done by differentiation of Eq. (2.12) with respect to the z -coordinate. Given the initial wave packet at $t = 0$ of amplitude s_0 and shape $\phi(z)$, the resulting boundary value problem including dispersion, reads

$$\begin{aligned} s_{tt} - c_0^2 s_{zz} - \frac{\alpha}{\rho} \frac{\partial}{\partial z} (s s_z) + 2c_0 \beta s_{zzzz} &= 0 \\ s(z, t = 0) &= s_0 \phi(z). \end{aligned} \quad (2.16)$$

Finally it is convenient to transform to a moving frame coordinate system, defined by the parameters $t' = t$, $y = z - c_0 t$. After substitution of these variables we arrive at terms consisting of only one derivative with respect to the travelling coordinate y , except for one term having a double time derivative $s_{t't'}$. Neglecting this term will not change the behavior up to first order, as this is a 'slow' coordinate with respect to the evolution of the wave packet. Integrating the resulting expression once, we finally obtain the equation

$$\begin{aligned} s_{t'} + \frac{\alpha}{2\rho c_0} s s_y - \beta s_{yyy} &= 0 \\ s(y, t' = 0) &= s_0 \phi(y). \end{aligned} \quad (2.17)$$

This is the well-known Korteweg-de Vries (KdV) equation, describing for example the formation of stable wave packets (solitons) in a narrow water channel

[3]. In the experimental configuration in the sapphire crystal, $\alpha < 0$ and $\beta > 0$, resulting in soliton development for $s < 0$, i.e. for compressional strain pulses.

2.3 Microscopic model

Before continuing with the solutions of the problem of nonlinear wavepacket development, we wish to spend some words to an alternative approach to derive the nonlinear dispersive wave equation. In the previous section, we have reviewed the classical theory of finite elasticity, leading to a fully three-dimensional, nonlinear wave equation for arbitrary crystallographic symmetry. After reduction to one dimension, phonon dispersion was added by means of a correction *a-posteriori*. For the problem of ultrashort strain packets in a crystalline lattice, it may well be worth the effort to consider a derivation that maintains the discrete character of the atomic lattice. The theory of nonlinear lattices has been developed since the early work of Fermi, Pasta and Ulam [9], but has soon focused on analytical model systems in one dimension (see e.g. [10]). In these models, dispersion is an inherent feature of the discrete system, and solitary waves have been identified as the normal modes of the nonlinear lattice. It has been demonstrated that the one-dimensional integrable lattice with exponential interactions, known as the Toda chain [10], reduces to the KdV equation in the long-wavelength limit.

Potapov *et al.* [11] showed that a microscopic lattice model can be used to derive the nonlinear dispersive wave equation for the atomic displacements. They started from a two-dimensional construction of point masses and considered only nearest-neighbor interactions in the first two configurational shells. Meijer [12] extended this approach to a cubic lattice in three dimensions. In these calculations, the local deformations are again defined by the square of the interatomic distances, similar to Eq. (2.1), but now on a discrete lattice. Subsequently, the transition from a discrete to a continuous description is made by maintaining an additional term in the expansion for the local displacements $u_{i,j,k}$

$$\begin{aligned} u_{i\pm 1,j\pm 1,k} &= u(x \pm a, y \pm a, z) \\ &\approx u(x, y, z) \pm a(u_x + u_y) + \frac{1}{2}a^2(u_{xx} + 2u_{xy} + u_{yy}) + \dots, \end{aligned} \quad (2.18)$$

where a denotes the interatomic distance of the cubic lattice. Note that we would have obtained similar results in the previous section if in the derivation of Eq. (2.1) the expansion would have been $\vec{u}(\vec{r}_2, t) - \vec{u}(\vec{r}_1, t) = \nabla \vec{u}(\vec{r}, t) + \frac{1}{2} \nabla \cdot (\nabla \vec{u}(\vec{r}, t))$. How-

ever, a redefinition of the concept of strain would have been necessary in this case, which is a complication we do not wish to stir up at this point. Meijer avoids this complication by maintaining the displacement coordinates as the working variables and expanding the lattice free energy in these coordinates rather than in the strain.

After rewriting the Euler-Lagrange equations of motion analogue to Eq. (2.6), the inclusion of the additional term in the displacement derivatives results in dispersive terms in the final wave equation [11, 12]. After reduction to one dimension, the Boussinesq equation [c.f. Eq. (2.16)] is once more obtained, only this time with constants depending on the microscopic interaction potentials. Not surprisingly, the dispersive factor is found to be equal to the expansion term in Eq. (2.15), justifying the artificial approach of Sec. 2.2.2.

2.4 The KdV initial-value problem

We now continue with the main topic of this chapter, namely the solution of the nonlinear dispersive wave equation. We are interested in the development of an arbitrary initial waveform $s(z, t) = s_0\phi(z/l_0)$, where $s_0 < 0$ and l_0 are the typical amplitude and width of the compressional part of the initial strain packet. After transformation to the coordinates $\eta = s/s_0$, $\xi = z/l_0$, and $\tau = t\alpha s_0/2\rho c_0 l_0$, the initial value problem of Eq. (2.17) takes on the form [13]

$$\begin{aligned} \eta_\tau + \eta\eta_\xi + \frac{1}{\sigma^2}\eta_{\xi\xi\xi} &= 0 \\ \eta(\xi, 0) &= \phi(\xi), \end{aligned} \tag{2.19}$$

where σ is a dimensionless parameter defined by

$$\sigma = l_0 \left(\frac{\alpha s_0}{2\rho c_0 \beta} \right)^{1/2}. \tag{2.20}$$

Equation (2.19) yields identical solutions for initial wavepackets with the same value of σ and $\phi(\xi)$, and therefore σ is called the similarity parameter. The magnitude of σ determines the relation between nonlinearity and dispersion in the wavepacket development. Note that according to Eq. (2.20), σ is proportional to the area under the square root of the compressional strain waveform. In order to compare the similarity parameters for different initial value conditions, it is thus

important to choose l_0 and s_0 so that the residual area of $[\phi(\xi)]^{1/2}$ is normalized to some predefined value, which in Ref. [13] equals π , the area under the square root of the sech^2 -waveform.

2.4.1 Single-soliton solution

One can show that there exists a class of exact soliton solutions of the KdV equation [4, 14, 15], for which $\sigma_s = \sqrt{12}$ [13]. For this purpose we consider solutions to the KdV-equation of the form $\eta(\xi, \tau) = f(\xi - W\tau) = f(\zeta)$, where W denotes the velocity in the moving frame system. For these modes, the KdV-equation Eq. (2.19) reduces to a single parameter equation, that after one integration over ζ reads

$$-Wf + \frac{1}{2}f^2 + \sigma^{-2}f_{\zeta\zeta} = c_1, \quad (2.21)$$

Multiplication of all terms with $\partial f / \partial \zeta$ yields a variational equation for f , that can be integrated to

$$-\frac{1}{2}Wf^2 + \frac{1}{6}f^3 + \frac{1}{2}\sigma^{-2}(f_{\zeta})^2 = c_1f + c_2. \quad (2.22)$$

From the requirement that in case $x \rightarrow \pm\infty$, $f, f_{\zeta}, f_{\zeta\zeta} \rightarrow 0$ it follows that $c_1 = c_2 = 0$. Equation (2.22) can now be put in the simple form $f_{\zeta} = \sigma f \sqrt{W - f/3}$, that may be integrated by separation of variables, giving

$$\int_0^f \frac{df'}{\sigma f' \sqrt{W - f'/3}} = \int_0^{\zeta} d\zeta'. \quad (2.23)$$

The left-hand side can be solved by the substitution $f' = 3W \text{sech}^2 q$, which results in $\sqrt{W - f'/3} = \sqrt{W} \tanh q$ and $\partial f' / \partial q = -6W \text{sech}^2 q \tanh q$. Further, the upper integration limit changes to $q_0 = \text{sech}^{-1}(f/3W)^{1/2}$. In this manner, Eq. (2.23) is rewritten as

$$-\frac{2}{\sigma \sqrt{W}} \int_0^{q_0} dq = -\frac{2}{\sigma \sqrt{W}} q_0 = \zeta. \quad (2.24)$$

Transforming back from q_0 to f now yields the single-soliton solution of the KdV equation

$$f(\xi) = f(z - Wt) = 3W \operatorname{sech}^2 \left(\frac{\sigma \sqrt{W}}{2} (z - Wt) \right). \quad (2.25)$$

This expression contains several characteristic properties of the KdV solitons. First, for given σ , there is only one free parameter, W , that determines the velocity, width and amplitude of the soliton. Secondly, it is observed that for given W , σ only modifies the width of the soliton, and not its velocity or amplitude.

In the initial-value problem of Eq. (2.19), the value of σ follows from the normalization used for the function $[\phi(\xi)]^{1/2}$. The soliton solution, Eq. (2.25), was derived without taking into account the initial-value condition. To turn it into a self-consistent solution of Eq. (2.19), we should normalize its amplitude $s_0 = -3W$ and width $l_0 = 2/\sigma \sqrt{W}$, resulting in a universal value of $\sigma_s = \sqrt{12}$ for any soliton scaled to normalized units. The capacity of an arbitrary initial wavepacket to develop one or more solitons now depends on the magnitude of its parameter σ with respect to σ_s . Any perturbation with $\sigma < \sigma_s$ may be called weakly nonlinear and with $\sigma \gg \sigma_s$ strongly nonlinear. Note that this does not say anything about the energy required for multi-soliton solutions. A short, intense waveform may produce less solitons than a longer, low-amplitude one that contains the same amount of energy. However, the solitons generated by the intense pulse have higher amplitudes (c.f. Sec 2.4.2), and consequently are shorter and move with higher velocity. As a rule of thumb, Eq. (2.20) predicts that the number of solitons increases linearly with the initial pulse width l_0 , but only proportional to the square root of the maximum pulse amplitude $|s_0|$.

2.4.2 Multi-soliton solutions

For the KdV-initial value problem Eq. (2.19) there exists an associated eigenvalue problem for the Schrödinger equation [14]

$$\Psi_{\xi\xi} + \left(\lambda + \frac{\sigma^2}{6} \eta(\xi, \tau) \right) \Psi = 0. \quad (2.26)$$

In a normal scattering problem, one is interested in the eigenvalues and reflection and transmission functions for a given potential $\eta(\xi, \tau)$. The inverse scattering problem amounts to the reconstruction of the potential *at each time* for a set of known scattering quantities, consisting of the energy levels λ_n , and the reflection and transmission functions (Ψ_R/Ψ_{in}) , (Ψ_T/Ψ_{in}) [see Fig. 2.2]. The solutions of this eigenvalue equation can consist of free or bound states, depending on the

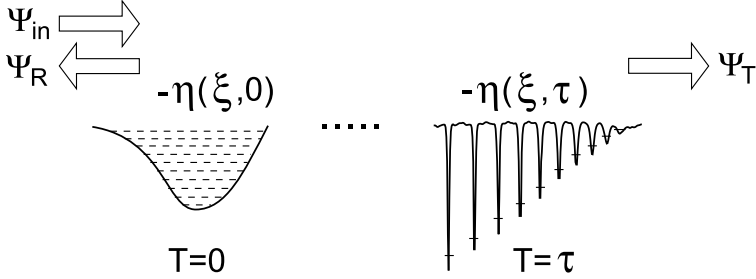


FIGURE 2.2 Visualization of inverse scattering method, where the time development of the wavepacket is mapped onto an eigenvalue problem for a time varying potential $-\eta(\xi, \tau)$. The evolution at large times can be recovered from the reflected and transmitted wavefunctions Ψ_R, Ψ_T . Horizontal lines (dash) denote eigenvalues λ_n .

sign of the initial potential $\phi(\xi)$. The reflection and transmission coefficients can be derived using the time dependence of the eigenfunctions Ψ , as dictated by the KdV equation for the potential $\eta(\xi, \tau)$. This evolution can be determined by writing $\eta(\xi, \tau)$ in terms of Ψ using Eq. (2.26) and filling it into the KdV equation, Eq. (2.19). A concise overview of the inverse scattering method for the KdV-initial value problem can be found in Refs. [13, 16].

We limit our discussion here to the most relevant result for this thesis, namely the stationary states after $t \rightarrow \infty$ for the potential $\eta(\xi, \tau)$, for a discrete spectrum of eigenmodes $\lambda_n < 0$. It turns out that all bound states of the initial potential $\phi(\xi)$ correspond to soliton-pulses of the form [13, 16]

$$\eta(\xi, \tau) = \frac{12k_n^2}{\sigma^2} \operatorname{sech}^2 \left(k_n [(\xi - \xi_0) - 4k_n^2 \tau] \right), \quad (2.27)$$

where $k_n = \sqrt{-\lambda_n} > 0$. Thus all the stationary states developing from an initial compressional wavepacket are solitons, completely defined by a single parameter, the eigenvalue λ_n . It can be observed from Eq. (2.27) that the amplitude of the n -th soliton is $\eta_n = 12\lambda_n/\sigma^2$, or $a_n = 2\lambda_n s_0$ in normal strain units. The velocity of these solitons is $\eta_n/3$ in normalized coordinates [as in Eq. (2.25)], or $c_n = \alpha a_n / 6\rho c_0$ in real coordinates [c.f. Eq. (2.19)]. Finally, the width is given by $[12/\eta_n \sigma^2]^{1/2}$, or $l_n = l_0 [12s_0/\eta_n \sigma^2]^{1/2}$ in real coordinates.

The exact number of solitons developing from an initial perturbation may be found from the depth of the potential well $\phi(\xi)$ and the spacing of the eigenvalues

of the energy. For large σ , it is possible to estimate the number of solitons using a quasi-classical approximation for the distribution of energy levels [13]. For large quantum numbers n , one may consider the distribution of energy levels to be continuous, and the wavefunctions to correspond to the classical paths in the potential. In this situation, one can apply the Bohr-Sommerfeld quantization rule [17], that connects the classical momentum to the number of energy levels of the potential

$$\frac{1}{2\pi} \oint p dx = N + \frac{1}{2}, \quad (2.28)$$

where $\oint p dx$ is taken around a closed orbit of the particle, which in the one-dimensional case amounts to $2 \int_a^b p dx$, with a, b the classical turning points. This rule can be appreciated by considering the phase space to be subdivided in modes with a volume $\Delta k \Delta x / 2\pi$. Equation (2.28) then divides the classical path in phase space into N of these unit cells. By considering the momentum to be given by $k(E) = (\frac{\sigma^2}{6} [\phi(\xi) - E])^{1/2}$ [c.f. Eq. (2.26)], one may obtain an expression for the number density by differentiating Eq. (2.28) to E , resulting in

$$\frac{\partial N}{\partial E} = (2\pi)^{-1} \left(\frac{\sigma}{\sqrt{6}} \right) \int_{\phi > E} \frac{d\xi}{\sqrt{\phi(\xi) - E}}, \quad (2.29)$$

which leads to the asymptotic expression for the total number of solitons

$$N = \left(\frac{\sigma}{\pi \sqrt{6}} \right) \int_{\phi > 0} \sqrt{|\phi(\xi)|} d\xi. \quad (2.30)$$

Note that in this limiting case, the number of solitons only depends on the positive part of the initial perturbation $\phi(\xi)$.

An analytical solution of the eigenvalue equation, Eq. (2.26) may be obtained in several special cases of the initial waveform $\phi(\xi)$. In particular, the spectrum of eigenvalues for a potential of the form $\phi(\xi) = \text{sech}^2 \xi$ has been obtained in Ref. [17]. By rewriting the Schrödinger equation in the variables $\epsilon = -\sigma \sqrt{E/6}$, $\sigma^2/6 = s(s+1)$, $\zeta = \tanh \xi$ and $u = \frac{1}{2}(1 - \zeta)$, one obtains an equation for $w(\xi) = (1 - \xi)^{-\epsilon/2} \Psi$

$$u(1-u)w'' + (\epsilon+1)(1-2u)w' - (\epsilon-s)(\epsilon+s+1)w = 0, \quad (2.31)$$

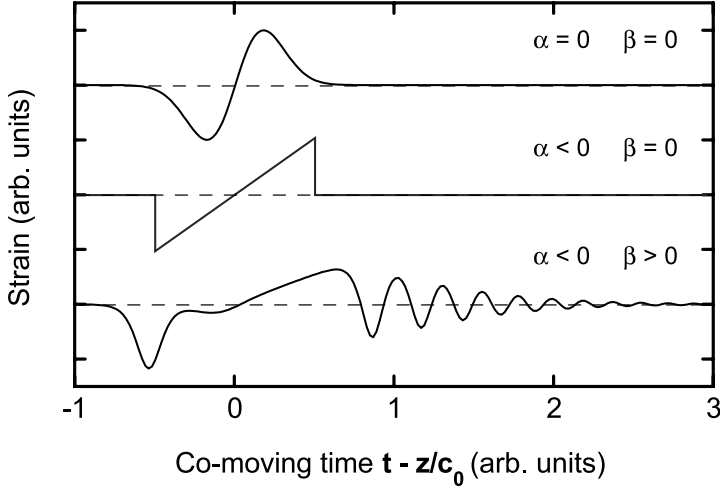


FIGURE 2.3 Development of initial wavepacket for different combinations of nonlinearity α and dispersion β , for zero damping, showing typical shock formation ($\alpha < 0, \beta = 0$) and soliton development ($\alpha < 0, \beta > 0, \sigma \approx \sqrt{12}$).

that has a solution $w(\zeta) = F[\epsilon - s, \epsilon + s + 1, \epsilon + 1, \frac{1}{2}(1 - \zeta)]$, with $F[a, b, c, d]$ the hypergeometric function. For this solution to remain finite at $\xi \rightarrow \pm\infty$ ($\zeta = -1$), we must have $\epsilon - s = -j$, with $j = 0, 1, 2, \dots$. The energy levels are thus defined by $E = \frac{6}{\sigma^2}(j - s)^2$ or using $E = 2s_0a$,

$$\frac{a_j}{s_0} = \frac{3}{\sigma^2} \left(1 - 2j + \sqrt{1 + 2\sigma^2/3}\right)^2. \quad (2.32)$$

However, in our experiments we will be dealing with strain pulses that have a profile given to good approximation by the derivative of a Gaussian. Thus we want to relate the estimate of Eq. (2.32) to the initial condition

$$s(y, 0) = \frac{\sqrt{2e}}{l_g} s_0 y \exp(-y^2/l_g^2), \quad (2.33)$$

that is normalized to s_0 at its maximum at $y = l_g/\sqrt{2}$. In the spirit of Eq. (2.20), we should normalize the area under the square root of the waveform Eq. (2.33) to that of the sech^2 -potential to obtain the dimensionless form $\phi(\xi)$. This amounts to the redefinition of the pulse width as $l_0 = e^{1/4}\Gamma(3/4)l_g/\pi$ ($\approx 0.50l_g$), with l_0 the

width of the pulse in the sech^2 -waveform (Γ denotes the Euler gamma-function). By replacing this length scale in Eq. (2.33), normalizing to s_0 , and transforming to $\xi = y/l_0$ we obtain the correct form of $\phi(\xi)$, and the associated σ for calculation of the number of solitons in Eq. (2.32).

Note that, for comparison with experiments, we use in the rest of this thesis a boundary value problem instead of an initial value problem, that is equivalent to Eq. (2.17) after a transformation $t \rightarrow z/c_0, z \rightarrow c_0 t$. The description in this chapter was however presented in the form of an initial value problem for the purpose of compatibility with the existing literature [13, 14, 16, 18].

Figure 2.3 shows the development of a typical initial waveform given by Eq. (2.33), in the situations of nonlinear propagation in absence and presence of the third-order dispersion. The dispersionless case results in the formation of shock fronts, the compressional phase of the bipolar wavepacket travelling slightly faster and the rarefaction phase slightly slower than the linear velocity of sound. This situation will be discussed in Sec. 2.5. The trace including the dispersion shows the development of a soliton pulse in the leading part and a oscillating tail in the trailing part of the bipolar initial wavepacket. The parameters α, β were chosen so that the similarity parameter for the compressional part equals $\sigma \approx \sqrt{12}$, leading to only one negative eigenvalue λ . The radiative tail is associated with the continuum of positive energy states of the scattering problem, Eq. (2.26). Although analytical expressions for this tail exist in the case of linear dispersive waves [13, 16], no simple form is known for the combination of nonlinearity and dispersion in the wavepacket propagation.

2.5 Shock-wave development

In practice, except at the lowest temperatures, acoustic waves are attenuated by scattering at thermal phonons during propagation through a crystal. Classically, scattering can be accounted for by including a viscosity term in the wave equation [6]

$$s_t + \frac{\alpha}{2\rho c_0} s s_y - \epsilon s_{yy} + \beta s_{yyy} = 0 \tag{2.34}$$

$$s(y, t' = 0) = s_0 \phi(y) .$$

The combination of nonlinearity, dispersion, and viscosity terms in the wave equation is called the Korteweg-de Vries-Burgers (KdV-Burgers) equation. Unlike the

KdV-initial value problem, this is not an integrable equation and a solution can only be obtained numerically. For special situations, however, we may neglect either one of the three constituent terms and recover either the KdV-, Burgers- or a linear wave equation. At this point we will consider the problem of a small dispersion relative to the viscosity. Neglecting the dispersive term, one recovers the Burgers equation that can be solved in an analytical way [16]. Starting from the Burgers equation in the form $s_t + \frac{1}{2}(s^2)_y = \nu s_{yy}$ one can apply the Cole-Hopf transformation $s = -2\nu u_y/u$ to arrive at

$$u_\tau = \nu u_{\xi\xi}. \quad (2.35)$$

This is the well-known heat equation, that has solutions that spread out diffusively with time [16]. The development of the initial wavepacket depends on the relative magnitude of the nonlinearity and dispersion, as contained in the parameter $\nu = c_0\epsilon/\alpha$. The most relevant case for this thesis is the condition that nonlinearity dominates the wavepacket development. In the extreme case, when viscosity is neglected, the initial shape develops until an infinitely sharp wavefront is formed. For an initially symmetric bipolar waveform it can be shown that, in the limit $y \rightarrow \infty$, it develops into a shape of the form [16]

$$s(t, y) = \begin{cases} y/t & -\sqrt{2A_0t} < y < \sqrt{2A_0t} \\ 0 & |y| > \sqrt{2A_0t} \end{cases}, \quad (2.36)$$

where A_0 denotes the area under the positive phase of the initial waveform. The solution for a bipolar wavepacket after a long time in the case of nonzero viscosity can be found using the solution of Eq. (2.35)

$$s(y, t) = \frac{y}{t} \frac{\sqrt{a/t} \exp(-y^2/4vt)}{1 + \sqrt{a/t} \exp(-y^2/4vt)}. \quad (2.37)$$

The typical form of a so-called N-wave is shown in Fig. 2.3. This expression can be scaled to the initial waveform of Eq. (2.33) via the area under one of its phases, $A_0 = 2\nu R_0$, where we have introduced an initial Reynolds number $R_0 = \log(1 + \sqrt{a/t_0})$. The characteristic property of Eq. (2.37) is the scaling of the main profile (i.e. the N-structure) over $y = (2A_0t)^{-1/2}$, combined with a smearing out of the shock front over a distance $\Delta y = R_0^{-1} \log t/t_0$. Further, the integral under each phase of the bipolar wavepacket decays by dissipation through the viscous term as $A(t)/A_0 = \log(1 + \sqrt{a/t} - \exp R_0)$.

References

- [1] A. E. H. Love, *Treatise on the Mathematical Theory of Elasticity* (Cambridge University Press, 1937).
- [2] F. D. Murnaghan, *Finite Deformations of an Elastic Solid* (John Wiley & Sons, 1951).
- [3] D. J. Korteweg and G. de Vries, *Philos. Mag.* **39**, 422 (1895).
- [4] N. J. Zabusky and M. D. Kruskal, *Phys. Rev. Lett.* **15**, 240 (1963).
- [5] D. C. Wallace, *Solid State Physics* (Academic Press, 1970), vol. 25, p. 301.
- [6] B. A. Auld, *Acoustic Fields and Waves in Solids*, vol. 1 (Robert E. Krieger Publishing Company, 1990), 2nd ed.
- [7] C. Kittel, *Introduction to Solid State Physics* (John Wiley & Sons, 1986), 6th ed.
- [8] H.-Y. Hao and H. J. Maris, *Phys. Rev. B* **64**, 064302 (2001).
- [9] E. Fermi, J. Pasta, and S. Ulam, *Tech. Rep. LA-1940*, Los Alamos (1955).
- [10] M. Toda, *Theory of Nonlinear Lattices* (Springer-Verlag, 1981).
- [11] A. I. Potapov, I. S. Pavlov, K. A. Gorshkov, and G. A. Maugin, *Wave Motion* **34** (2001).
- [12] H. G. E. Meijer, Master's Thesis, University of Utrecht (2003).
- [13] V. I. Karpman, *Non-linear Waves in Dispersive Media* (Pergamon Press, 1975), 1st ed.
- [14] C. S. Gardner, J. M. Greene, M. D. Kruskal, and R. M. Miura, *Phys. Rev. Lett.* **19**, 1095 (1967).
- [15] P. D. Lax, *Comm. Pure Appl. Math.* **21**, 467 (1968).
- [16] G. B. Whitham, *Linear and Nonlinear Waves* (Wiley, 1974), 1st ed.
- [17] L. D. Landau and E. M. Lifschitz, *Quantum Mechanics, Non-relativistic Theory* (Pergamon Press, 1965), 2nd ed.
- [18] K. Naugolnykh and L. Ostrovsky, *Nonlinear Wave Processes in Acoustics*, Cambridge Texts in Applied Mathematics (Cambridge University Press, 1998), 1st ed.

CHAPTER 3

DETECTION OF MODELOCKED STRAIN WAVEPACKETS BY BRILLOUIN SCATTERING

Abstract

We employ Brillouin spectroscopy to study the propagation in lead molybdate of ultrashort acoustic wavepackets created by absorption of subpicosecond optical pulses in a thin-film metallic transducer. The development of the acoustic power spectrum during traversal of the wavepacket is studied at frequencies up to 8 GHz. Diffraction of the Fourier components of the acoustic wavepacket in the crystal can be monitored in the spectral domain via the spectral width, or in real-space using scans transverse to the beam. Results at helium temperatures show pump intensity dependent propagation effects, which are precursors for soliton development.

3.1 Introduction

In the last decade, many studies have been conducted on the propagation of strain pulses in thin-film structures covered with a metallic transducer, where the optical skin depth limits the time resolution of the experiment [1–3]. Only very recently, explorative work has appeared to examine the propagation of picosecond acoustic pulses in bulk crystalline materials [4], although a metallic transducer fixed at the surface of the crystal remains necessary for probing the development of the wavepacket. Frequency domain techniques in the bulk have been used recently to study low amplitude, monochromatic coherent phonons [5–7]. We demonstrate that ultrashort, broadband acoustic pulses can be studied as well in the bulk of a transparent crystal by means of frequency domain techniques. We use Brillouin scattering to monitor the selected frequency components as they develop during the propagation of the acoustic wavepacket. For an introduction to the principles

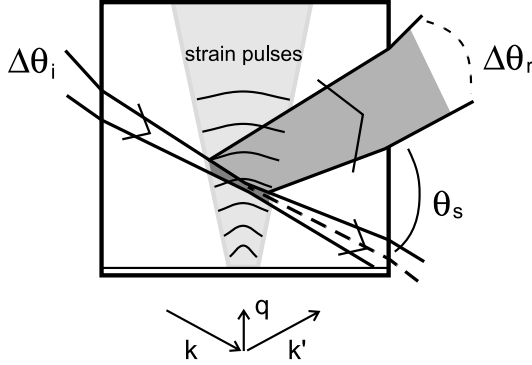


FIGURE 3.1 Scattering configuration in the crystal, showing the diverging strain pencil, argon-ion laser beams, and wavevector selection rule $\vec{k}' = \vec{k} + \vec{q}$. Also shown are the definitions of scattering angle 2θ and angular width profiles $\Delta\theta_i$, $\Delta\theta_s$ (see Sec. 3.3.3).

of Brillouin scattering we refer to the existing literature [8]. The typical scattering process is depicted in Fig. 3.1. A plane acoustic wavepacket reflects a minute fraction of an incoming laser beam, which for anti-Stokes Brillouin scattering is Doppler shifted upward, and for Stokes shifted downward, by the phonon frequency corresponding to the scattering wavevector. Conservation of wavevector and energy in the inelastic scattering process results in the following selection rules:

$$\begin{cases} \vec{k}' = \vec{k} + \vec{q} \\ \omega' = \omega + \Omega \end{cases} \Rightarrow \Omega = 2c_0k \sin \theta_i, \quad (3.1)$$

where \vec{q}, Ω denote the wavevector and energy of the phonon involved in the scattering process, \vec{k}, ω and \vec{k}', ω' denote the wavevector and energy of the incident and reflected optical radiation, respectively. Equation (3.1) implies that, for each scattering angle, we are sensitive to a *single* Fourier component of the acoustic wavepacket. The condition for wavevector conservation is, of course, relaxed by some amount due to the limited size of the interaction volume, formed by the spatial overlap volume of the focused Brillouin laser beam and the acoustic pencil. As a consequence, the observed spectral width of the Brillouin signal contains direct information on the transverse width of the acoustic beam for the selected frequency component, provided that the opening angle of the detection setup is sufficiently large.

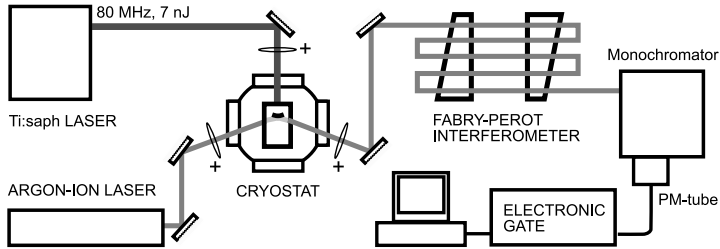


FIGURE 3.2 Experimental setup for Brillouin scattering, showing lasers, optical cryostat, Fabry-Pérot interferometer and electronic equipment.

3.2 Experimental details

The sample is a $10 \times 4 \times 5\text{-mm}^3$ single crystal of lead molybdate (PbMoO_4), with the crystallographic c -axis aligned perpendicular to the $10 \times 4\text{ mm}^2$ surface. A 600-nm thin gold transducer is deposited onto this surface, with a 5-nm buffer layer of Cr for better adhesion. Lead molybdate is a widely used medium for acousto-optic modulators and has been chosen by us mainly for its very high acousto-optic coupling parameter [9]. Given the sound velocity in the [001] direction of 3.64 km/s and the index of refraction of 2.26, the maximum frequency that can be detected by Brillouin scattering is limited to 32 GHz at a laser wavelength of 514.5 nm.

The experimental setup is shown in Fig. 3.2. Longitudinal acoustic wave-packets are created by absorption of light in the gold film from a mode-locked Ti-sapphire femtosecond laser beam, focused to a Gaussian spot with a waist of $\sim 15\text{ }\mu\text{m}$. The thickness of the acoustic pulse created in a metallic film is determined by the nonequilibrium electron transport distance, reached within the relaxation time of a few picoseconds, and amounts in gold to, say, 150 nm [3, 10]. The local acoustic strain for the selected Fourier components is detected by Brillouin scattering, employing a single-mode argon-ion laser at 514.5 nm and with 60 mW optical output power. We focus the probe laser beam in the crystal tightly to a waist of a few micrometers [see Fig. 3.1]. The frequency-shifted, scattered radiation is analyzed by a quintuple-pass Fabry-Pérot interferometer (Burleigh RC110) and detected using standard photon counting techniques. The spectrometer is equivalent to the one used earlier to study the propagation of coherent, monochromatic phonon beams in lead molybdate and paratellurite [5–7].

Damping of monochromatic, low-amplitude gigahertz phonon beams has been studied previously in lead molybdate by Damen *et al.* [6] and was found to correspond at liquid-helium temperatures to mean free paths much larger than the crystal dimensions.

3.3 Experiments in lead molybdate

3.3.1 Acoustic power spectrum

First, the input Fourier spectrum of the wavepacket was determined at room temperature, by measuring the diffracted intensity $100\ \mu\text{m}$ behind the transducer at various scattering angles. In the experiments of this chapter, the metal film was excited from the crystal-side, which resulted in a significantly higher intensity than from the helium-side. We attribute this to the significantly larger absorption coefficient of the thin chromium buffer layer at the optical wavelength. The observed power spectrum is shown in Fig. 3.3(b). The resolution is limited to $\sim 0.3\ \text{GHz}$, by the width of the cone of diffracted radiation emitted by the small interaction volume (see Sec. 3.3.2). We observe 3 broad bands, that can be fit reasonably well to the power spectrum of the typical strain wavepacket shown in Fig. 3.3(a), assuming a sound velocity in the gold film of $\sim 2.6\ \text{km/s}$. This value lies between the bulk velocity for polycrystalline gold, of $1.7\ \text{km/s}$, and the maximum value of $3.24\ \text{km/s}$, in the crystalline [001] direction. Disagreement between simulated and experimental spectra exists mainly in the exact position of the 3 bands in the spectrum. For the simulated waveform, these frequencies are determined by the resonances of the gold film to values of $\nu_n = nc_0/2d$, with n the number of the harmonic, c_0 the sound velocity and d the film thickness. The deviations of the experimentally obtained peak positions may be due to a thermal lensing effect in the crystal, resulting from the heat radiated by the metal film. This causes a slight angle-dependent distortion of the path of the incident argon-ion laser beam close to the transducer. In the experiments performed at low temperatures, described later in this thesis, this deflection was strongly reduced by the efficient cooling of the crystal.

3.3.2 Spectral mode-structure

A typical Brillouin spectrum of the acoustic wavepacket, at a scattering angle of $2\theta \approx 40^\circ$, is presented in Fig. 3.4(a). The spectrum consists of a Gaussian enve-

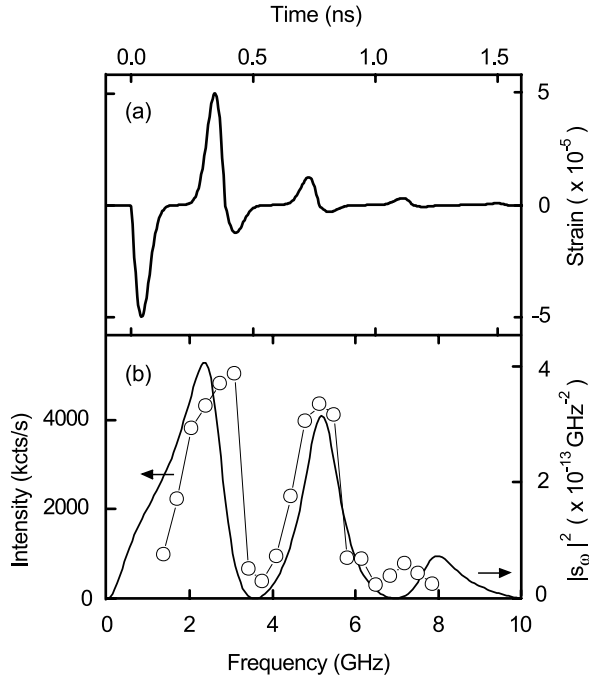


FIGURE 3.3 (a) Strain wavepacket calculated for the crystal-side excitation geometry. (b) Frequency spectrum of the acoustic wavepacket (○) Experimental data, (line) power spectrum of the wavepacket of (a).

lope containing a number of narrow peaks at multiples of the 75.4 MHz repetition frequency of the Ti-sapphire laser, centered around a Doppler shifted frequency of ~ 3.3 GHz. The spectral resolution is limited by the finesse of the interferometer to a value of 20 MHz, at the free spectral range of 1.06 GHz. As the mutual distance between the acoustic wavepackets, as they travel through the sample, is larger than the size of the detection volume, the mode structure in the measured spectrum must be caused by optical interference *inside* the interferometer of light scattered by subsequent acoustic pulses traversing the interaction volume. In this way the Fabry-Pérot interferometer acts as a periodic cross-correlator of the optical signal over the round-trip time of $2L/c \approx 1$ ns, and with a 'memory' limited by the finesse to about 50 ns. The measured phase relationship of the scattered radiation over this time implies that we are dealing with a *mode-locked acoustic pulse train*.

Figure 3.4(b) shows the sum of the peak intensities in the mode spectrum as a function of intensity of the pump laser. Clearly, the dependence of the Brillouin intensity on excitation power shows a quadratic behavior over the whole dynamic range. This demonstrates that the generated strain in the gold film in the measured frequency window depends linearly on pump power. The Brillouin intensity of a single spectral mode can be compared quantitatively with the thermal background of LA phonons in the detection bandwidth of 20 MHz. In the absence of coherent wavepackets, we find a thermal phonon signal of ~ 500 cts/s. In Fig. 3.4(a), the scattered yield from the component at 3.3 GHz is 10^3 times larger than this value, which can be directly translated to an occupation number $n_\omega \approx 1 \times 10^3 (k_B T / \hbar \omega) = 3 \times 10^6$, or a mode temperature exceeding 10^5 K.

From the estimate of the occupation number it is a small step to the approximation of the average displacement and the acoustic strain contained in the individual spectral modes. It is well known that for a harmonic oscillator, the average energy is equally distributed over the potential and kinetic parts, $U = T = \frac{1}{2} \hbar \omega (n_\omega + \frac{1}{2})$. Combined with the expression for the potential energy $U = \frac{1}{2} M \omega^2 \langle \bar{u}_\omega^2 \rangle$, and the number of oscillators given by the Debye density of states $D(\omega) \Delta \omega$, we obtain the expression for the average wave amplitude \bar{u}_ω , given by

$$\bar{u}_\omega = \left(D(\omega) \Delta \omega \frac{(n + \frac{1}{2}) \hbar}{M \omega} \right)^{1/2}. \quad (3.2)$$

As we are dealing with a very directional beam of phonons, the complete, 3-dimensional density of states will hugely overestimate the number of participating oscillators. We therefore take into account only a cone of wavevectors, with a top angle defined by the acceptance angle of the detector, $\theta_0 = 50$ mrad (see Sec. 3.3.3). Integration over only this part of phase space yields a more realistic density of states $D(\omega) \Delta \omega \approx V \omega^2 \theta_0^2 \Delta \omega / 4\pi c_0^3$.

From Eq. (3.2) we can obtain the associated strain $\bar{s}_\omega = \partial \bar{u}_\omega / \partial x$ by multiplication with ω / c_0 . For our example at 3.3 GHz, this results in a displacement of $\bar{u}_\omega = 5 \times 10^{-15}$ m, or an acoustic strain $\bar{s}_\omega = 3 \times 10^{-8}$, over a bandwidth of 75.4 MHz. We can even go further and gauge the overall spectrum of Fig. 3.3(b) to this value. The calibrated scale for the power density $|\bar{s}_\omega|^2$ is shown on the right side of this graph. The inverse Fourier transform of this calibrated spectrum, finally, results in an estimate of the coherent strain amplitude of 5×10^{-5} for an excitation power of ~ 2 mJ/cm², as shown on the right-hand scale of Fig. 3.3(a).

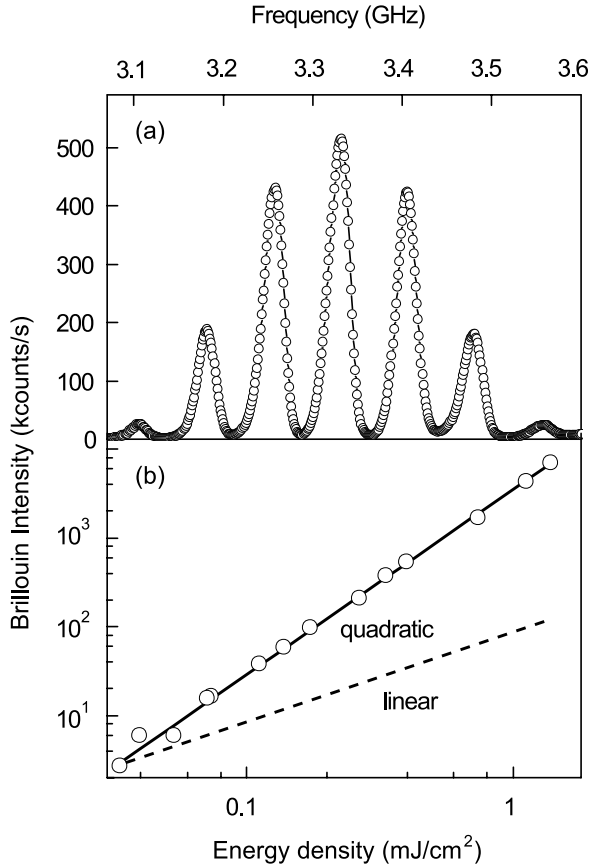


FIGURE 3.4 (a) Brillouin spectrum observed at a scattering angle $2\theta = 20^\circ$, at a pump fluence of 0.5 mJ/cm^2 . The width of the peaks is limited by the resolution of the spectrometer. (b) dependence of the integrated Brillouin intensity at 3.2 GHz , measured at $100 \mu\text{m}$ distance from the transducer, on excitation power, showing a quadratic dependence over 2 orders of magnitude.

3.3.3 Relation between spatial and spectral width

To determine the relation between the Gaussian spectral envelope, as shown in Fig. 3.4(a), and the spatial strain profile, we set up an experiment to independently measure these quantities. Information on the transverse strain profile was obtained by transverse scans of the acoustic pencil through the detection volume, while the spectral width was obtained directly from the interferometer scans. The diameter

of the excitation spot on the metal film was varied by translation of the focusing lens of the pump laser. The resulting values for spatial and spectral widths of the Brillouin intensity are shown in Fig. 3.5(a) and (b), respectively. Clearly, an increase in size of the phonon beam is accompanied by a reduction of the bandwidth of the Brillouin spectrum.

The spatial width of the strain profile $w_{\text{ph}}(z)$ can be explained by the divergence of the Gaussian pump laser [line in Fig. 3.5(a)], for a minimal waist $w_{\text{ph}}(0) = 17.1 \pm 0.2 \mu\text{m}$. The spectral distribution of Brillouin-scattered intensity has been derived by Damen [11] as $|E_s/E_0|^2 \propto \exp(-\frac{1}{2}q^2\Delta\theta^2w_{\text{ph}}^2)$, with $q = 2k \sin\theta_s/2$ the scattering vector, $\Delta\theta_s$ the deviation in angle from the specular condition [see Fig. 3.1], and w_{ph} the $1/e$ half-width of the acoustic strain profile. Together with the frequency-angle relation for small angles, $\Delta\nu = c_0k\Delta\theta_s/\pi$, this yields for the spectral halfwidth $\Delta\nu$ the expression

$$\Delta\nu \approx \frac{\sqrt{2}c_0}{\pi w_{\text{ph}}(z)}. \quad (3.3)$$

We used this approximation to calculate the spectral width associated with the experimentally obtained values of w_{ph} of Fig. 3.5(a) [marked \times in Fig. 3.5(b)]. We find only qualitative agreement with the experimental behavior: the spectral bandwidth decreases for increasing spatial width. The quantitative disagreement is believed to be a direct consequence of a compromise made in the imaging of the detection volume onto the interferometer. The limited aperture of the Fabry-Pérot allows for only specific combinations of opening angle and beam diameter, conserving the product $d\Delta\theta$, with d the diameter of the detection volume. Our choice of imaging results in a combination of $d \approx 50 \mu\text{m}$ and horizontal opening angle $\Delta\theta \approx 0.05$ rad, corresponding to a bandwidth of 800 MHz. Further, the tight focusing of the argon-ion laser beam introduces an additional distribution of angles in the scattering process, that acts as an offset in Fig. 3.5(b). We try to correct for the clipping of the high frequencies and angular spread of the argon laser by using the simple model equation

$$\Delta\nu_c = \left(\frac{1}{\Delta\nu + A} + \frac{1}{B} \right)^{-1}, \quad (3.4)$$

with A the offset and B the high-frequency cutoff. Application of this correction scheme to the values derived from the spatial profiles gives agreement with the directly measured bandwidth for values of $A = 90 \pm 10$ MHz and $B = 800 \pm$

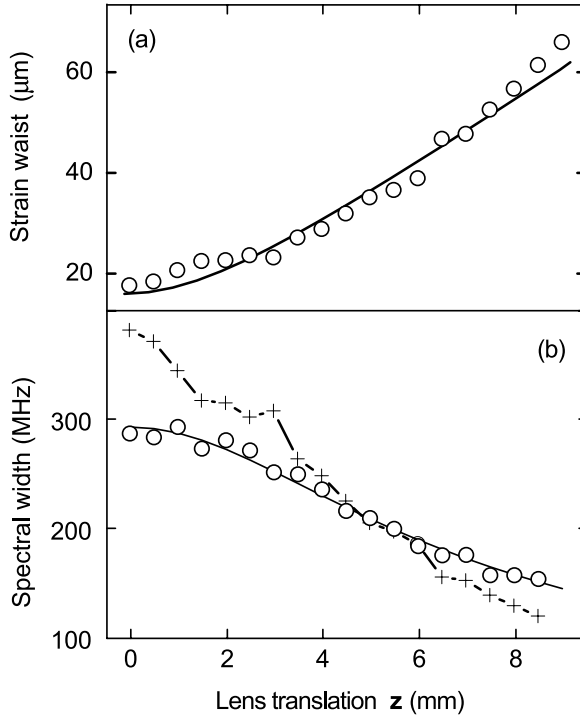


FIGURE 3.5 (a) Spatial 1/e halfwidth of the phonon beam at 3.3 GHz against translation of the focusing lens of the pump laser. (o) experimental data, (line) fit to data assuming Gaussian beam divergence. (b) Spectral 1/e halfwidth of the Brillouin scattered intensity for same settings as in (a). (o) experimental data, (x) derived from (a) using Eq. (3.3), and (line) after correction by Eq. (3.4).

50 MHz [line in Fig. 3.5(b)].

From the data of Fig. 3.5(a,b) we have observed a clear correlation between spectral width and the spatial strain profile. However, next to the phonon beam profile, the spectral width turns out to be determined also by the size of the probe beam and the opening angle of the detector. Further, the fourier spectrum of the wavepacket [see Fig. 3.3(b)] shows strong variations over gigahertz frequencies, which will distort the connection between spatial and spectral properties as well. In conclusion, the spectral width is unreliable for a quantitative analysis of the beam profile.

3.3.4 Propagation of a single strain component

Once an acoustic mode is selected by means of its associated scattering angle, it can be easily followed over long distances in the crystal by translation of the cryostat. For our example at 3.3 GHz, we measured the transverse profile at several travelled distances z at room temperature. The obtained $1/e$ halfwidth of the Gaussian profiles is shown in Fig. 3.6(a) and shows broadening due to Fraunhofer diffraction. After accounting for phonon focusing, the expression for the divergence of a gaussian strain profile reads [7]

$$w_{\text{ph}}(z) = w_0 \left(1 + \left(\frac{z}{z_0} \right)^2 \right)^{1/2}, \quad (3.5)$$

$$z_0 = \frac{\pi w_0^2}{\lambda_0} (1 - 2p), \quad (3.6)$$

where $\lambda_0 = 2\pi/q_0$ denotes the selected phonon wavelength and z_0 the Rayleigh distance, over which the acoustic pencil increases by a factor of $\sqrt{2}$. The phonon focusing parameter equals $p = +0.174$ for lead molybdate around the [001]-direction. Excellent agreement is obtained with the experimentally observed divergence and Eq. (3.5) [line in Fig. 3.6(a)] for $w_0 = 20.2 \pm 0.2 \mu\text{m}$ and $\lambda_0 = 1.09 \mu\text{m}$, which indeed corresponds to a 3.34-GHz phonon frequency. The divergence angle of the phonon beam follows from Eqs. (3.5) and (3.5) as $\theta_0 = w_0/z_0$ and amounts to 25 mrad for the frequency component of Fig. 3.6(a).

Integration of the Brillouin signal over the transverse coordinate gives the total acoustic power, which is shown versus propagation distance z in Fig.3.6(b). The decay can be fit by a single exponential function with a relaxation length of $225 \mu\text{m}$, in agreement with the theory and previous experiments for phonon attenuation at room temperature [11]. Note that this method of integration is valid only for phonon beams less than $\sim 40 \mu\text{m}$, the typical width of the detection volume. For broader beams, the energy that falls outside this region will not be detected and therefore a reduced total power will be observed.

Experiments at liquid helium temperatures are necessary to eliminate thermal damping effects, thus enabling the study of propagation over much longer distances and at lower pump intensities. Preliminary results for the 3.3-GHz frequency component indicate a strong dependence of both the divergence (not shown) and the acoustic power (inset of Fig. 3.6(b) on the pump intensity. The rapid decay of the total intensity at the highest pump powers may be explained

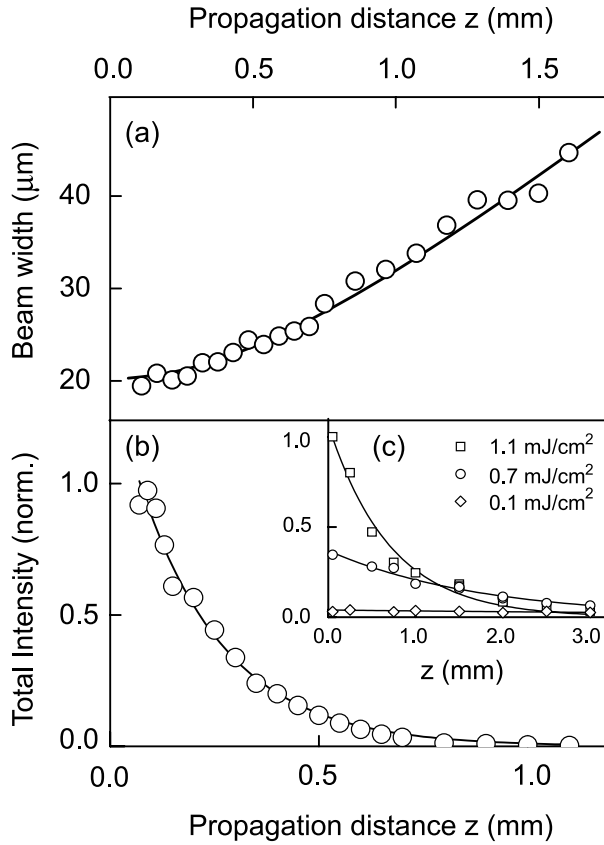


FIGURE 3.6 (a) Acoustic beam width at 3.3 GHz (\circ) as a function of propagation distance in the crystal at room temperature. (Line) fit to data using Eq. (3.5). (b) Integrated Brillouin intensity at 3.3 GHz (\circ) as a function of propagation distance at room temperature, (line) theoretical fit to data using exponential decay. (c) Brillouin intensity as a function of propagation distance z at 15 K for three different pump intensities.

by an increase in coupling between acoustic modes, due to the high local strain around the wavepacket maximum. We observed this population decay to be even more pronounced at lower acoustic frequencies, around 1 GHz (not shown), suggesting the presence of an upconversion effect, which may be interpreted as the self steepening of the acoustic wavepacket and a precursor of soliton formation. Further investigation into the power dependence of these effects and of diffraction will be presented later on in this thesis.

3.4 Conclusions

In summary, we have presented the first experiments on picosecond strain wavepackets using Brillouin scattering as a local probe of acoustic frequency components. We obtain integrated intensities of up to 10^7 photons per second, which is sufficient to do sophisticated experiments. The wavepacket spectrum could be measured up to 8 GHz in lead molybdate, and was gauged against the scattered intensity of the thermal phonon background. Furthermore, a fine-structure in the acoustic spectrum on the scale of the 75.4 MHz repetition frequency was revealed, demonstrating the phase relation between subsequent strain pulses. Propagation over millimeter distance at room temperature is consistent with the linear theory of Fraunhofer diffraction and thermal damping for the acoustic wavevector selected by the scattering geometry. At low temperatures, the propagation could be monitored over much longer distances in the crystal. The anomalies in the propagation at this regime may serve as a starting point for the investigations presented in the following chapters.

References

- [1] C. Thomsen, H. T. Grahn, H. J. Maris, and J. Tauc, *Phys. Rev. B* **34**, 4129 (1986).
- [2] T. F. Crimmins, A. A. Maznev, and K. A. Nelson, *Appl. Phys. Lett.* **74**, 1344 (1999).
- [3] D. H. Hurley and O. B. Wright, *Opt. Lett.* **24**, 1305 (1999).
- [4] H.-Y. Hao and H. J. Maris, *Phys. Rev. Lett.* **84**, 5556 (2000).
- [5] E. P. N. Damen, A. F. M. Arts, and H. W. de Wijn, *Phys. Rev. Lett.* **75**, 4249 (1995).
- [6] E. P. N. Damen, A. F. M. Arts, and H. W. de Wijn, *Phys. Rev. B* **59**, 349 (1999).
- [7] E. P. N. Damen, D. J. Dieleman, A. F. M. Arts, and H. W. de Wijn, *Phys. Rev. B* **64**, 4303 (2001).
- [8] J. W. Tucker and V. W. Rampton, *Microwave Ultrasonics in Solid State Physics* (North-Holland Publishing Company, 1972), 1st ed.
- [9] G. A. Coquin, D. A. Pinnow, and A. W. Warner, *J. Appl. Phys.* **42**, 2162 (1971).
- [10] G. Tas and H. J. Maris, *Phys. Rev. B* **49**, 15046 (1994).
- [11] E. P. N. Damen, PhD Thesis, University of Utrecht (1993).

CHAPTER 4

HIGH-AMPLITUDE, ULTRASHORT, LONGITUDINAL STRAIN SOLITONS IN SAPPHIRE

Abstract

We demonstrate the development of high-amplitude picosecond strain pulses in a sapphire single crystal into an ultrafast compressional soliton train. For this purpose, large-intensity light pulses were used to excite a metal film, yielding a two-orders of magnitude higher strain than that achieved in earlier studies. Propagation of the packets is monitored over a distance of several millimeters by means of Brillouin light-scattering. This yields a complicated oscillation pattern of the scattered intensity, that is interpreted in terms of optical interference and Bragg-resonances of light reflected from the solitons moving at different velocities. A one-parameter model, based on the Korteweg-de Vries-Burgers equation, simultaneously explains the observed behavior at all strains and temperatures under study. We predict up to 11 solitons in the train, reaching pressures as high as 20 kbar and 0.5 ps temporal widths.

4.1 Introduction

After the successful application of the Brillouin-scattering method in the detection of ‘modelocked’ strain wavepackets, as described in Chapter 3, we extend this detection method to the regime of acoustic wavepackets of very high amplitude in sapphire. Picosecond, planar strain pulses are generated thermoelastically in a metal film using excitation by an amplified femtosecond laser. From the experiments by Hao *et al.* [1] it is known that, at moderate strains, high-frequency wavepackets will experience sufficient nonlinearity to compensate for phonon dispersion, resulting in strain solitons of compression. In this chapter we present results demonstrating the development of a train of ultrashort strain solitons, reaching

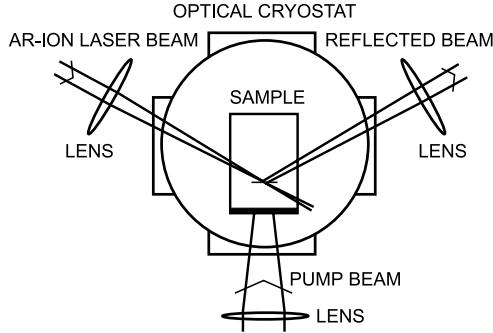


FIGURE 4.1 Top view of the Brillouin scattering configuration in the crystal, showing the optical cryostat that contains a single crystal sapphire. Arrows indicate the directions of the femtosecond pump laser beam and incident and reflected probe light.

amplitudes up to 0.4% and 0.5 ps temporal widths [2].

4.2 Experimental setup

We increase the strain amplitude of the wave packets injected from the metal transducer, relative to those in conventional picosecond ultrasonics, by two orders of magnitude using excitation by an amplified ultrafast Ti:sapphire laser system (Spectra Physics ‘Hurricane’). The output beam of the laser carries 0.75 mJ per pulse at a repetition rate of 1.0 kHz and is loosely focused to a spot of several millimeters in diameter onto the sample. For the propagation experiments we use a piece of high-quality (< 1 at. ppm. impurity ions) single-crystal sapphire of $5 \times 11 \times 10\text{-mm}^3$ dimensions, with the c -axis aligned perpendicular to the $5 \times 11\text{-mm}^2$ surface. A 1000-\AA chromium film is deposited onto this surface. The crystal is mounted into an optical cryostat to perform experiments down to liquid helium temperatures. The optical pump fluence is varied by changing the position of the focusing lens, the upper limit being the damage threshold of our transducer at $\sim 15\text{ mJ/cm}^2$.

Transient changes of the refractive index due to the presence of the acoustic wave packets are detected by means of Brillouin scattering, as explained in Chapter 3. Momentum conservation in the scattering process selects a narrow band of Fourier components of the acoustic wave packet. The frequency-shifted optical beam is analyzed with a quintuple-pass Fabry-Pérot interferometer and detected

by a photon-counting system. This setup has been used in Chapter 3 to observe modelocked acoustic wave packets [3] and was used earlier to study coherent, monochromatic phonon beams [4, 5]. One of the obvious technical difficulties with respect to the configuration of Chapter 3 is the dramatic decrease in duty-cycle by a factor of 7.54×10^4 by the replacement of the modelocked laser by the regenerative amplifier. Indeed a significantly lower scattering yield, of the order of 10 – 100 cts/s, was obtained, which fortunately turned out to be sufficient to perform the detailed experiments described in the following sections. Spurious background intensity due to elastic scattering and detector noise could be efficiently suppressed using electronic time gating of the arriving counts.

Brillouin scattering is the ideal technique to study the development of the wavepacket into soliton trains in transparent crystals because the propagation distance can be continuously varied and the expected spatial walk-off between the solitons corresponds to wavevectors around the typical scattering wavevector, yielding excellent sensitivity. We have chosen to focus the Brillouin laser beam tightly to a waist of $\sim 4 \mu\text{m}$, to achieve an optimal spatial resolution for detection along the propagation direction. Acoustic frequency components up to ~ 30 GHz in sapphire can be studied with 514-nm light using the scattering configuration through the side-windows of the cryostat [see Fig. 4.1]. Our choice of the metal transducer guarantees an initial wave packet with gigahertz components [6]. The excellent attachment of chromium to sapphire and the small acoustic mismatch results in an acoustic reflection coefficient at the interface of only 10%. A typical power spectrum, obtained by measuring the Brillouin intensity at a distance of $50 \mu\text{m}$ behind the transducer, for several scattering angles, is shown in Fig. 4.2(a). For comparison, the vertical scale is normalized to the spectrum of the initial wavepacket used in the simulations of the following sections [c.f. Fig. 4.2(b)].

4.3 Numerical simulations

Numerical simulations of the Korteweg-de Vries-Burgers (KdV-Burgers) equation were performed using a discrete, implicit scheme of second order accuracy and three-level quadratic approximation in time [7] (see Appendix A). In those cases where solitons were formed, part of the simulation was further evolved using the analytical methods for soliton trains described in Sec. 2.4 of this thesis. In all calculations, we use the known parameters for the elastic constants of second- and third order and the phonon dispersion around the c -axis of sapphire [8].

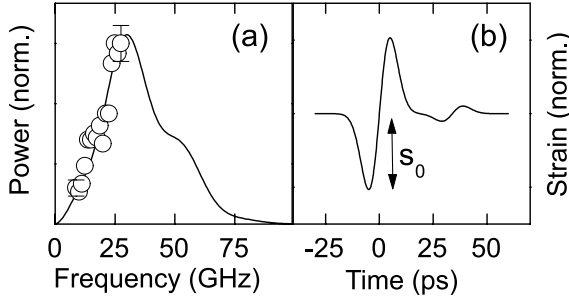


FIGURE 4.2 (a) Power spectrum of the initial wave packet used in simulations, with Brillouin intensity (points) obtained at different scattering angles. (b) Initial waveform used in simulations.

4.4 Experiments at a single strain component

4.4.1 Propagation at room temperature

Figure 4.3 shows typical traces of the acoustic power vs propagation distance at 22 GHz, at room temperature and for six values of the pump fluence. Note the vertical rescaling and horizontal expansion in the figure for the first 0.5-mm propagation distance. At all fluences the Brillouin intensity initially sharply decreases with distance, followed by a weak and gentle oscillation. Simulations have been included in the figure using the KdV-Burgers equation. For the viscosity of sapphire at room temperature we took 4.54×10^{-4} Ns/m² [9]. Fitted values for the initial acoustic strain s_0 , the single adjustable parameter of the model (except for the overall amplitude), are presented as numbers in Fig. 4.3(a). Good agreement between theoretical and experimental traces is obtained for values of s_0 around 10^{-3} , which corresponds to a transient pressure of 10 kbar. These values coincide with the absolute Brillouin intensity, gauged against the measured thermal phonon background in absence of strain pulses. Further, temporal traces obtained from the simulation after a 5-mm propagation distance are included in Fig. 4.3(a), which exhibit the typical shape of the damped N-wave solution of the Burgers equation [10]. From these simulations we conclude that, at room temperature, the degree of self-steepening does not reach the critical value in order to bring dispersion into play.

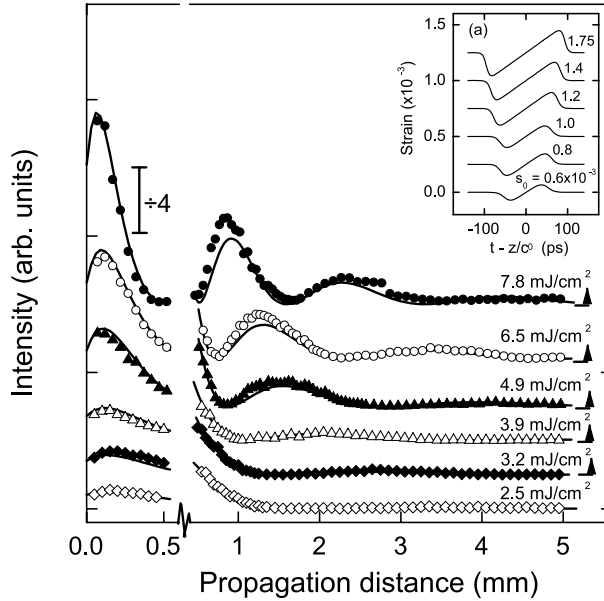


FIGURE 4.3 Acoustic power at 22 GHz as a function of propagation distance in the sapphire crystal, at room temperature. Points: experimental data. Lines: simulations. Arrows indicate vertical offsets. Up to 0.5 mm, traces have been vertically divided by 4. Inset: (a) Time-domain waveforms after 5 mm of propagation, in the moving-frame coordinate $t - z/c_0$, obtained from simulations with corresponding values of acoustic strain s_0 .

4.4.2 Temperature dependence

The propagation at intermediate temperatures is shown in Fig. 4.4 and shows the typical crossover from overdamped to virtually undamped propagation. Again, simulations have been performed successfully, by taking a linear temperature dependence of the viscosity above 100 K [5]. This makes our simulation free of adjustable parameters. The onset of fast oscillations in the propagation, between 50 K and 100 K, signifies the formation of solitons, as we will show in the following section. Simulations in the crossover regime have not been performed, because the specific anharmonic process involved in the damping is not known. At a temperature of 5 K, however, it appears that we may neglect damping completely.

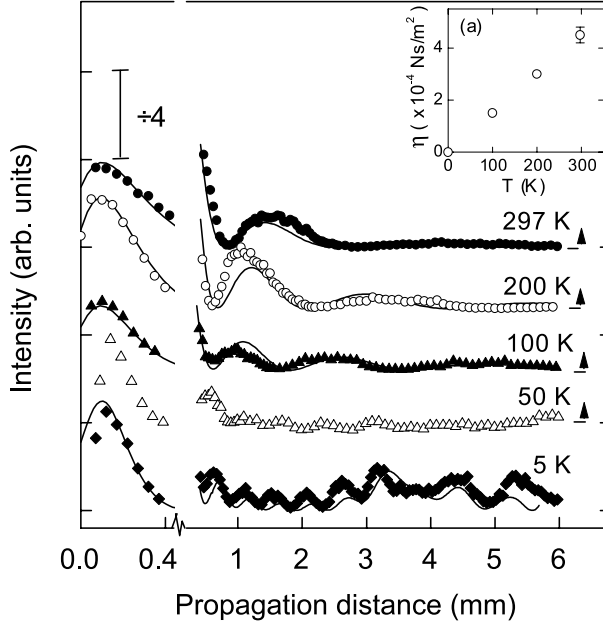


FIGURE 4.4 Traces of the 22-GHz frequency component for different temperatures, at a pump fluence of 4.9 mJ/cm^2 . Points: experimental data. Lines: simulations based on the KdV-Burgers equation. (a) Values for the viscosity η used in the simulations.

4.4.3 Propagation at low temperature

In Fig. 4.5 we present traces taken at a temperature of 5 K, again at 22 GHz and for a range of pump fluences. We observe for all curves an initial decay reminiscent of the behavior at higher temperatures, but slightly faster. Beyond a propagation distance of a few hundred micrometers, we can distinguish fast oscillations in the acoustic power, with a period decreasing with increasing pump fluence. After a propagation length of several millimeters, the characteristic oscillations become less pronounced.

At this point we show that this behavior can be accounted for by simulations using the KdV equation. In the present simulations, proper corrections were made for the input strain values to correct for the temperature-dependent absorption changes in the transducer [see Fig. 4.5(a)], leaving us again without any adjustable parameters. The calculated Brillouin intensities at 22 GHz are shown as lines in Fig. 4.5 and show a remarkable agreement up to several millimeters prop-

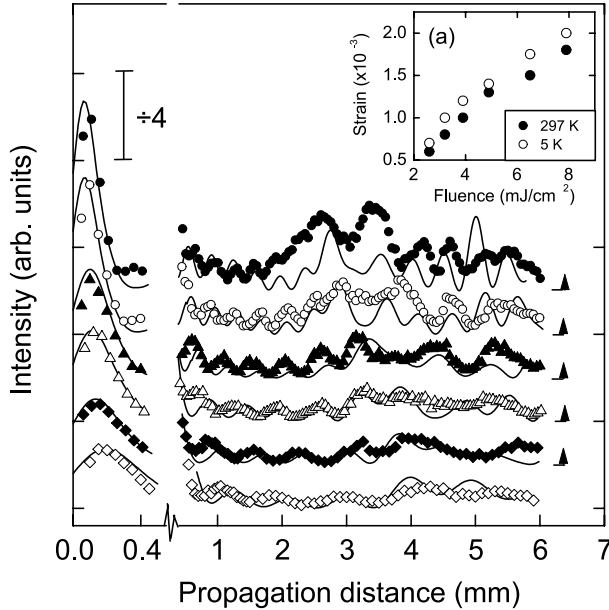


FIGURE 4.5 Scans of the 22-GHz Fourier component of the acoustic wave packet, for different pump fluences, at a temperature of 5 K. Points: experimental data. Lines: simulations based on the KdV equation. (a) Values for the acoustic strain obtained for the simulations at temperatures of 293 K and 5 K.

agation length. General features, like the initial decay, fast oscillations, and the transition from an oscillatory to a more complex behavior after several millimeters are correctly reproduced by the calculations.

4.5 Interpretation

Figure 4.6 shows the simulated successive stages of the development of the wave packet into a soliton train. Inspection of the experimental data and the simulations reveals that the initial decay of the Brillouin intensity is produced by self-steepening of the wave packet and concomitant upconversion of the acoustic energy to frequencies as high as 1 THz, i.e., far beyond the experimental window. Only at these high frequencies, phonon dispersion provides enough phase accumulation to balance self-steepening and initiates soliton formation in the leading part and the so-called radiative tail in the trailing part. The variations of the Brill-

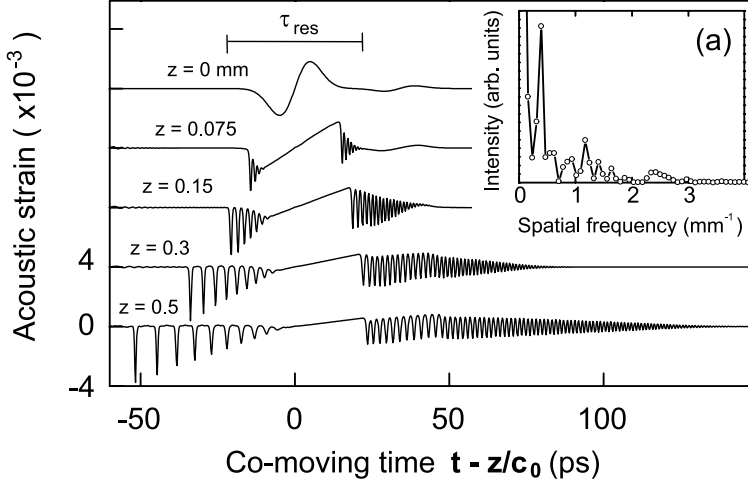


FIGURE 4.6 Time domain traces, for several propagation distances z , obtained from simulations based on the KdV equation, for an initial strain of 1.75×10^{-3} . (a) Fourier transform of experimental scan of Fig. 4.5 at 6.5 mJ/cm^2 .

loun intensity vs propagation distance can then indeed be traced back to Bragg-scattering off the soliton train, with resonance length $\tau_{\text{res}} = 1/\nu_{\text{B}}$ as indicated in the figure (ν_{B} denotes the Brillouin frequency). Two solitons of different amplitude and consequently different velocities ν_1, ν_2 would already result in one oscillation, with a period of

$$\lambda = c_0^2 / (\nu_1 - \nu_2) \nu_{\text{B}}, \quad (4.1)$$

c_0 being the sound velocity. For a velocity difference of $10^{-3}c_0$, this will give an oscillation with a period of $\lambda = 0.51 \text{ mm}$. Likewise, N solitons produce no more than $(N - 1)!$ spatial resonances. This leads to the complicated beating pattern as a function of propagation distance, as we observe experimentally. We examine in Fig. 4.6(a) the spatial Fourier-transform of one of the experimentally obtained diagrams of Fig. 4.5 and resolve at least 9 distinct contributing frequencies. This directly poses a lower limit on the number of solitons (and tail) of $N = 5$. From the simulation it can further be observed that the mutual distances between the solitons are almost equal, implying degeneracy of many spatial resonances and a reduction of the number of experimentally observable beating frequencies. The limited propagation length in our experiments unfortunately prevents an exact de-

termination of the number of solitons in the train directly from the spatial-Fourier spectrum of Fig. 4.6(a). However, accurate knowledge of all material parameters and experimental conditions allows us to define a prototype wave packet, the soliton train of Fig. 4.6, that is consistent with all our experimental data.

The bold extrapolation in the above discussion from the gigahertz Brillouin-scattering data to the terahertz characteristics of the wave packet is in our opinion justified by the excellent agreement between the experimental and computed behavior. In the problem of nonlinear wave propagation, one cannot simply separate the behavior of the high- and low-frequency components of the wave packet: they are inherently coupled and interlaced. This fact allows one to draw detailed conclusions on the evolution of high-frequency components, once the low-frequency behavior is assessed to sufficient precision as we did using Brillouin spectroscopy. A viscously damped N-wave must evolve according to a typical diffusive scaling law [10], which explains the slowing down of the oscillations in the high-temperature Brillouin data. KdV-solitons propagate with constant velocity, and therefore will exhibit a constant oscillation period in the Brillouin signal. As the KdV-soliton is a one-parameter entity, its amplitude and width follow directly from this velocity. Inelastic light scattering thus forms a unique monitor of soliton-train evolution inside a crystal, despite the fact that the solitons consist of very high frequency components, far beyond the bandwidth of a Brillouin spectrometer.

4.6 Conclusions

In conclusion, we have efficiently generated planar, high-intensity acoustic wave packets of picosecond duration, and monitored their propagation using Brillouin scattering. High-intensity optical excitation yields a two orders of magnitude higher strain and correspondingly higher conversion of absorbed energy to coherent phonons than conventional picosecond ultrasonics. Experiments at low temperature have been described successfully by the KdV equation. From these calculations, we predict the development of an acoustic soliton train of up to 11 individual solitons, reaching a strain as high as 4×10^{-3} , a subpicosecond time duration, and a 5-nm spatial width. Further measurements show that solitons can be formed at temperatures as high as 50 K. Above 100 K, damping of high acoustic frequencies completely eliminates the role of dispersion, resulting in weak shock wave formation.

Potential applications of intense subpicosecond acoustic pulses are in strain-induced chemistry and surface science, and possibly switching of synchrotron beams [11, 12]. Further, the small acoustic wavelength and highly localized energy content make ultrashort acoustic solitons a potentially suitable vehicle for patterning or imaging of nanometer-scaled objects. The feasibility to generate these pulses up to liquid nitrogen temperatures may therefore be of technological relevance. Research at even higher nondestructive excitation intensities will be possible, but require a stronger or embedded transducer. Intense subpicosecond acoustic wave packets will certainly open up new areas of fundamental research on vibrational dynamics [13] and phonon localization in glasses [14, 15]. Finally, the single-cycle pulse shape and quadratic nonlinearity provide a new and fascinating playground for fundamental studies on one- and higher-dimensional solitons, in analogy with their optical counterparts [16, 17].

References

- [1] H.-Y. Hao and H. J. Maris, *Phys. Rev. B* **64**, 064302 (2001).
- [2] O. L. Muskens and J. I. Dijkhuis, *Phys. Rev. Lett.* **89**, 285504 (2002).
- [3] O. L. Muskens and J. I. Dijkhuis, *Physica B* **316-317**, 373 (2002).
- [4] E. P. N. Damen, D. J. Dieleman, A. F. M. Arts, and H. W. de Wijn, *Phys. Rev. B* **64**, 4303 (2001).
- [5] E. P. N. Damen, A. F. M. Arts, and H. W. de Wijn, *Phys. Rev. B* **59**, 349 (1999).
- [6] O. B. Wright and K. Kawashima, *Phys. Rev. Lett.* **69**, 1668 (1992).
- [7] J. H. Ferziger and M. Perić, *Computational Methods for Fluid Dynamics* (Springer Verlag, 1999), 2nd ed.
- [8] H.-Y. Hao and H. J. Maris, *Phys. Rev. B* **63**, 224301 (2001).
- [9] B. A. Auld, *Acoustic Fields and Waves in Solids*, vol. 1 (Robert E. Krieger Publishing Company, 1990), 2nd ed.
- [10] G. B. Whitham, *Linear and Nonlinear Waves* (Wiley, 1974), 1st ed.
- [11] M. F. DeCamp et al., *Nature* **413**, 825 (2001).
- [12] A. Cavalleri et al., *Phys. Rev. Lett.* **87**, 237401 (2001).
- [13] J.-P. R. Wells, R. E. I. Schropp, L. F. G. van der Meer, and J. I. Dijkhuis, *Phys. Rev. Lett.* **89**, 125504 (2002).
- [14] B. Hehlen et al., *Phys. Rev. Lett.* **84**, 5355 (2000).
- [15] T. Nakayama, *Phys. Rev. Lett.* **80**, 1244 (1998).
- [16] X. Liu, K. Beckwitt, and F. W. Wise, *Phys. Rev. E* **62**, 1328 (2000).
- [17] W. E. Torruellas et al., *Phys. Rev. Lett.* **74**, 5036 (1995).

CHAPTER 5

INELASTIC LIGHT SCATTERING BY SOLITON TRAINS IN SAPPHIRE

Abstract

In this chapter we explore the development in sapphire of trains of acoustic solitons by measuring the Brillouin signal over a range of scattering angles. We obtain detailed new information on the relation between the acoustic frequency and the observed oscillation patterns. The interpretation in terms of spatial resonances of the moving train, developed in Chapter 4, is applied in a quantitative way to determine a soliton velocity from the spatial frequency spectrum. Estimates for the highest soliton amplitudes have been obtained that are in good agreement with the numerical simulations of the KdV equation from Chapter 4.

5.1 Introduction

In Chapter 4 we have demonstrated the formation of ultrashort strain solitons in sapphire using a direct comparison of Brillouin scattering data and numerical simulations. An attempt was made to analyze the intricate oscillation pattern in terms of spatial resonances of the solitons, but no quantitative results were obtained using this method. At this point, we will try to get information on the soliton train using only the analytical framework, i.e. without the numerical simulations. For this purpose, we have analyzed the propagation in sapphire of several frequency components of the wavepacket, in the range 10 – 26 GHz.

Next to this, we discuss in Sec. 5.2 some general properties of the Brillouin scattering method, namely the dependence of the Brillouin intensity on polarization of the probe laser beam, and the calibration against the thermal phonon signal. Finally, in Sec. 5.5, the spectral evolution of the numerical soliton packets of

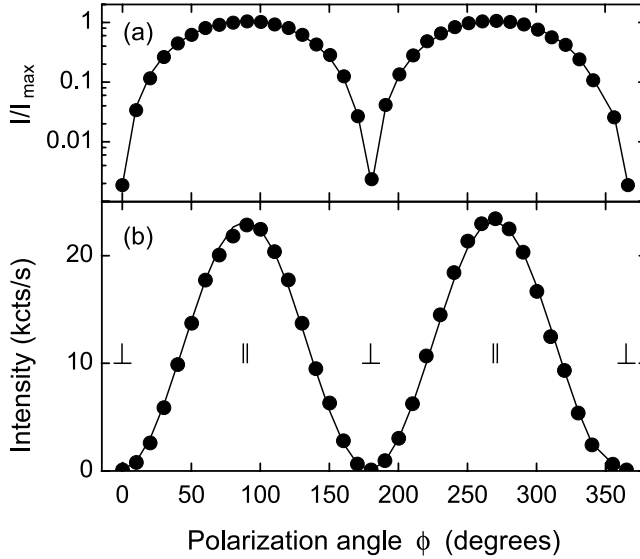


FIGURE 5.1 Dependence of Brillouin scattering signal at a frequency of 22 GHz on argon-ion laser polarization, (a) Logarithmic, normalized to maximum and (b) linear scale. (\parallel , \perp) indicate orientation of electric-field vector \vec{E} to the crystallographic c -axis

Chapter 4 is revisited, and connected with the analytical estimates of Sec. 5.4. In Sec. C.2 the role of the dispersive tail and solitons in the low-frequency Brillouin scattering experiment is studied.

5.2 General observations

5.2.1 Polarization dependence

It is well-known that the elasto-optic coupling efficiency in sapphire shows a strong anisotropy for electromagnetic waves propagating perpendicular to the c -axis [1, 2]. Therefore we have determined the dependence of the Brillouin scattering efficiency on the polarization angle of the probe-laser beam [see Fig. 5.1]. We use excitation by a 80-MHz, modelocked Ti:sapphire laser that allows for a dynamic range of 10^4 in intensity. Indeed, a very strong variation over three orders of magnitude of the scattered intensity as a function of probe-beam polarization angle ϕ is observed, that can be explained by the sum of the electric-field compo-

nents parallel and perpendicular to the c -axis:

$$I(\phi) = a \left(p_{33}^2 \sin^2 \phi + p_{13}^2 \cos^2 \phi \right), \quad (5.1)$$

where p_{33}, p_{13} denote the elasto-optic coupling parameters for $\vec{E} \parallel c$ and $\vec{E} \perp c$, respectively, and a is an arbitrary scaling factor. The ratio is found to be $p_{33}/p_{13} \approx 22$, which is somewhat larger than expected from the literature values of $p_{33} = 0.23$ and $p_{13} \leq 0.005$ [1]. This difference will be most likely due to the angle of incidence of the probe beam of about 20° , which results in some mixing with the elasto-optic component $p_{31} \approx 0.03$. Without going into further detail on this, we have chosen to maximize the Brillouin scattering intensity throughout Chapters 4 and 5, using the $\vec{E} \parallel c$ polarization.

5.2.2 Strain calibration

Analogous to the method used in Sec. 3.3.2, we can gauge the Brillouin spectrum induced by the coherent strain packet against the thermal phonon background of ~ 40 cts/s, measured in sapphire at 22 GHz and at room temperature. Comparison with the typical intensity induced by the wavepackets, as shown in Fig. 5.1, yields an occupation number $n_\omega \approx 10^3 n_{\text{th}}$ for excitation using a modelocked laser at a fluence of ~ 0.5 mJ/cm² per pulse. Application of Eq. (3.2) results in a component of displacement $\bar{u}_\omega = 3 \times 10^{-14}$ m, or a strain component $\bar{s}_\omega = 3.5 \times 10^{-7}$, over a finesse-limited bandwidth of 0.8 GHz (at a free spectral range of 42 GHz). Calibration of the typical wavepacket spectrum, as shown in Fig. 4.2, to this value yields a coherent strain amplitude of $\sim 1 \times 10^{-4}$ for the ‘modelocked’ wavepackets.

In the case of excitation by amplified laser pulses, we measured a maximum intensity of ~ 1 kcts/s at $E = 8$ mJ/cm² pump fluence. Accounting for the reduction in repetition rate, this yields a $u_\omega = 2.1 \times 10^{12}$ m, corresponding to a coherent strain amplitude of 4×10^{-3} . Comparison with Fig. 4.5(a) shows that this is a slight overestimation by a factor of 2. Most likely, this deviation is caused by the estimate of the duty cycle difference, which depends strongly on the exact dimensions of the detection volume.

5.3 Experiments at different frequency components

In section 4.5 we have introduced a method of describing the patterns in the Brillouin scattering intensity as a function of propagation distance, in terms of spatial

resonances and Bragg-scattering from the moving soliton train [c.f. Eq. (4.1)]. This model assumes a direct relation between the Brillouin frequency ν_B and the observed spatial beating period λ . To check the validity of this approach, we measured the Brillouin intensity at five different frequency components, with mutual distances of 4 GHz.

As usual, individual frequency components of the wavepacket were selected by adjusting the scattering angle within the aperture limited by the windows in the cryostat. Similar to the experiments of Chapter 4, the inelastically scattered beam is frequency filtered by a quintuple-pass Fabry-Pérot interferometer and detected using a gated photon counting setup. The development of the acoustic wavepacket spectrum is monitored by moving the detection volume to difference positions z in the crystal. Figure 5.2(a) shows the dependence of the Brillouin intensity on propagation distance at the selected frequencies, for a pump fluence of 6.5 mJ/cm^{-1} . At all frequencies, the intensity shows a strong decrease in the first hundred micrometers of propagation, followed by an oscillatory behavior. The initial decrease has been attributed earlier to the spectral redistribution of energy, up to terahertz acoustic frequencies, by the nonlinear steepening of the wavepacket (Sec. 4.5) and will not be further discussed at this point. The intricate beating pattern at distances beyond the self-steepening regime can be unravelled by performing a spatial Fourier transform of the experimental traces after the initial decay, where the solitons are supposed to be well-developed. The results of this procedure on the experimental traces are shown in Fig. 5.2(b). In all spectra we observe a distinct amount of spatial frequencies that produce the beating pattern. Unfortunately, the finite propagation distance limits the spectral resolution to $\nu_x \approx 0.17 \text{ mm}^{-1}$, causing the resonances to overlap into broad bands. The scanning length at 26 GHz is further limited to 1 mm by the size of the cryostat windows. Still, several oscillations of $\nu_x \approx 4 \text{ mm}^{-1}$ can be observed.

5.4 Discussion

The degeneracy of many of the resonances makes it an impossible task to assign them individually to beating modes of the soliton train. It is however possible to determine from the spectra a high-wavevector cutoff, corresponding to the interference of light scattered by the fastest soliton with that of the slowest solitons and of the linearly propagating tail. The estimated highest spatial frequencies ν_x for all scattering angles and at several pump intensities are shown in Fig. 5.3. We ob-

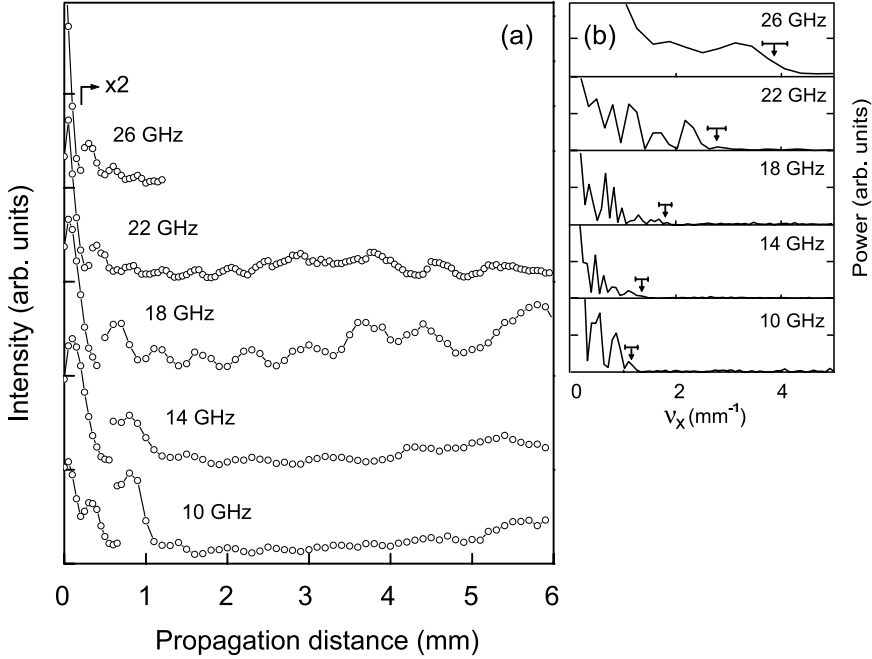


FIGURE 5.2 (a) Brillouin scattering intensity as a function of propagation distance at 5 different scattering angles, at a pump fluence of 6.5 mJ/cm^2 . (b) spatial Fourier transforms of data ($v_x = 1/\lambda$), arrows indicate highest spatial frequency in the scans.

serve a linear dependence of the maximum v_x on the Brillouin frequency, its slope increasing with pump fluence. This is consistent with our earlier interpretation in terms of Bragg-resonances (c.f. Sec. 4.5), which relates the resonance condition $\tau_{\text{res}} = 1/v_B$ to the spatial beating frequency v_x :

$$v_x = \frac{(v_1 - v_2)v_B}{c_0^2}, \quad (5.2)$$

where $v_1 - v_2$ are the velocities of the two scattering objects involved in the resonance, $c_0 = 11.23 \text{ km/s}$ denotes the longitudinal sound velocity in sapphire. We use this relation to obtain accurate values of the velocity difference from the linear fits to the data of Fig. 5.3(b). From analytical solutions to the KdV initial value problem (see Sec. 2.4.2) it is known that the soliton amplitudes in the train are

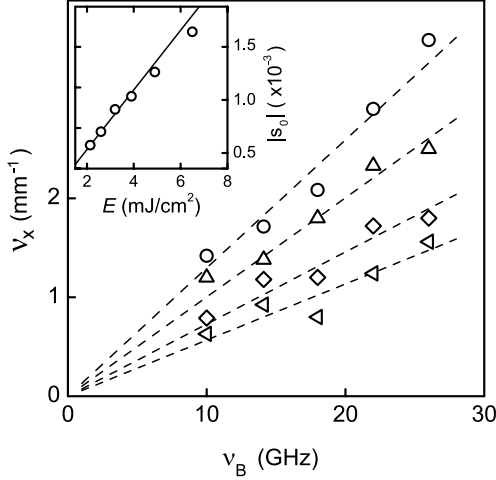


FIGURE 5.3 Highest spatial frequency ν_x as a function of Brillouin frequency ν_B for 4 typical pump fluences $E = 2.6$ (\triangleleft), 3.2 (\diamond), 4.9 (\triangle) and 6.5 (\circ) mJ/cm^2 . Lines are fits to data, following Eq. (5.2). Inset: initial strain amplitude $|s_0|$ obtained from the slope of fitted data at different pump fluences E . Line denotes linear dependence.

given by

$$a_j = \frac{3s_0}{\sigma^2} \left(1 + \sqrt{1 + 2\sigma^2/3} - 2j \right)^2, \quad (5.3)$$

where j is the index of the soliton in the train, $j = 1$ denotes the leading soliton. The parameter σ involves the scaling of the physical problem to the dimensionless class of KdV solutions, and depends on material parameters and initial strain waveform through the expression [c.f. Eq. (2.20)]

$$\sigma = l_0 \left(\frac{\alpha s_0}{2\rho c_0 \beta} \right)^{1/2}, \quad (5.4)$$

with l_0 and s_0 the spatial width and strain amplitude of the initial wavepacket, respectively, α the nonlinear constant defined by the lattice anharmonicity, β the third order correction to the phonon dispersion, and finally ρ the crystal density.

Note that the number of solitons evolving from an initial wavepacket is given by $N = \sigma/\pi\sqrt{6}$, which identifies σ as the generalized pulse 'area' [3]. Under our experimental conditions, σ takes on values in the range 10-50, leading to soliton

trains of up to $N = 11$, and we may approximate Eq. (5.3) for the leading solitons in the train to first order by

$$a_j \approx 2s_0 \left(1 - 4\sqrt{6}j/\sigma\right). \quad (5.5)$$

This shows that for large σ the first soliton in the train has an amplitude $a_1 \approx 2s_0$, independent of the length of the initial disturbance l_0 or material parameters α and β . The velocity change of a soliton, with respect to the sound velocity, is directly related to its amplitude by the relation

$$\frac{\Delta v_j}{c_0} = \frac{\alpha a_j}{6\rho c_0^2}. \quad (5.6)$$

Given the literature value [4] of $\alpha = -1.83$ TPa, we find a relative velocity of $\Delta v_j/c_0 = 0.61|a_j|$ along the c axis of sapphire. Using this relation and Eq. (5.2), we can fit the experimental dependence of the highest wavevector on Brillouin frequency (lines in Fig. 5.3). The values for s_0 obtained from these fits are shown against pump fluence in the inset of Fig. 5.3. Good agreement is found between these values and those obtained from detailed numerical reproduction of the scattered intensity at a single Brillouin frequency in Fig. 4.5.

In the framework of the KdV-model, velocity, amplitude and width of a soliton are connected, resulting in a halfwidth of the strain waveform $s(t) = s_0 \operatorname{sech}^2(t/\tau_j)$ given by:

$$\tau_j = \sqrt{\frac{24\rho\beta}{c_0\alpha a_j}}. \quad (5.7)$$

For the highest strain amplitude in our experiment, $|a_1| = 4 \times 10^{-3}$, this provides a soliton width of $\tau_1 = 0.21$ ps.

5.5 Development of the soliton spectrum

At this point, we will investigate the spectral properties of the soliton trains under study, and in particular the redistribution of energy in the low-frequency part of the spectrum. Further, a connection between the analytical framework and the numerical simulations will be made, in order to find a general behavior in the complicated spectral development of the wavepacket.

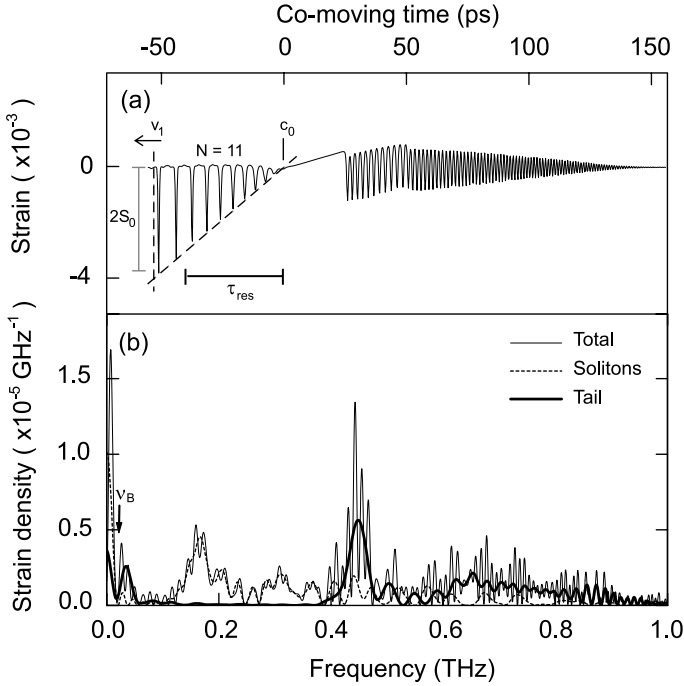


FIGURE 5.4 (a) Simulated soliton train developed after 0.5 mm propagation in sapphire. (b) Acoustic strain spectrum of the simulated soliton packet, with frequency components up to the terahertz range. $\nu_B = 1/\tau_s$ denotes Brillouin frequency of 22 GHz.

Figure 5.4(a) shows again the simulated soliton train of Fig. 4.6, developed from the initial picosecond strain pulse, using the numerical KdV model formulated in the material parameters of sapphire. Clearly, the wavepacket exhibits the typical features predicted by the analytical expressions for large σ , which has a value of approximately 80 in our simulated wavepacket. We observe an equidistant soliton train of $N = 11$, with strain amplitudes decreasing linearly in the train starting from an amplitude of the leading soliton of $a_1 \approx 2s_0$. The trailing radiation in the packet emerges from the dispersive development of the rear edge of the initial bipolar pulse, and is not described in our analytical framework. Figure 5.4(b) shows the acoustic power spectrum of this typical strain waveform, for the complete wavepacket, as well as separated into the individual contributions of soliton train and radiative tail. Spectral components up to terahertz frequencies can be observed, corresponding to the sharpest features of the wavepacket of less

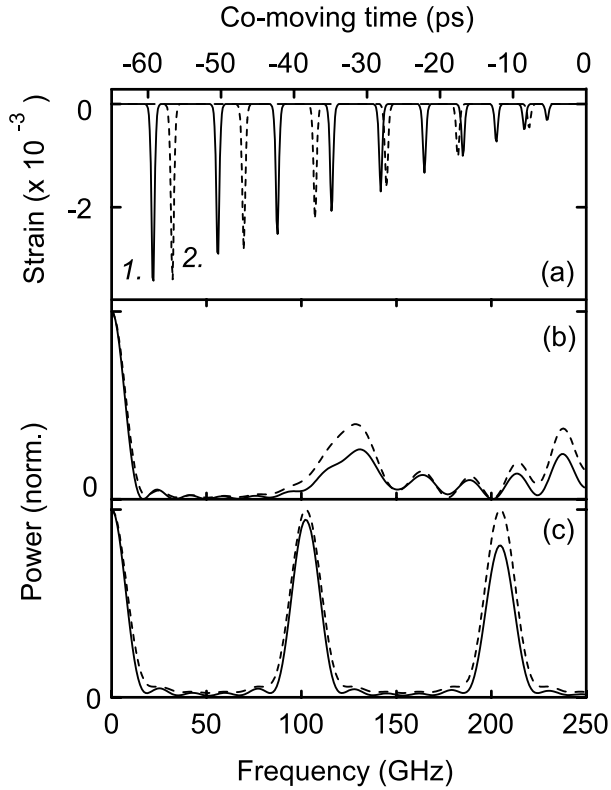


FIGURE 5.5 (a) Analytical soliton trains after 0.5 mm, using 1. real form, Eq. (5.3) (solid) and 2. equidistant approximation, Eq. (5.5) (dash). (b) Power spectrum of the train 1. of (a) (solid), and (dash) using Dirac- δ functions instead of soliton shapes. (c) Similar as (b), for equidistant train 2. of (a).

than ~ 0.5 ps in width. The contributions of the radiative tail are localized primarily in the higher part of this spectrum. The soliton train, however, contains a more homogeneous, but strongly oscillating, distribution of frequency components over the spectral range, which correspond to the spatial resonances of the train.

In the following we will zoom in on the lower-frequency part of the spectrum, and consider only the contribution of the solitons in the packet. Figure 5.5(a) shows two soliton trains as obtained from the expressions Eq. (5.3) (solid) and Eq. (5.5) (dash). Note that the former of the two is exact, while the latter is an approximation for very large σ , that results in an equidistant spacing between

the subsequent solitons. The consequence of this difference in spacing for the lower part of the spectrum can be observed in Fig. 5.5(b,c). For the equidistant soliton train, the spectrum is periodical over a range ~ 100 GHz, while for the exact form no periodicity can be observed. The dashed lines represent the same trains, but with the soliton waveforms replaced by Dirac- δ functions with appropriately scaled amplitudes. Qualitatively, the low-frequency spectrum is not significantly altered by this approximation.

Pursuing the line of thought of our interpretation in terms of Bragg scattering, we can analyze the spectra of Fig. 5.5(b,c) in terms of resonances between the solitons in the train. We consider a train given by

$$f(z, t) = \sum_{j=1}^N a_j \delta(t + \gamma_j z), \quad (5.8)$$

with N the number of solitons, a_j the soliton amplitudes, and $\gamma_j = v_j/c_0^2$ the soliton walkoff in the moving frame system. For the equidistant train of Eq. (5.5), $\gamma_j = j\Delta\gamma$ and $a_j = j\Delta a$, with $\Delta a = 8\sqrt{6}s_0/\sigma$ the amplitude difference and $\Delta\gamma = 4\sqrt{6}\alpha s_0/3\sigma\rho c_0^3$ the walkoff between subsequent solitons [c.f. Eq. (5.6)]. In this case, it is useful to consider the train f of Eq. (5.8) as a product of a comb-function g with a triangular shape h :

$$f(z, t) = g(z, t) \cdot h(z, t) \quad (5.9)$$

$$g(z, t) = \sum_{j=1}^N \delta(t + j\Delta\gamma z), \quad h(z, t) = \frac{\Delta a}{\Delta\gamma z} t.$$

After Fourier transformation, this product will be transformed into the convolution $\tilde{f} = \tilde{g} \otimes \tilde{h}$, with \tilde{g} and \tilde{h} the transforms of the comb and triangular functions, respectively given by

$$\tilde{g}(z, \omega) = (2\pi)^{-1/2} \frac{\sin N\beta\omega}{\sin\beta\omega} e^{-i\beta\omega(N+1)} \quad (5.10)$$

$$\tilde{h}(z, \omega) = -i\zeta \frac{\partial}{\partial\omega} \delta(\omega),$$

with the abbreviations $\beta = \Delta\gamma z/2$ and $\zeta = (2\pi)^{1/2} \Delta a/\Delta\gamma z$. The above expression for \tilde{g} is the well-known transform function for a grating with N slits, indicating

that the frequency spectrum of the equidistant soliton train can be interpreted in terms of the diffraction orders of a grating. For completeness, we give the exact solution of the above convolution equation. Partial integration yields

$$\begin{aligned} \tilde{f}(z, \omega) &= -i\zeta \left. \frac{\partial}{\partial \omega'} \tilde{g}(\omega - \omega') \right|_{\omega'=0} \\ &= \zeta \tilde{g}(\omega) \left(N + 1 + iN \frac{\cos(N\beta\omega)}{\sin(N\beta\omega)} - i \frac{\cos(\beta\omega)}{\sin(\beta\omega)} \right). \end{aligned} \quad (5.11)$$

The power spectrum corresponding to this expression can be observed as the dotted line in Fig. 5.5(c). The overall periodicity in this equation is determined by the zeros of the denominator of \tilde{g} , with spacing $\Delta\omega_0/2\pi = 1/2\beta \approx 102.5$ GHz. Further it turns out that there are exactly $(N - 1)$ subminima between the main orders, with a period $\Delta\omega_1 = \Delta\omega_0/N$, although their visibility is reduced by the additional terms in Eq. (5.11).

We are now able to understand the shape and periodicity of the spectrum in Fig. 5.5(c) by treating the equidistant soliton train as a diffraction grating. It is even possible to determine the number of solitons from the fine structure in the spectrum, by counting the oscillations between the main grating orders. If we now compare the simple form of Fig. 5.5(c) with the spectrum of Fig. 5.5(b), it is clear that the variations in spacing in the real soliton train are sufficient to destroy the periodicity of the grating function. Still, however, the part of the spectrum below, say 100 GHz, seems to correspond reasonably well to the pattern observed in the equidistant soliton train below the first grating order. The bump around 135 GHz may even be attributed to constructive interference of the slightly smaller spacings in the realistic train of Fig. 5.5(a). Thus, by counting the number of oscillations before this maximum, we may get an impression, or lower limit, of the number of solitons in the train. For example, in Fig. 5.5(b) we can count up to 7 minima before the first order maximum at 135 GHz, yielding an estimate of $N = 8$. This means that we underestimate the number of solitons by only two or three.

At a first glance, the spectrum of Fig. 5.5(b) looks very similar to the typical experimental traces for a single Fourier component, as shown in Fig. 5.2(a). This is of course the consequence of the scaling behavior of the spectrum, as the train propagates over distances z [c.f. Eq. (5.10)]. Consequently, when monitoring a fixed frequency component, the initial high-frequency content will meet this probe frequency, as the spectrum scales to lower acoustic frequencies.

5.6 Conclusions

We have determined the evolution of the acoustic spectrum of a picosecond strain wavepacket over millimeters of propagation at five different Brillouin frequencies, and have found the intricate beating patterns typical for soliton train formation. Dependence of the maximum wavevector on Brillouin frequency agrees well with our interpretation in terms of Bragg resonances of the light scattered from parts of the wavepacket propagating with slightly different velocities. Quantitative analysis of this dependence on Brillouin frequency, at several pump fluences, provides us with estimates of the strain amplitude of the first soliton in the train. The value obtained agrees well with our earlier estimates based on numerical simulations. We believe that this interpretation of Brillouin scattering traces in terms of spatial resonances can be used as a reliable method for the determination of the strain amplitudes in an ultrashort soliton train.

Further, via the analysis of a train of equidistant solitons we have described the soliton train spectrum in terms of diffraction orders of a grating. The fine structure between the main grating orders in the spectrum consists of a number of oscillations that is proportional to the number of solitons in the train. This method of analysis of the low-frequency part of the Brillouin traces can be applied reasonably well to the realistic soliton trains in our study, despite the fact that the periodicity is disturbed by the intrinsic deviation in distance between the solitons. Further, the linear stretching of the soliton train with propagated distance ensures that the orders will shift towards lower frequencies, where they can be detected using Brillouin scattering. Thus, examination of the Brillouin traces yields the spectral distribution of the initial soliton train, and its fine structure allows us to determine the number of solitons in the packet.

References

- [1] K. H. Hellwege and A. M. Hellwege, eds., *Landolt-Bornstein* (Springer, 1979), vol. 11, p. 518.
- [2] S. C. Jones, B. A. M. Vaugham, and Y. M. Gupta, *J. Appl. Phys.* **90**, 4990 (2001).
- [3] G. B. Whitham, *Linear and Nonlinear Waves* (Wiley, 1974), 1st ed.
- [4] J. M. Winey, Y. M. Gupta, and D. E. Hare, *J. Appl. Phys.* **90**, 3109 (2001).

CHAPTER 6

COHERENT INTERACTIONS OF TERAHERTZ STRAIN SOLITONS AND ELECTRONIC TWO-LEVEL SYSTEMS IN PHOTOEXCITED RUBY

Abstract

We examine coherent interactions between an ultrashort, longitudinal acoustic soliton train and the 29-cm^{-1} electronic transition in photoexcited ruby. Propagation of the strain pulses over millimeter distance through an excited zone reveals striking behavior of the induced electronic population, that has been explained by impulsive excitation of the two-level systems, combined with the nonlinear properties of the solitons in the resonant medium. This opens up new possibilities for coherent manipulation of ultrashort acoustic pulses by local electronic centers.

6.1 Introduction

Recent efforts to generate coherent, longitudinal strain wavepackets at terahertz frequencies have focused on ultrafast excitation of quantum wells and multilayer structures [1–3]. Thermoelastic generation methods employing a metallic film have been well developed, but remain limited to several hundreds of gigahertz by the optical skin depth and nonequilibrium electron transport [4, 5]. For a long time, investigations of these transducer-generated picosecond strain pulses have been conducted only in the low-amplitude regime and over micrometer propagation distances. However, extension to higher strain amplitudes and larger crystals has opened up an entirely new range of nonlinear phenomena in picosecond ultrasonics. The first observations of strain solitons were made by Hao *et al.* [6] and showed consistency with the Korteweg-de Vries (KdV) equation. Experi-

ments at even larger strain amplitudes, attainable using high-power laser excitation, demonstrated breakup of the initial strain wavepacket into a train of ultra-short solitons in sapphire [see Chapter 4] [7], predicting strain amplitudes up to 0.4% and soliton widths less than 0.5 ps.

In this chapter, we prove directly the presence of 0.87-THz frequency components in these soliton trains by coupling them to the well-known $\bar{E}(^2E) - 2\bar{A}(^2E)$ electronic transition in optically excited ruby. This system, known as the ruby phonon spectrometer, has been used for many years to study nonequilibrium phonons and related transport phenomena [8–11]. The experiments presented in this chapter, however, are of a fundamentally different nature, as the incident strain field excites a macroscopic acoustic polarization in the electronic system, like in gigahertz acoustic paramagnetic resonance [12]. The *half-cycle* nature and very high amplitude of the acoustic field allow for the experimental study of an entirely new regime of coherent electron-phonon interactions.

6.2 Experiments along the a axis

The studied sample is a $10 \times 10 \times 15$ -mm³ ruby crystal with one of the a axes perpendicular to a 10×15 -mm² surface, that is covered by a 1000-Å chromium transducer. High-amplitude, picosecond strain wavepackets are generated thermoelastically by absorption in the transducer of mJ optical pulses from an amplified Ti:sapphire laser, operating at 800 nm. The sample is mounted in an optical cryostat with superconducting magnet, and immersed in superfluid helium held at a temperature of 1.5 K. At similar experimental conditions, we have observed, independently, the development of strain solitons in the ruby crystal, using the Brillouin scattering method of Chapter 4 [7].

The excited-state $\bar{E}(^2E) - 2\bar{A}(^2E)$ doublets in a Cr³⁺-ion form a two-level system (TLS) with an energy splitting equal to 29 cm⁻¹, or 0.87 THz. The metastable density of TLS N^* can be simply controlled by the optical pumping cycle. We use a focused 2-W argon-ion laser to excite a pencil A [c.f. Fig. 6.1(a)] of about 200 μm in diameter up to densities of $N^* \approx 3 \times 10^{18}$ cm⁻³. The R_2 - and R_1 -luminescence intensities, emanating from the $2\bar{A}$ and \bar{E} levels, respectively, allow for a direct monitoring of the ratio of electronic level populations of the TLS. We collect the luminescence perpendicular to the argon-ion laser beam path. The time evolution of the R_2 - and R_1 -emission lines, at 692.8 and 694.2 nm optical wavelengths, is monitored using a double monochromator equipped with a stan-

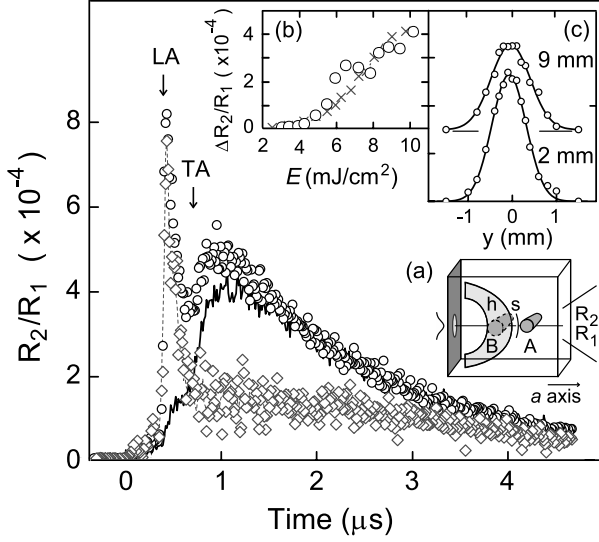


FIGURE 6.1 Time-resolved R_2 luminescence normalized to R_1 at 5-mm propagation distance, for on-axis (\circ) and off-axis (line) configurations, and in the presence of a secondary excited zone B (\diamond), at a pump fluence $E = 8.5 \text{ mJ/cm}^2$. (a) Experimental configuration, with A and B excited volumes, s soliton pulse, and h heat pulse. (b) Soliton-induced LA intensity against pump fluence E at $z = 8 \text{ mm}$ and $N^* \approx 6 \times 10^{17} \text{ cm}^{-3}$, (\circ) Experimental data, (\times) simulation results. (c) Transverse profiles of the soliton-induced LA intensity, at $z = 2 \text{ mm}$ and 9 mm , at $E = 8.5 \text{ mJ/cm}^2$ pump fluence and $N^* \approx 6 \times 10^{17} \text{ cm}^{-3}$.

standard time-resolved photon counting setup with a time resolution of 3 ns. Further, a small magnetic field of $\sim 0.2 \text{ T}$ is applied to lift the degeneracy of the Kramers doublets, enhancing the speed of the ruby detector by a factor of four [11].

6.2.1 Detection in crystal

Figure 6.1 shows a typical R_2 luminescence signal normalized to the R_1 intensity at 5 mm from the transducer, for two configurations: one in which the path of the strain pulses is placed exactly in line with the excited zone (\circ , on-axis), and one at a transverse displacement of 1.5 mm (line/red, off-axis). The off-axis traces are ordinary heat pulse signals [10], with the 1:3-ratio for the longitudinal (LA) and transverse (TA) acoustic phonon contributions and arrival times that are in good agreement with the values calculated for corresponding phonon polarizations (ver-

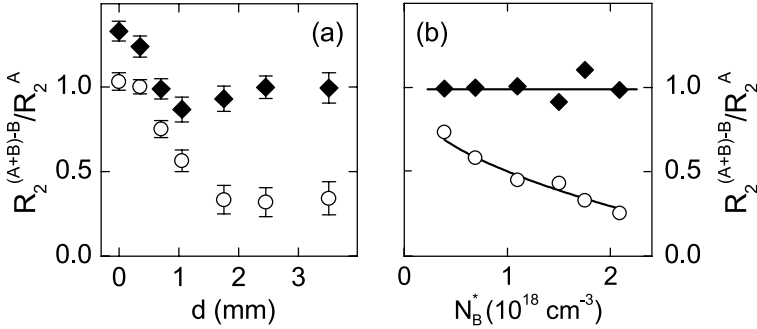


FIGURE 6.2 (a) Soliton-induced LA (\blacklozenge) and heat pulse TA (\circ) relative peak heights against distance d between zones, for $N^* \approx 2 \times 10^{18} \text{ cm}^{-3}$. (b) Similar, but as a function of N^* of zone B , at $d = 2.4 \text{ mm}$.

tical arrows in Fig. 6.1) for propagation along the ruby a axis. The on-axis signal exhibits a sharp spike at a time precisely corresponding to the travel time of the LA phonons from the transducer to the detection volume.

In order to clarify the nature of the on-axis LA peak, we point out three experimental observations. (i) The peak height shows a highly nonlinear dependence on the intensity of the ultrafast pump laser [see Fig. 6.1(b)]: the signal is absent at pump fluences below 4 mJ/cm^2 , but rises quickly above 5 mJ/cm^2 . (ii) The observed width of the transverse profile at 2-mm distance [see Fig. 6.1(c)] coincides with that of the pump laser at the position of the transducer, and only a slight broadening is observed after traversal over 9 mm, corresponding to a divergence angle of less than 0.5° . (iii) The directional component maintains its amplitude throughout the crystal, whereas the heat pulse decays strongly with distance, consistent with a hemispherical radiation source. Together with the independent Brillouin-scattering data, the points (ii) and (iii) confirm that we are dealing with soliton pulses which have frequency components at 0.87 THz. We show later that point (i) is also consistent with the soliton behavior.

6.2.2 Propagation through an additional excited zone

To further explore the difference between the soliton and heat pulse signals, we changed the experimental configuration and included an additional excited zone B [c.f. Fig 6.1(a)], in the path leading from the transducer to the detection zone A . For such a configuration it is well-known that both the ballistic LA and TA

resonant phonons are strongly scattered by the excited Cr^{3+} -ions in zone B [10]. Indeed, we observe a reduction of the heat pulse TA contribution by about 70% of its value without zone B , as shown in Fig. 6.1. In contrast, the soliton-induced LA-contribution remains unchanged, up to the highest $N^* \approx 3 \times 10^{18} \text{ cm}^{-3}$ of zone B . Thus, the solitons are scattered by excited Cr^{3+} much less efficiently than incoherent 29-cm^{-1} phonons in the heat pulse do.

Figures 6.2(a) and (b) show the relative LA- and TA-contributions from zone A , against the distance d and the TLS-density N^* of zone B , respectively. At the highest N^* we obtain a depletion of the thermal TA phonons over a distance d of 1.5 mm. We attribute the relatively large distance required for the depletion of 29-cm^{-1} phonons, by the presence of quasidiffusive phonons, bending around the zone by a single scattering event [13]. These paths can be blocked more efficiently by placing the secondary zone closer to the phonon source. Further the soliton-induced intensity is seen to enhance at distances less than 0.7 mm. This effect can be related to a local increase in N^* due to the spatial overlap of the two zones, leading to a stronger absorption as will be discussed later (c.f. Sec. 7.4.2). The N^* -dependence of the TA-depletion in Fig. 6.2(c) can be explained by the difference in the bandwidth of trapped phonons in the two zones. For an absorption bandwidth scaling with $(N^*)^{1/2}$ (see Sec. 7.4.3 later in this thesis), the presence of excited zone B reduces the luminescence of zone A by $1 - (N_B^*/N_A^*)^{1/2}$ for $N_B^* < N_A^*$ [line in Fig 6.2(c)].

6.2.3 Propagation through a collinear zone

To investigate the scattering of the solitons by excited Cr^{3+} -ions more precisely, we modified the configuration to the one shown in Fig. 6.3(a). The excited zone now consists of a $\sim 0.6\text{-mm}$ wide cylinder *along* the path of propagation of the coherent acoustic beam. Luminescence is again detected at propagation distances z , imaging only a $0.2 \times 0.5\text{-mm}^2$ section of the center of the excited volume [zone A in Fig. 6.3(a)]. We again take the on- and off-axis difference of the luminescence signals to extract the soliton-induced signal. Figure 6.3 shows the amplitude of the soliton-induced signal as the obtained R_2/R_1 -ratios against propagation distance z at three values of N^* . A gradual decrease as a function of propagation distance is observed, that resembles exponential decay (lines). We determine the mean free path for solitons $\bar{l} = 7.0 \pm 1.0 \text{ mm}$ at the highest $N^* = 3 \times 10^{18} \text{ cm}^{-3}$. It is well-known that the mean free path $\bar{l}_r \sim 0.1 \mu\text{m}$ for the resonant 29-cm^{-1} phonons at the same N^* [see Appendix B] [9–11, 14]. This is five orders of magnitude

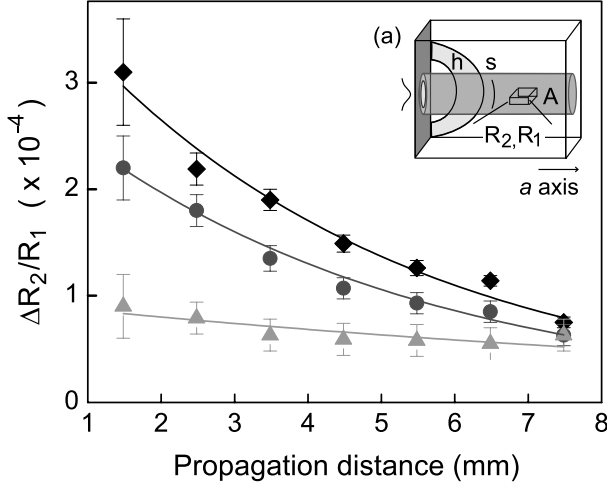


FIGURE 6.3 Soliton-induced LA intensity as a function of propagation distance z for values of $N^* = 0.25$ (▲), 0.8 (●) and 2.5 (◆) $\cdot 10^{18} \text{ cm}^{-3}$. (a) Experimental configuration, including detection volume A .

less than the experimentally observed value for the soliton. Further, from the integral of the population ratios in Fig. 6.3 over the 1-cm long excited pencil, we calculate the energy converted from the wavepacket to the electronic state to be $\sim 1 \mu\text{J}/\text{cm}^2$. This is of the order of magnitude of the *total* energy of the strain wavepacket, implying that significantly more energy is scattered from the solitons into the electronic system than just a near-resonant fraction.

6.3 Coherent, impulsive interaction model

In the following part we will interpret the key experimental features of the soliton-induced luminescence, namely the insensitivity to an additional excited volume, its long mean free path of several millimeters, and the threshold in the pump dependence. Linear response theory predicts the formation of a spectral hole in the propagating wavepacket spectrum at the resonance frequency of the TLS, and would yield the same absorption behavior for the soliton as for the heat pulse, i.e. the formation of a spectral hole at resonance. We will demonstrate below that the intrinsic nonlinearity of the strain solitons can fill in this spectral hole and efficiently funnel energy to the 29-cm^{-1} phonons via spontaneous emission.

The main property, responsible for the experimental observations, turns out to be the slightly higher velocity of the solitons than the velocity of sound, which constitutes the nonlinearity in our problem [6, 7]. We may illustrate this statement using the simulations presented in Fig. 6.4(a,b). The interaction of a short pulse with the TLS results in the formation of trailing resonant strain radiation upon propagation [curve 1 in Fig. 6.4(a)] [15]. The presence of this radiation corresponds to the spectral hole for resonant modes in the combined spectrum of the strain wave after the interaction with TLS. The difference in velocities for soliton and conventional sound leads to a delay of the linear trailing radiation respective to the faster soliton, that is proportional to the propagation distance z . A walk-off by 1/4th of a resonant phonon wavelength will occur within a distance of $l_s \approx 1.3 \mu\text{m}$ for a typical 0.4% strain soliton [7]. This has far-reaching consequences for the development of the trailing radiation as can be seen in Fig. 6.4(a). In a dispersive medium with the resonant Beer's length \bar{l}_r , the trailing radiation virtually disappears [curve 2 in Fig. 6.4(a)], which corresponds to a refilling of the spectral hole at the resonant modes in the frequency domain. Figure 6.4(b) shows the calculated dependence of the population of the resonant 0.87-THz modes in the strain packet which has traversed the resonant medium over a distance z . Curves 1 and 2 [Fig. 6.4(b)] correspond to the linear and nonlinear propagation regimes, respectively. The linear regime is accompanied with a strong attenuation of the resonant modes over $z \sim \bar{l}_r$, while in the nonlinear case the number of resonant modes is almost independent on z . As a result, the nonlinear regime allows to convert almost all energy in the soliton to the resonant electronic two-level system, which emits resonant phonons via spontaneous decay. Obviously, the linear regime cannot produce such a spectral redistribution.

Thus, the temporal and the spectral shape of the soliton wavepacket do not change significantly with propagation distance in the resonant medium. This allows us to simplify the analysis and assume that each atom in the excited volume experiences exclusively impulsive excitation by the solitons. Analogous to treating electronic TLS-excitation in the optical domain, we consider the electronic system as a pendulum, that may be excited either through a resonant driving field or by impulsive action. The latter regime is commonly ignored in optics as it requires pulses shorter than the resonant period of the electronic state. For a quantitative description we make use of the original set of Bloch equations [16], that has been used earlier in the studies of few-cycle optical pulses [17]. In this model, no approximations are made that assume a slowly varying envelope on a fast carrier

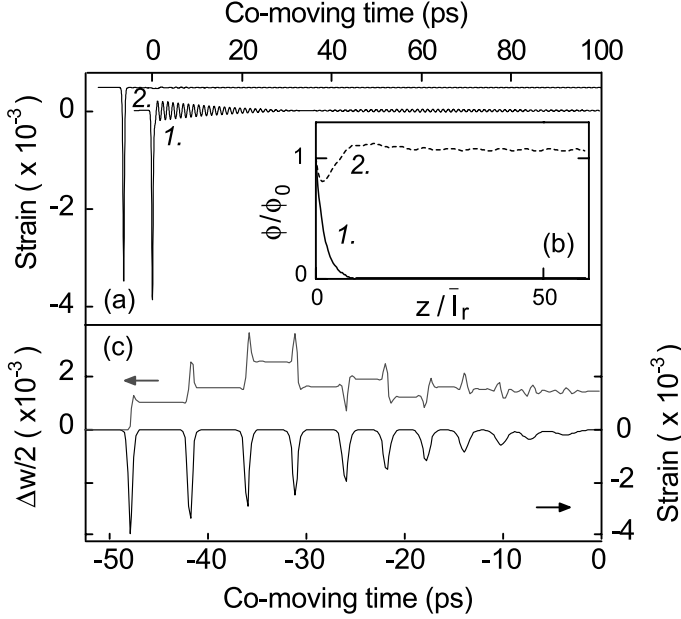


FIGURE 6.4 (a) Time-domain profile of a 0.4% strain pulse after propagation over $150\bar{l}_r$ in a resonant medium, for (1) linear propagation and no walk-off, and (2) with soliton walk-off, $l_s = 13\bar{l}_r$. (b) Resonant Fourier component ϕ at 0.87 THz against traversed distance z/\bar{l}_r for situations (1) (line) and (2) (dash). (c) Simulated population ratio $\Delta w/2$ (line/red) for a typical KdV soliton train [7] (line/black).

wave [12, 16]. Rather, the strain waveform $s(t)$ acts directly on the 'carrier' Rabi frequency $\chi(t)$ proportional to the matrix element χ_0 of the $\bar{E}(^2E) - 2\bar{A}(^2E)$ transition, estimated to a value of $\hbar\chi_0 \approx 200 \text{ cm}^{-1}$ per unit of uniaxial strain along the ruby a axis [18, 19]. Subsequently the phase of the electronic state vector rotates with resonance frequency ω_0 and decays by spontaneous emission, $T_1 \approx 0.7 \text{ ns}$ [14], and $T_2 = 2T_1$. For completeness, we give the full evolution equation for the electronic state vector \vec{S} :

$$\frac{\partial}{\partial t} \vec{S} = \vec{\beta} \times \vec{S} - \Gamma \cdot (\vec{S} - \vec{S}_0), \quad (6.1)$$

with the usual conventions for relaxation Γ , initial state $\vec{S}_0 = (0, 0, -1)$, and pseudofield-vector $\vec{\beta} = (2\chi(t), 0, \omega_0)$.

Knowing the state vector \vec{S} , we can calculate the population ratio $\Delta w/2$ of the

electronic levels by projection of \vec{S} onto the vertical axis. Numerical simulations of $\Delta w/2$, during the passage of a realistic soliton train (see Ref. [7]), are shown in Fig 6.4(c). It is observed that excitation of the two-level system is induced primarily by the first 5 pulses in the train consisting of 11 solitons. In contrast to the sharp steps produced by these first solitons, that are the shortest and have the highest amplitude, excitation by the longer pulses at the end is suppressed by the precession of the state vector at its natural frequency ω_0 . We also observe that in our example, for the 4th and 6th solitons, we have a *decrease* in the population. This is similar to coherent control experiments, where the result of the short pulse excitation depends critically on the phase of the electronic state [20]. The obtained excitation $\Delta w/2 \approx 2 \times 10^{-3}$ corresponds to a Bloch angle of about 4° , which means that the electronic excitation remains well within the linear regime of the harmonic oscillator.

The measured ratio of R_2 - and R_1 -luminescence intensities is of the order of magnitude of the calculated $\Delta w/2$ for the typical soliton train in Fig. 6.4(c). For more precise quantitative agreement between simulated and experimental R_2/R_1 -ratios in Fig. 6.1(b), we correct for the bottleneck efficiency [9–11] and radiative probabilities of the R -lines [21]. We have simulated the excited-state population for impulsive excitation by soliton trains at various initial strain amplitudes and plotted the results as R_2/R_1 in Fig. 6.1(b) (\times). Here the horizontal scale was calibrated using the Brillouin scattering data mentioned in Sec. 6.1. We obtain good agreement in both the offset at $\sim 4 \text{ mJ/cm}^2$ and the steep increase of the signal for increasing pump fluences, above the threshold of Fig. 6.1(b).

Our estimate of $\Delta w/2$ of 2×10^{-3} adds up to an accumulated electronic energy of $\sim 1 \text{ } \mu\text{J/cm}^3$ at $N^* = 10^{18} \text{ cm}^{-3}$, and thus to a soliton mean free path of $\sim 1 \text{ cm}$, in close agreement with the experiments of Fig. 6.3.

Experimental results are consistent with the presented model where the slight difference in velocities for soliton and the linear sound takes place, enough to fill in the spectral hole around the resonance. The mean free path for the soliton pulses is in this model much larger than that for resonant phonons from the heat pulse. Further, the accumulated energy transferred from the soliton to the TLS-medium at the mean-free path is of the order of the total energy in the initial strain packet.

6.4 Conclusions

In conclusion, we have observed coherent interaction between an acoustic soliton train and the $\bar{E}(^2E) - 2\bar{A}(^2E)$ electronic transition in photoexcited ruby, explicitly demonstrating the development of strain components in the solitons of frequencies as high as 0.87 THz. The soliton-induced signal was found to be highly directional, strongly dependent on pump fluence, and only weakly influenced by dissipation through the interaction with the electronic system. We have explained the key experimental observations using only simple arguments based on nonlinear refilling of the spectral hole and impulsive excitation of the two-level systems by the soliton train.

The presented work opens up new avenues for the manipulation of ultrashort acoustic pulses using local electronic centers. A challenging possibility is the amplification of coherent terahertz-strain wavepackets using inverted two-level systems, attainable by direct optical excitation of the $2\bar{A}(^2E)$ states. The transducer-generated ultrashort strain solitons may then serve as a trigger for starting up the coherent release of the acoustic polarization in the form of a resonant tail. In this situation, the area theorem [15, 16] predicts exponential growth of the Bloch angle of this tail over the submicrometer, *resonant* absorption length \bar{l}_r , anticipating an exponential factor $L_c/\bar{l}_r \approx 200$, with $L_c = c_0T_1$ the length over which the inversion can be maintained using pulsed optical excitation of the Cr^{3+} -ions [22]. Amplification over several orders of magnitude and concomitant breakup of the wavepacket into a new kind of terahertz strain solitons, the resonant 2π -pulses of self-induced transparency, appears well within the range of experimental possibilities.

References

- [1] A. Bartels, T. Dekorsy, H. Kurz, and K. Köhler, Phys. Rev. Lett. **82**, 1044 (1999).
- [2] Ü. Özgür, C.-W. Lee, and H. O. Everitt, Phys. Rev. Lett. **86**, 5604 (2001).
- [3] A. Kent, N. M. Stanton, L. Challis, and M. Henini, Appl. Phys. Lett. **81**, 3497 (2002).
- [4] C. Thomsen, H. T. Grahn, H. J. Maris, and J. Tauc, Phys. Rev. B **34**, 4129 (1986).
- [5] O. B. Wright and K. Kawashima, Phys. Rev. Lett. **69**, 1668 (1992).
- [6] H.-Y. Hao and H. J. Maris, Phys. Rev. B **64**, 064302 (2001).
- [7] O. L. Muskens and J. I. Dijkhuis, Phys. Rev. Lett. **89**, 285504 (2002).
- [8] K. F. Renk and J. Deisenhofer, Phys. Rev. Lett. **26**, 764 (1971).

-
- [9] J. E. Rives and R. S. Meltzer, *Phys. Rev. B* **16**, 1808 (1977).
- [10] A. A. Kaplyanskii and S. A. Basun, in *Nonequilibrium Phonons in Nonmetallic Crystals*, ed. W. Eisenmenger and A. A. Kaplyanskii (North Holland, 1986) p. 373.
- [11] R. J. G. Goossens, J. I. Dijkhuis, and H. W. de Wijn, *Phys. Rev. B* **32**, 7065 (1985).
- [12] N. S. Shiren, *Phys. Rev. B* **2**, 2471 (1970).
- [13] W. E. Bron and W. Grill, *Phys. Rev. Lett.* **40**, 1459 (1978).
- [14] M. H. F. Overwijk, P. J. Rump, J. I. Dijkhuis, and H. W. de Wijn, *Phys. Rev. B* **44**, 4157 (1991).
- [15] D. C. Burnham and R. Y. Chiao, *Phys. Rev.* **188**, 667 (1969).
- [16] L. Allen and J. H. Eberly, *Optical Resonance and Two-Level Atoms* (General Publishing Company, 1987), 2nd ed.
- [17] R. W. Ziolkowski, J. M. Arnold, and D. M. Gogny, *Phys. Rev. A* **52**, 3082 (1995).
- [18] M. Blume, R. Orbach, A. Kiel, and S. Geschwind, *Phys. Rev.* **139**, A314 (1965).
- [19] S. M. Sharma and Y. M. Gupta, *Phys. Rev. B* **43**, 879 (1991).
- [20] N. Dudovic, D. Oron, and Y. Silberberg, *Phys. Rev. Lett.* **88**, 123004 (2002).
- [21] S. Sugano and Y. Tanabe, *J. Phys. Soc. Jpn.* **13**, 880 (1958).
- [22] M. H. F. Overwijk, J. I. Dijkhuis, and H. W. de Wijn, *Phys. Rev. Lett.* **65**, 2015 (1990).

CHAPTER 7

STRAIN SOLITONS AND THE 29-cm^{-1} RUBY PHONON SPECTROMETER

Abstract

The interaction between strain solitons and the 29-cm^{-1} phonon spectrometer is examined for propagation of the acoustic wavepackets along both the ruby a - and c -axes. We observe a large difference in soliton-induced R_2 luminescence between the two configurations, that can be explained by the anisotropy of the crystal-field coupling strength between the longitudinal acoustic phonons and the electronic two-level systems. The detector response as a function of a variety of external parameters is studied and explained in the context of the impulsive excitation model of Chapter 6.

7.1 Introduction

Recent experiments have demonstrated the development of ultrashort strain solitons from a picosecond acoustic wavepacket during ballistic propagation in large crystals at low temperatures [1, 2]. It was found that these *half*-cycle pulses can reach strain amplitudes as high as 0.4% and frequency components into the terahertz-range. This combination of high strains on ultrashort time scales holds promise for exploring terahertz-coherent electron-phonon interactions in a medium containing two-level centers [3]. Early experiments have explored the phenomenon of acoustic self-induced transparency of gigahertz ultrasonic pulses [4], demonstrating the direct analogy between acoustic paramagnetic resonance experiments and coherent optics in two-level media [5]. For terahertz electron-phonon interactions, however, coherence has up to now not played a significant role, mainly due to the lack of suitable excitation mechanisms for the strain field. Stimulated emission [6] has been well described by incoherent rate equations, and

it was only in phonon-induced optical dephasing experiments [7] that the question of phonon coherence was addressed.

In this chapter we again employ the ruby phonon spectrometer, based on the $\bar{E}(^2E) - 2\bar{A}(^2E)$ crystal field transition of the Cr³⁺ embedded in the Al₂O₃ host lattice. By exposing this system to trains of ultrashort acoustic solitons, we have demonstrated in Chapter 6 coherent, impulsive interactions along the crystallographic *a* axis. Here, we extend the studies to propagation in the other high-symmetry direction, the *c* axis. The behavior of the soliton-induced *R*₂ luminescence for strain propagation along the two principle axes is compared as a function of the applied magnetic field, the concentration of excited ions, and the power of the femtosecond pump laser. The additional experimental data is used to test the interpretation of Chapter 6, in terms of nonlinear refilling of the spectral hole in the $\bar{E}(^2E) - 2\bar{A}(^2E)$ absorption band. As an introduction to the experiments, the theory of linear and nonlinear propagation in a resonant medium is reconsidered in the next section.

7.2 Theory of spectral-hole refilling

For the explanation of the soliton-induced *R*₂ luminescence in Chapter 6, we proposed a model based on nonlinear reshaping of the solitons in the resonant medium and concomitant refilling of the spectral hole at 0.87-THz. In this section we will go into more detail on this model and demonstrate that the energy removed from the soliton wavepacket by spontaneous emission is *linearly* proportional to the propagated distance *z* and thus to the amount of centers *N*^{*}, while the energy taken from a linear wavepacket by the electronic system is only proportional to *z*^{1/2} and (*N*^{*})^{1/2}. In simple words, this amounts to the fact that after propagation over a few Beer's lengths, for a nonlinear soliton, absorption continuously takes place in the *center* of the resonance due to the refilling of the spectral hole, while for linear pulses only the wings of the resonance contribute to the absorption.

For the explanation of resonant absorption of phonons in an opaque medium we resort to the most simple picture, namely that of Beer's law for a homogeneous resonance. After travelling over several resonant absorption lengths \bar{l}_r , the phonon spectrum at the center of the resonance is completely absorbed. We can estimate the spectral absorption bandwidth Δ from solving Beer's law for a homogeneous, Lorentzian line shape

$$\frac{I_{\Delta}(z)}{I_{\Delta}(0)} = e^{-z/\bar{l}(\Delta)} = \frac{1}{2}, \quad \bar{l}(\Delta) = \bar{l}_r \frac{\Delta^2 + T_2^{-2}}{T_2^{-2}}. \quad (7.1)$$

For large propagation distances, i.e. $z \gg l_r$, we can expand the exponential to first order, resulting in a bandwidth Δ of the spectral hole

$$\Delta \approx \left(2T_2^{-2}z/l_r\right)^{1/2}, \quad (7.2)$$

which for $l_r \propto 1/N^*$ increases with $(N^*)^{1/2}$. The amount of energy that is absorbed out of the phonon spectrum after several resonant mean free paths is given by the phonon density of states $\rho(E)$, integrated over the absorption bandwidth Δ , times the resonant phonon energy $\hbar\omega$.

We now consider the evolution of a very short, *linear* strain pulse travelling through a two-level medium. As calculated in Chapter 6, the impact of a *half*-cycle pulse, short compared to the angular frequency of the electronic two-level systems, impulsively tilts the electronic state vector to a Bloch angle θ . The ensemble of excited atoms in the medium subsequently radiates back to the strain field, partly coherent, via superradiance, and partly incoherent, via spontaneous emission. The evolution of short pulses propagating in a two-level medium has been thoroughly analyzed in terms of these two processes for optical radiation [8–10]. The direct analogy between the optical- and acoustic-field equations (see Appendix B) allows us to apply these concepts to the electron-phonon system under study. In fact, the results of Refs. [8–10] reduce again to the linear (dielectric) response theory in the limit of low excitation [5]. Therefore, the wavepacket evolution may be completely described in the spectral domain using the spectral response functions of the medium. For a Lorentzian resonance lineshape, the evolution operator $\tilde{F}(\omega, z)$ has the simple spectral form [5, 11]

$$\begin{aligned} \tilde{F}(\omega, z_j) &= \exp(i\tilde{\phi}(\omega)z_j) \\ \tilde{\phi}(\omega) &\approx \frac{T_2^{-1}}{2} \left(\frac{1}{(\omega - \omega_0) - iT_2^{-1}} + \frac{1}{(\omega + \omega_0) - iT_2^{-1}} \right), \end{aligned} \quad (7.3)$$

where $\tilde{\phi}(\omega)$ is defined so that its imaginary part equals unity at resonance and Eq. (7.3) reduces to Eq. (7.1) for the intensity (Beer's law), with the propagated distance expressed in units of resonant absorption lengths, $z_j = z/\bar{l}_r$. In the derivation of $\tilde{\phi}(\omega)$ we have used the approximation $(1 + \epsilon)^{1/2} \approx 1 + \frac{1}{2}\epsilon$, where $\epsilon \ll 1$

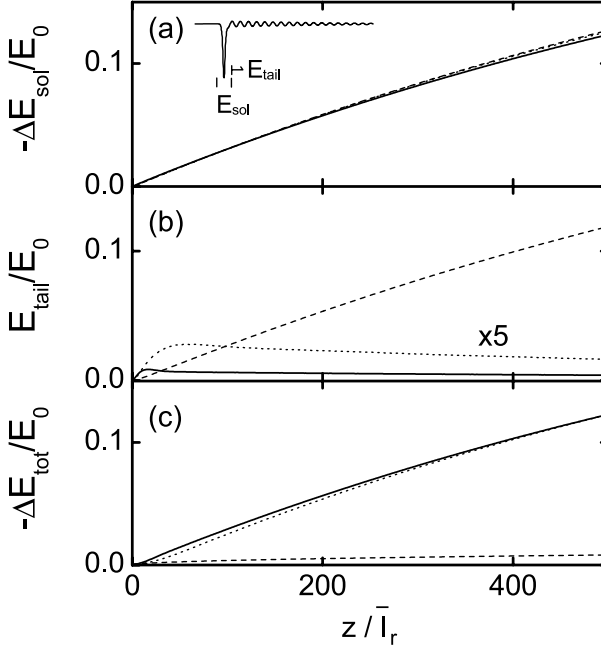


FIGURE 7.1 Dependence on propagated distance z in units of \bar{l}_r of (a) energy removed from soliton $-\Delta E_{\text{sol}}$, (b) energy contained in trailing radiation E_{tail} , and (c) energy removed from total wavepacket by spontaneous emission, $-\Delta E_{\text{tot}}$, normalized to initial energy E_0 , for nonlinear soliton pulse with walk-off length $l_s = 6\bar{l}_r$ (line), $l_s = 13\bar{l}_r$ (short dash), and linear strain pulse (dash).

denotes the (dielectric) susceptibility function.

In an acoustically thin medium, i.e. $z \ll \bar{l}_r$, the net absorption is not limited by the available 29-cm⁻¹ phonons, and one can approximate the exponential decay function in Eq. (7.1) by a linear term $[1 - z/\bar{l}(\Delta)]$. Under these conditions, the energy removed from the total phonon wavepacket by the two-level medium via spontaneous emission is proportional to the number of scatterers N^* . In contrast, for an opaque medium, i.e. $z \gg \bar{l}_r$, the absorption at resonance strongly saturates by the depletion of the 29-cm⁻¹-phonons in the packet. Spontaneous emission then only takes place in the wings of the resonance, over a bandwidth given by Eq. (7.2). Thus, in this situation, the energy taken from the wavepacket by spontaneous emission is proportional to the square root of the number of TLS, i.e. $\propto (N^*)^{1/2}$.

The above argument shows that the energy drained from the linear strain pulse is proportional to N^* while the fraction that is eventually removed by spontaneous emission is only proportional to $(N^*)^{1/2}$. The difference between the two must therefore be the energy remaining in the electronic polarization and carried by the coherently emitted radiative tail.

This redistribution of energy within the wavepacket is illustrated by the calculations presented in Fig. 7.1(a-c). Using the response function of Eq. (7.3), we have simulated the propagation of a short pulse through the TLS-medium over a distance of $z_j = 500$, corresponding to the typical length scale of our experiments. In our calculations we consider both the *linear* (dashed line) and the *nonlinear* (solid line and dotted line) propagation regimes by adjusting the soliton velocity in the moving frame system. Subsequently, energy densities are defined locally within the total strain wavepacket by integration of the square of the strain field over the part of the wavepacket that can be assigned to the soliton pulse and the part corresponding to the trailing radiation packet [see inset Fig. 7.1(a)]. In this way the energy flow from the soliton, $-\Delta E_{\text{sol}}$, and to the tail, ΔE_{tail} , may be computed and compared with the energy contained in the strain field before entering the TLS medium.

In Fig. 7.1(a) we plot $-\Delta E_{\text{sol}}/E_0$, the energy that is removed from the soliton pulse normalized to the initial pulse energy E_0 , against propagated distance in the resonant medium. We observe for both the linear pulse and nonlinear solitons a continuous drain of energy from the soliton proportional to the travelled distance z , due to impulsive excitation of the electronic system. Up to 12% of the initial energy is removed from the pulse over a distance of 500 resonant absorption lengths \bar{l}_r , which corresponds to about one millimeter of excited ruby at $N^* = 10^{18} \text{ cm}^{-3}$. The very small difference between the full and the dashed lines at large z_j is due to grid-size limitations of our calculation and has no physical significance.

The fundamental difference between linear and nonlinear propagation in the two-level medium is illustrated in Fig. 7.1(b,c). In Fig. 7.1(b) we plot the energy accumulating in the form of coherent trailing radiation, $\Delta E_{\text{tail}}/E_0$. Clearly, in the *linear* case (dashed line), the energy taken from the soliton pulse is almost completely given back to the coherent strain field in the form of trailing radiation. In the time domain [c.f. Fig. 6.4(a)] this corresponds to the development of a tail on a length scale corresponding to the superradiant decay length $T_R \ll T_2$ [10]. In the spectral domain, this corresponds to the formation of a spectral hole. In contrast, for the *nonlinear* soliton pulse (solid line and dotted line), the amount of energy

carried by the trailing radiation tail remains on a very low, stationary level, that is already established within a distance l_s . Comparison with the trace of Fig. 6.4(a) tells us that this suppression of the radiative tail for nonlinear pulses corresponds to the *destructive* interference of the superradiant emission, as the soliton pulse moves away from the linear radiative tail over a distance larger than one period of the resonant 0.87-THz phonons. The stationary state of energy exchange for the nonlinear propagation regime depends on the magnitude of l_s with respect to \bar{l}_r , but this has no influence on the measured luminescence intensity, as we will demonstrate below.

The fraction of the total energy, $\Delta E_{\text{tot}}/E_0$, that is lost from the wavepacket by spontaneous emission of the TLS, is shown in Fig. 7.1(c). Here we find the reverse behavior of that in Fig. 7.1(b), namely that the energy taken from the *non-linear* soliton pulse is completely removed from the coherent packet via spontaneous emission, while only a minor part of the energy of the *linear* pulse has been transferred to spontaneously emitted phonons. This part is proportional to $(N^*)^{1/2}$ as expected from Beer's law, Eq. (7.2). In the spectral domain this difference amounts to the refilling of the resonant spectral hole in the nonlinear situation, as was shown in Fig. 6.4(b).

Furthermore, the calculated amount of energy brought to the bottleneck by spontaneous emission is in the nonlinear case virtually the same for the two specified values of the walk-off distance l_s . Of course this is closely related to the formation of a stationary state of the tail, that is established after one walk-off distance. Energy balance then simply *requires* that the constant drain of energy from the soliton is transferred to spontaneous emission, irrespective of the magnitude of l_s . However, when the refill-rate becomes smaller with increasing l_s , the steady-state population of resonant phonons drops to a very low level and the situation of the linear pulse is gradually approached. This transition regime, however, lies far beyond the window of feasible experimental values for l_s .

Hence, from the simulation results of Fig. 7.1(a-c) a comprehensive picture emerges of the interaction between strain packets and electronic centers for both the linear pulses and the nonlinear solitons. The key observation is that the amount of energy converted to 29-cm⁻¹ phonons via spontaneous emission is *linearly* proportional to the number of centers N^* . The fact that the superradiant radiation tail is suppressed by the difference in velocity of the solitons and linear sound is consistent with the picture presented in Chapter 6, in which a refilling of the hole takes place by the nonlinear reshaping of the soliton.

7.3 Experiments along the c axis

7.3.1 Method

In this section we present experiments conducted in the configuration in which the strain packets propagate along the c axis of a ruby crystal containing 500 ppm. Cr^{3+} -ions. For this purpose, the $10 \times 10 \times 15\text{-mm}^3$ specimen of Chapter 6 was covered with a 100-nm chromium transducer on one of the other $10 \times 15\text{-mm}^2$ surfaces, oriented perpendicular to the crystallographic c axis. Again, as in Chapter 6, the metastable $\bar{E}(^2E)$ -level is populated by indirect excitation via the broad 4T_2 and 4T_1 absorption bands, using a multimode 2-W argon-ion laser beam focused to a pencil of about $200 \mu\text{m}$ in diameter. Following excitation of high-amplitude strain pulses via absorption in the metal film of optical femtosecond pulses from an amplified Ti:sapphire laser, the time evolution of the R_1 - and R_2 -emission lines in the crystal is monitored using a double monochromator equipped with a time-resolved photon counting setup. Direct feeding of the $2\bar{A}(^2E)$ -level via the optical pumping cycle is switched off during the acquisition of the soliton signal by means of an acousto-optic modulator. An external magnetic field is applied parallel to the c axis to lift the degeneracy of the electronic doublets, $\bar{E}(^2E)$ and $2\bar{A}(^2E)$, and decrease the bottleneck decay time (see Sec. 7.4.1 for details). The experiments on the propagation of strain packets along the ruby a axis in Chapter 6 demonstrated strong interaction between strain solitons and the electronic system throughout the entire crystal. However, for propagation along the c axis, no soliton-induced R_2 luminescence could be detected inside the crystal.

In heat-pulse experiments, suppression of the LA phonon-induced R_2 luminescence along the crystallographic c axis has been observed and explained earlier in a set of sophisticated experiments by Kaplyanskii *et al.* [12]. By applying the selection rules for the $\bar{E}(^2E) - 2\bar{A}(^2E)$ transition in the trigonal point group, they demonstrated complete disappearance of the electron-phonon coupling parameter for propagation along the c axis of a collimated heat-pulse beam. This issue is addressed in Appendix B.

7.3.2 Detection at endface

Strikingly, a soliton-induced contribution could be detected at the far end of the crystal. Figure 7.2 shows two typical time-resolved luminescence traces, at a

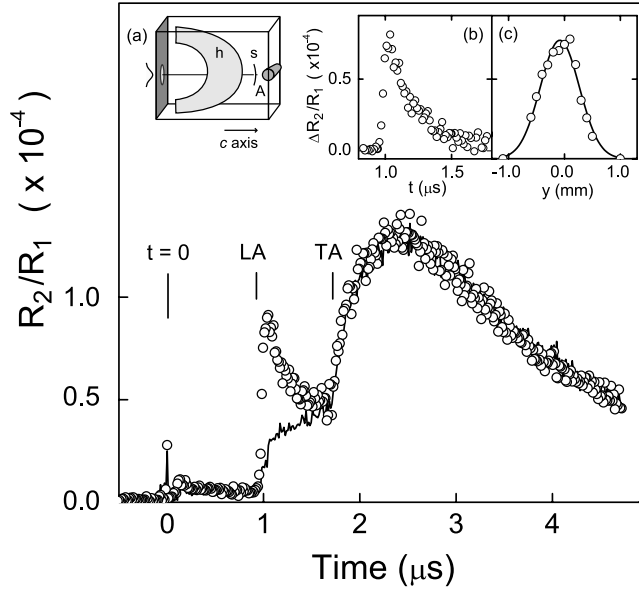


FIGURE 7.2 Time-resolved R_2 luminescence normalized to R_1 at 9.6-mm propagation distance along the c axis, for on-axis (\circ) and off-axis (line) configurations. (a) Experimental configuration, with A detection region, s soliton pulse and h heat pulse. (b) Difference signal between on- and off-axis. (c) Transverse profile of the soliton-induced LA intensity at $z = 9.6$ mm.

magnetic field of ~ 0.1 T, for the configurations in which the excited zone A [c.f. Fig. 7.2(a)] is positioned in the path of the acoustic wavepacket (on-axis) or at a transverse displacement of 1 mm (off-axis). The peak at zero time and the luminescence background during the first microsecond are due to spurious effects induced by pump light leaking through the metal film. A clear difference between on- and off-axis signals is observed at a time corresponding to the arrival of LA-phonons from the transducer. Fig 7.2(b) shows the difference of the two traces around the LA arrival time. After a rapid rise of the population within 10 ns, $\Delta R_2/R_1$ decays exponentially over $0.25 \mu\text{s}$, governed by the so-called bottleneck of 29-cm^{-1} phonons [12, 13]. The amplitude of the R_2 luminescence normalized to the R_1 intensity is 0.7×10^{-4} , an order of magnitude smaller than the ratio measured along the a axis under the same pumping conditions. The transverse profile of the additional contribution in the LA-luminescence, shown in Fig. 7.2(c), has a Gaussian profile with a $1/e$ -halfwidth of 0.4 mm. This corresponds favorably

to the width of the pump laser beam at the position of the transducer, indicating a divergence angle of less than one degree. The highly nonlinear dependence of this signal on pump fluence (see Sec. 7.4.2) and the directionality of the beam signifies that the additional luminescence is induced by the strain solitons.

The soliton-induced R_2 luminescence is the strongest when the excited zone is positioned just inside the crystal, but close to and partially overlapping with the edge of the crystal [c.f. Fig 7.2(a)]. We measured the decay of this signal by scanning the beam into the bulk of the crystal as well as beyond the crystal. The results, presented in Fig. 7.3(a), show a strong decay of the luminescence into the crystal within 0.2 mm, followed by a slow attenuation persisting to distances up to ~ 1 mm from the surface. In the other direction, the intensity decreases much more rapidly due to the reduced overlap between the probe laser beam and the crystal. Three typical time-resolved traces at increasing distance from the crystal surface [denoted by points 1, 2, and 3 in Fig. 7.3(a)] are shown in the central part of Fig. 7.3. Although the quality of this data is not very good, we can still observe some features related to the longitudinal phonons. The onset of the LA-phonon induced luminescence is very sharp for the trace taken at the surface (curve 1). Compared to this slope, the onset of the LA peak in curves 2 and 3 is much less pronounced. At a distance of 1 mm from the surface (curve 3), we can even distinguish two separate steps in the increase of the LA signal, both at 0.9 and 1.1 μs , that correspond well to the arrival time of phonons directly from the transducer and after reflection at the crystal surface, respectively.

7.3.3 Discussion

In order to explain the appearance of soliton-induced luminescence exclusively near the surface we consider the well-known theories of mode-conversion of phonons reflecting at a rough interface. A considerable amount of research has been done on the related problem of enhanced transmission of high-frequency phonons through an interface, known as Kapitza resistance (see e.g. Ref. [14]). Following the work of Nakayama [15], we consider the processes of mode conversion and diffusive scattering of acoustic phonons at the ruby surface. Apart from direct surface scattering of the LA phonons into bulk modes (LA and TA), there are several channels of indirect scattering involving surface modes (R). The lifetimes of these R-modes for the reverse scattering processes into bulk waves was estimated to be of order $\tau_R = 100\nu^{-5}$, with ν the phonon frequency in gigahertz [15]. For the 0.87-THz phonons in our experiment, this corresponds to a lifetime of 0.2 ps,

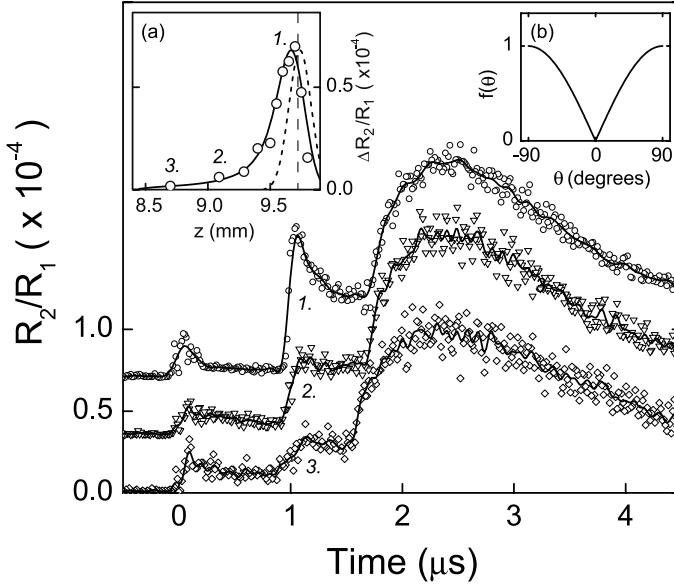


FIGURE 7.3 Time-dependent traces of the R_2 luminescence normalized to R_1 at indicated positions in the crystal, (\circ), (∇), and (\diamond) experimental points, (line) 5-point signal average. (a) Soliton-induced R_2/R_1 -ratio as a function of position z in the crystal, (\circ) experimental data, vertical dashed line at $z = 9.7$ mm denotes exact surface position; model calculations for localized surface excitation (short dash) and diffusive scattering (line). (b) Dependence of the normalized electron-phonon coupling parameter $f(\theta)$ on angle θ of the reflected phonons.

which is less than one oscillation period. Clearly the presence of these indirect channels will not be observable via surface modes. However, they will serve to enhance the diffusive nature of the scattered high-frequency phonons.

For our further analysis, we just consider the endface, apart from the specular reflection, as a Lambertian surface, diffusively reflecting the phonons back into the crystal. This yields a hemispherical distribution function of phonons scattered from a single point at the surface of $n_\omega(r, \theta) \propto 1/r^2$. In the most simple approximation, the highly anisotropic coupling strength between strain and the electronic transitions can be approximated by the projection of the phonon wavevector onto the a axis normalized to its absolute value, $\eta(\theta) = |\sin \theta|$, with θ the angle between wavevector and the c axis. The luminescence per volume element d^3r can now be written as

$$\frac{R_2}{R_1} d^3r = \Gamma n(r, \theta) \eta(\theta) r^2 \sin \theta dr d\theta d\phi, \quad (7.4)$$

where Γ denotes an overall bottlenecking efficiency factor. For a cylindrical detection volume parallel to the surface, we may integrate this response function over the cartesian dimension x . After convolution with the 200- μm wide Gaussian (y, z) profile of the probe volume, we arrive at the luminescence intensity. Excellent agreement is obtained with our experimental data using this model [line in Fig. 7.3(a)]. In contrast, we also show in Fig. 7.3(a) (dashed line) the behavior as expected from an excitation mechanism that is localized at the surface. As expected, the resulting trace is just equal to the profile of the probe volume centered at the surface, which is much too narrow to explain the experimentally observed decay into the crystal.

If we wish to account for the observed luminescence intensity we must realize that the mechanism responsible for the luminescence after diffuse scattering at the crystal surface cannot be the same as the nonlinear refilling of the spectral hole introduced in Chapter 6. The diffusive surface-scattering efficiently distorts the wavepacket coherence on the nanometer scale and the remaining specularly reflected part will be inverted at the free surface and therefore be pulled apart by dispersion. These disturbances result in a severe suppression of the nonlinearity in the wavepacket propagation directly after reflection, ‘freezing in’ the acoustic spectrum as it was present prior to the scattering at the surface. Thus the interaction with the electronic states after diffuse scattering of the wavepacket should be considered like that of an incoherent phonon spectrum and should behave accordingly, i.e. like a heat pulse. A more detailed analysis of these notions and the resulting dependencies will be presented in the next section.

7.4 Properties of the soliton-TLS interaction

Up to this point, we have discussed two experiments in which the strain packets were travelling along either one of the crystallographic a (c.f. Chapter 6) or c (c.f. Sec. 7.3.2) axes. We identified soliton-induced interactions and demonstrated effects of mode conversion at the crystal surface. In Sec. 7.3.2, it was already mentioned that there should be a marked difference of the soliton-induced luminescence between the two configurations, as for direct detection the solitons behave essentially nonlinear, while after reflection and mode-conversion the wavepacket spectrum and propagation may become completely linearized. In or-

der to make the case more strongly and draw definitive conclusions, it is very important to examine in more detail the two experiments and form a comprehensive picture of the electron-phonon interaction mechanism for the soliton trains. First, we will present the behavior of the soliton-induced luminescence as a function of the applied magnetic field, the two-level density N^* , and the intensity of the ultrafast pump-laser. The differences between the soliton-induced luminescence and their induced luminescence *after* mode-conversion will subsequently be discussed in Sec. 7.4.3, relying on the coherent interaction model that was introduced in Chapter 6 and extended in Sec. 7.2.

7.4.1 Magnetic field dependence

The dependence of the decay of bottlenecked 29-cm⁻¹ phonons on an applied external magnetic field has been extensively studied many years ago [12, 13, 16, 17]. The magnetic field induces a Zeeman splitting of both the $\bar{E}(^2E)$ levels and the $2\bar{A}(^2E)$ levels, introducing a symmetric quartet in the crystal-field resonance with transition energies $\hbar\omega = \Delta_0 \pm \frac{1}{2}(g_{\bar{E}} \pm g_{2\bar{A}})\mu_B H$, with the gyromagnetic constants $g_{\bar{E}} = 2.445$ and $g_{2\bar{A}} = 1.6$ for $\vec{H} \parallel c$ and $g_{\bar{E},2\bar{A}} \approx 0.06$ for $\vec{H} \perp c$ [18]. It was shown, both in heat pulse and in steady state experiments, that a small field of ~ 0.05 T results for the resonant phonons in a nearly fourfold decrease of the bottleneck efficiency and decay time [12, 16, 17]. This strong effect was attributed to the spectral splitting of the homogeneously broadened resonances into four independent spectral regions of the phonon bottleneck, each communicating with a reduced number of level systems N^* and thus experiencing a longer absorption mean-free path. In the stationary experiments, this effect appeared as a reduction in the bottlenecked R_2 -luminescence intensity, while in time-resolved heat-pulse experiments the field turned out to reduce the bottleneck decay time τ . At higher magnetic fields (0.2 - 5 T), several other physical mechanisms have been identified, including spectral diffusion, Raman processes, and coupled Cr^{3+} -pairs [12, 13, 19], that makes the bottleneck factor to recover virtually to its $H = 0$ -value.

This brief historical sketch shows that the phonon bottleneck itself is already a quite complex phenomenon and may easily obscure a straightforward interpretation of soliton-TLS interaction that is relevant in the present work. Therefore, we confine ourselves to study only the magnetic field dependence at low fields, i.e. in the range 0 - 0.5 T over which the degeneracy of the quartet is lifted, but high-field effects are not yet prominent. Unfortunately, this does not eliminate yet

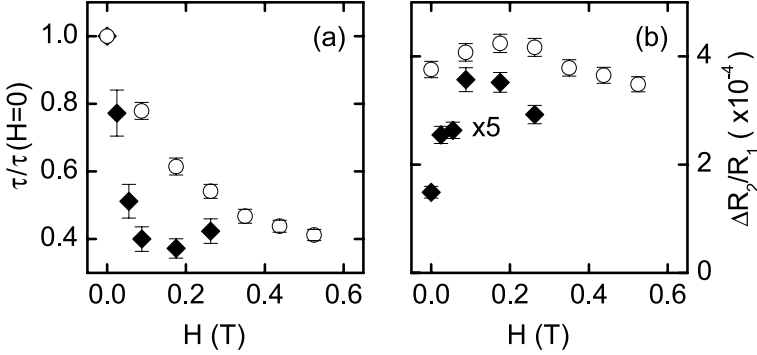


FIGURE 7.4 (a) Bottleneck decay time τ normalized to $H = 0$ value and (b) soliton-induced R_2 intensity normalized to R_1 as a function of applied magnetic field B , for propagation along c axis (\blacklozenge) and a axis (\circ). Connected symbols denote TA peak amplitude.

another complication, namely the fact that in the experiment in the a -axis configuration, the magnetic field is oriented nearly perpendicular to the c axis by the construction of our superconducting, split-coil magnet in the cryostat. Due to the low gyromagnetic constants in the a -direction, the level splitting only weakly depends on the applied field. To overcome this problem, we deviated the angle and made it several degrees between \vec{H} and the a axis. The results for both orientations are shown in Fig. 7.4(a,b), measured at the far end of the crystal and on the edge of the sample for the c axis configuration. Indeed, a significantly higher field is required to reduce the bottleneck decay time in the a -axis compared to the c -axis configuration, but comparable reductions of the bottleneck decay time are obtained within the range of moderate fields under study. In absence of the magnetic field, we measure $\tau(H = 0) \approx 0.25 \mu\text{s}$ along the c axis and an almost two-times-as-large value along the a axis. This can be accounted for by the reduction in volume size in the on-edge c -axis configuration, reducing the escape time of resonant phonons to the bath.

Consistent with our earlier findings, the absolute R_2 intensity in the two configurations differs by almost an order of magnitude [see Fig. 7.4(b)]. This we will denote as main observation (i). However, a new effect appears when the applied field is varied. For the case of propagation along the c axis, the R_2/R_1 -ratio increases by a factor of ~ 2.5 when applying of a field of 0.15 T. In the a -axis configuration, only a small variation is observed around a mean value of 4×10^{-4} .

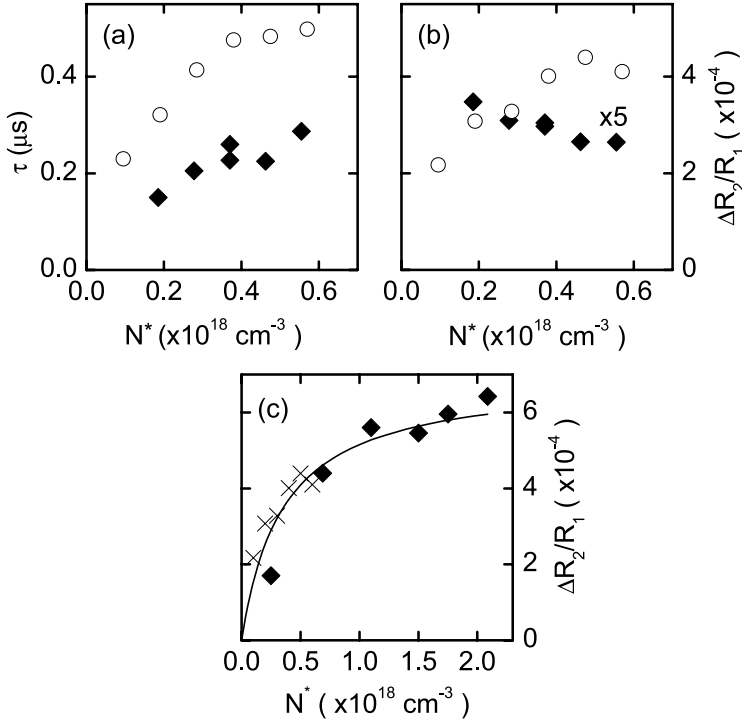


FIGURE 7.5 (a) Bottleneck decay time τ and (b) soliton-induced R_2 intensity normalized to R_1 as a function of Cr^{3+} concentration N^* , for propagation along c axis (\blacklozenge) and a axis (\circ). (c) Same as (b), but for larger range of N^* , for propagation along a axis (\blacklozenge), combined with experimental a axis-data (\times) of (b). (Line) denotes fit using the phonon bottleneck equation, Eq. (7.5).

The origin of this qualitative difference in the field-dependence of the signal intensity will be discussed below (c.f. Sec. 7.4.3) in terms of the intrinsic nonlinearity of the soliton propagation. For further discussion, we denote this magnetic-field dependence as observation (ii).

7.4.2 N^* and pump-power dependence

At this point, we explore the dependence of the signals on the concentration of excited Cr^{3+} -ions N^* . For both configurations, we varied the excited-state population N^* between 0.2 and $0.7 \times 10^{18} \text{ cm}^{-3}$. The results of the measurements, each taken at the same spots in the crystal as in Sec. 7.4.1, are shown in Fig. 7.5(a,b). As

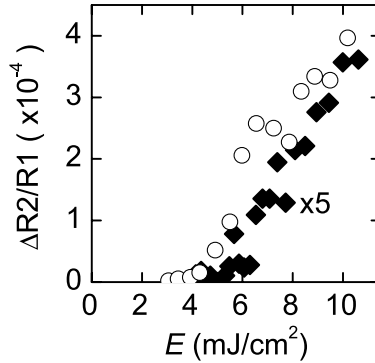


FIGURE 7.6 Dependence of soliton-induced R_2/R_1 -ratio on pump fluence E , for propagation along c axis (◆) and a axis (○).

in Fig. 7.4, there is a factor of 2 difference in bottleneck decay time caused by the reduced zone diameter in the c axis configuration. The *relative* increase in decay time with increasing N^* , however, appears to be the same for both configurations and is indicative of a decrease in mean free path for the resonant phonons and a stronger imprisonment. Similar to observation (ii) in Sec. 7.4.1, the main difference between the two configurations takes place in the *amplitude*-behavior of the soliton-induced signal. In the c -axis experiment, the soliton-induced LA peak is seen to *decrease* slightly. In the a -axis configuration, however, the luminescence ratio *increases* by more than a factor of 2. This difference in the N^* -dependence of the soliton-induced luminescence ratios will be referred to as observation (iii).

In the a -axis configuration we also measured the soliton-induced signal up to much higher values of N^* [see Fig. 7.5(c)]. Combined with the data of Fig. 7.5(b), Fig. 7.5(c) displays the dependence of $\Delta R_2/R_1$ for N^* varying from 0.2 to $2 \times 10^{18} \text{ cm}^{-3}$. Clearly, the signal saturates at excited-state concentrations higher than $0.6 \times 10^{18} \text{ cm}^{-3}$. At this point we also note the strong resemblance of the increase of the intensity in Figs. 7.5(b) with that of the bottleneck decay time in Figs. 7.5(a), again for the a axis configuration. As we will demonstrate at the end of Sec. 7.4.3, this resemblance can be traced back to the concentration-dependence of the phonon bottleneck [line in Fig. 7.5(c)].

Finally, we present in Fig. 7.6 the soliton-induced luminescence as a function of intensity of the femtosecond pump-laser, in both a - and c -axis configurations. The results along the a axis were presented earlier in Fig. 6.1(b) of Chapter 6. In

both data series, there is a clear threshold below which soliton-induced luminescence is absent. The threshold is located at a slightly higher pump fluence in the case of pulses travelling along the c axis. This may be explained by the slightly lower nonlinear constant α in this direction in the crystal ($\alpha = -2.37$ TPa along the a axis and -1.84 TPa along the c axis [20]), thus requiring a larger strain to reach the 0.87 THz frequency components in the solitons. As discussed in Sec. 6.3, the threshold in the pump-dependence of the signal demonstrates that the excitation is critically dependent on the availability of 0.87-THz frequency components in the soliton spectrum and thus on the ultrashort time duration of the incident strain pulses.

7.4.3 Discussion

The above experiments lead to the following three observations in connection to the interaction between the electronic system and the solitons: (i) the absolute signal along the c axis is typically one order of magnitude lower than along the a axis; (ii) the Zeeman-splitting of the electronic levels by a magnetic field results in an *increase* in soliton-induced luminescence signal only in the c axis configuration; (iii) a higher concentration N^* results in an *increase* of the signal only in the a axis configuration. In the discussion, we will assume that in the a -axis configuration the $2\bar{A}$ -population is *impulsively* excited by the solitons, while in the c -axis configuration it is caused by an incoherent, *fixed* phonon spectrum. In the experiments of Chapter 6, the soliton signal was found to survive the traversal through an additional excited volume and even long-distance propagation through a collinear pencil. As an explanation, it was proposed that the intrinsic nonlinearity of the soliton pulses is responsible for refilling the spectral hole caused by resonant absorption followed by spontaneous emission, that efficiently funnels energy from the soliton-pulse spectrum to the resonant 29-cm⁻¹ phonons in the bottleneck.

At this point we will demonstrate that the observations (i)-(iii) for the two configurations can be brought in good agreement with the model proposed in Sec. 7.2. First of all, the difference in absolute luminescence intensity (i) can be explained from the calculations of the total removed energy as shown in Fig. 7.1(c). Given the resonant mean free path of $\bar{l}_r \approx 2 \mu\text{m}$ for longitudinal acoustic phonons (see Appendix B) and a zone diameter of $200 \mu\text{m}$, the travelled distance is of the order of one hundred Beer's lengths. The energy deposited into the phonon bottleneck after $z \approx 100\bar{l}_r$ is one order of magnitude less for the linear pulse than for the

soliton, which agrees well with the observed difference in R_2 luminescence in the c - and a -axis configurations.

The magnetic-field dependence of point (ii) reveals yet another aspect of the soliton-TLS interaction. The increase of the luminescence intensity by a factor of 2.5 in the c -axis configuration can be well understood from the point of view of available phonon modes. In the absence of refilling, a bandwidth around the absorption line will be completely depleted of phonons. The excited-state population of the electronic system is therefore limited by the available resonant phonons within the absorption bandwidth. The splitting of the electronic levels by an external magnetic field will lead to an increase of the amount of available phonons once this splitting exceeds the absorption bandwidth. In contrast, for the nonlinear solitons, the spectral absorption bandwidth is continuously replenished from other parts of the spectrum. Therefore the excited-state population is not limited by the amount of phonon modes that are available, and no dependence on magnetic field is observed.

Finally, the dependence of the luminescence ratio on the excited-state concentration N^* [observation (iii)] can be explained by the most fundamental difference found in Sec. 7.2, namely that, due to the nonlinear refilling, the energy is removed much faster from the soliton wavepacket through spontaneous emission than from a linear strain pulse. For the linear pulse, after the first few micrometers, spontaneous emission only takes place in the wings of the resonance lineshape, resulting in an electronic excitation proportional to $(N^*)^{1/2}$ [c.f. Eq. (7.2)]. As the R_1 intensity is proportional to the excited-state population N^* , the normalized ratio should go as $(N^*)^{-1/2}$. Indeed a decrease is observed in Fig. 7.5(b) for the c -axis configuration.

For the soliton pulses, the energy funnelled to the phonon bottleneck is *linearly* proportional to the number of centers N^* [c.f. Fig. 7.1(c)], and thus the R_2 -luminescence intensity normalized to R_1 should be independent of N^* . However, Fig. 7.5(c) shows an *increasing* ratio that is not predicted by the refill model. We believe that the increase of the signal with N^* along the a axis reflects a fundamental property of the phonon bottleneck, which we will explain below.

A simple rate-equation analysis shows that the incoherent 29-cm^{-1} phonon energy extracted from the solitons is redistributed equally over the phonon bath and the electronic centers, yielding a ratio of the electronic populations according to

$$\frac{N_{2\bar{A}}}{N_{\bar{E}}} = \frac{\Delta w}{2} \frac{N^*}{N^* + \rho\Delta\nu}, \quad (7.5)$$

with $\rho\Delta\nu$ the Debye density of states around the 0.87 THz phonon frequency. In this balance, the critical parameter is the bandwidth $\Delta\nu$ over which the coherent electronic polarization tail is converted to phonons. We find good agreement with the experimentally observed behavior for $\Delta\nu \approx 10$ GHz (line in Fig. 7.5(c)) and a $\Delta w/2$ of 7×10^{-3} . This bandwidth is higher than the inhomogeneous linewidth of the transition of 0.3 GHz [21], but is in the ball park of the Kramers-doublet splitting in the applied magnetic field.

The resemblance of the behavior of the bottleneck decay time with the N^* -dependence of the R_2/R_1 -ratio in Fig. 7.5(a,b) is no coincidence in this framework. The bottleneck decay time is strongly connected to the detailed balance between spin- and phonon-baths, which can be appreciated from the fact that the ratio $\rho\Delta\nu/N^*$, appearing on the right side of Eq. (7.5) reflects the relative ‘trapping’ ratio τ_r/T_1 [12], with $\tau_r = \bar{l}_r/c_0$ the resonant absorption time and T_1 the spontaneous-emission lifetime. This ratio describes the fraction of time that a resonant energy-quantum resides in the phonon state. The phonon ‘escape’ time τ , constituted of spatial diffusion and anharmonic decay, is slowed down with increasing N^* by exactly the same ratio as the luminescence intensity in Eq. (7.5), due to the increasing amount of time the energy quantum spends in the electronic state, where it is immune to phonon-escape processes.

Apparently, the enhancement of the trapping efficiency of Eq. (7.5) will apply to all the above experimental configurations, irrespective of the origin of the 29-cm⁻¹ phonons. This includes the N^* -dependence of the luminescence ratio in the c -axis configuration, shown in Fig. 7.5(b). Indeed, the decrease of the R_2/R_1 -ratio is not as strong as predicted by the energy considerations of Sec. 7.2. The bottleneck factor of Eq. (7.5) may account for this deviation and is therefore not in disagreement with the above interpretations.

As a final remark we wish to point out that the luminescence induced by the heat pulse (not shown) does not always show the same behavior as the soliton signal in the c -axis configuration. However, the observed behavior turns out to be consistent when we take into account the fact that the heat pulse is much longer than the bottleneck decay time. As a result, the heat pulse signal consists of a convolution of the dynamics of the phonon bottleneck with the slowly varying pulse shape, in contrast to the soliton-induced signal, that is extremely well defined by its ultrashort strain profile.

7.5 Conclusions and prospects

In conclusion, we have studied the interaction of ultrashort strain solitons and the electronic $\bar{E}(^2E) - 2\bar{A}(^2E)$ -transition along the ruby c axis and compared it with the case of propagation along the a axis of Chapter 6. The absence of soliton-induced luminescence in the bulk of the crystal is consistent with the suppression of the interaction due to the selection rules of the trigonal point group. The observation of a signal near the far end of the crystal has been explained by the increased coupling of the reflected wave due to diffusive scattering and mode-conversion at the surface roughness. Further, the observed signals in both the c - and a -axis configurations have been compared as a function of magnetic field and excited-state concentration, and the observed differences were found to be consistent with the presented model based on the nonlinear properties of the solitons.

References

- [1] H.-Y. Hao and H. J. Maris, Phys. Rev. B **64**, 064302 (2001).
- [2] O. L. Muskens and J. I. Dijkhuis, Phys. Rev. Lett. **89**, 285504 (2002).
- [3] K. Hasenburger, E. Sigmund, and G. Mahler, Phys. Rev. B **41**, 3627 (1990).
- [4] N. S. Shiren, Phys. Rev. B **2**, 2471 (1970).
- [5] L. Allen and J. H. Eberly, *Optical Resonance and Two-Level Atoms* (General Publishing Company, 1987), 2nd ed.
- [6] P. Hu, Phys. Rev. Lett. **44**, 417 (1980).
- [7] M. H. F. Overwijk, J. I. Dijkhuis, and H. W. de Wijn, Phys. Rev. Lett. **65**, 2015 (1990).
- [8] D. C. Burnham and R. Y. Chiao, Phys. Rev. **188**, 667 (1969).
- [9] M. Crisp, Phys. Rev. A **1**, 1604 (1970).
- [10] F. T. Arecchi and E. Courtens, Phys. Rev. A **2**, 1730 (1970).
- [11] J. D. Jackson, *Classical Electrodynamics* (John Wiley & Sons, 1998), 3rd ed.
- [12] A. A. Kaplyanskii and S. A. Basun, in *Nonequilibrium Phonons in Nonmetallic Crystals*, ed. W. Eisenmenger and A. A. Kaplyanskii (North Holland, 1986) p. 373.
- [13] R. J. G. Goossens, J. I. Dijkhuis, and H. W. de Wijn, Phys. Rev. B **32**, 7065 (1985).
- [14] A. F. G. Wyatt, *Nonequilibrium Superconductivity, Phonons and Kapitza Boundaries* (Plenum, 1981), p. 31.
- [15] T. Nakayama, Phys. Rev. B **33**, 8664 (1986).
- [16] J. I. Dijkhuis, A. van der Pol, and H. W. de Wijn, Phys. Rev. Lett. **37**, 1554 (1976).
- [17] J. I. Dijkhuis, K. Huibregtse, and H. W. de Wijn, Phys. Rev. B **20**, 1835 (1979).
- [18] S. Geschwind, G. E. Devlin, R. L. Cohen, and S. R. Chinn, Phys. Rev. **137**, A1087 (1965).

- [19] R. S. Meltzer, J. E. Rives, and W. C. Egbert, *Phys. Rev. B* **25**, 3026 (1982).
- [20] J. M. Winey, Y. M. Gupta, and D. E. Hare, *J. Appl. Phys.* **90**, 3109 (2001).
- [21] M. J. van Dort, J. I. Dijkhuis, and H. W. de Wijn, *Phys. Rev. B* **41**, 8657 (1990).

CHAPTER 8

ULTRAFAST PUMP-PROBE REFLECTOMETRY OF STRAIN WAVEPACKETS

Abstract

We describe an experimental setup for the detection of ultrashort strain pulses by means of femtosecond pump-probe reflectometry. The principle of operation and noise-reduction methods are explained. Preliminary experimental results on strain pulses generated by high-power femtosecond laser pulses in a chromium film are presented and compared with theory and with previous experiments at low pump intensities.

8.1 Introduction

After the demonstration of picosecond acoustic wavepacket development into soliton trains using Brillouin light-scattering in Chapters 4 and 5, and the direct observation of terahertz frequency components by means of the ruby phonon spectrometer in Chapters 6 and 7, the next step would be to detect the solitons *in the time-domain* as they arrive at the far-end of the crystal. The detection of very short acoustic pulses using time-resolved pump-probe reflectometry is common practice and has already been used to demonstrate soliton development at relatively low strain amplitudes in Ref. [1]. In this chapter we present a new and improved setup for the detection of small ultrafast transients using a low repetition-rate, amplified laser system, and demonstrate its successful operation by means of some explorative studies on strain-pulse generation in a thin chromium transducer.

8.2 Theory of ultrafast elasto-optic strain detection

The detection of short strain pulses using the elasto-optic effect in a metal film has long been considered impossible as the strain at a free surface is always equal to zero. However, the finite optical penetration depth turned out to be sufficient to generate a seizable strain-induced modulation in the reflected intensity. The theory of ultrafast strain detection using this transient reflectometry method was developed by Thomsen *et al.* [2]. Here, the change in reflectivity is considered as a spatial convolution of the strain packet $s(z, t)$ with the response function $f(z)$ of the metal at each time t , given by

$$\Delta R(t)/R = \int_0^{\infty} f(z)s(z, t)dz. \quad (8.1)$$

The sensitivity function $f(z)$ depends on the complex dielectric and elasto-optic material parameters at the selected optical wavelength and is given by

$$f(z) = f_0 \operatorname{Re} \left(\frac{\partial n}{\partial s} \sin(2knz - \phi) + \frac{\partial \kappa}{\partial s} \cos(2knz - \phi) \right) e^{-z/\zeta}$$

$$f_0 = 8k \frac{[n^2(n^2 + \kappa^2 - 1)^2 + \kappa^2(n^2 + \kappa^2 + 1)^2]^{1/2}}{[(n + 1)^2 + \kappa^2]^2} \quad (8.2)$$

$$\tan \phi = \frac{\kappa(n^2 + \kappa^2 + 1)}{n(n^2 + \kappa^2 - 1)},$$

with k the optical wavevector, $n + i\kappa$ the complex index of refraction of the metal, $\zeta = (2k\kappa)^{-1}$ the optical skin depth, and $\partial n/\partial s$, $\partial \kappa/\partial s$ the elasto-optic coefficients.

Let us consider what kind of reflectivity signals can be expected for the typical strain waveforms as presented in this thesis. In view of the experiments later on in this chapter, we calculated the transient reflectivity in two cases: for a thick chromium film and for a 5-nm thin aluminium film. The material parameters relevant for these and other calculations in this chapter are given in Table 8.1. Figure 8.1 shows the calculated reflectivity traces for the normal, bipolar strain pulse, the Burgers N-wave, and finally the ultrashort soliton. It can be seen that the reflectivity signals strongly depend on the precise pulse shape, and behave like the derivative of the strain waveform. The highest peak amplitudes are found for the bipolar, Gaussian-derivative waveform, where the effect of the two phases adds up

	Cr	Al	Al ₂ O ₃	PbMoO ₄
ρ ($\times 10^3$ kg/m ³)	7.2	2.7	3.97	6.95
c_0 ($\times 10^3$ m/s)	5.9	6.42	11.23	3.64
Z ($\times 10^7$ kg/m ² s)	4.25	1.76	4.46	2.52
$n + ik$	$3.2 + 3.3i$	$2.7 + 8.4i$		
$\frac{\partial n}{\partial s} + i \frac{\partial k}{\partial s}$	$6.5 - 4.2i$ [3]	$-20.9 + 11.2i$ [4]		

TABLE 8.1 Material parameters ρ , c_0 , and resulting impedance Z for the metals and substrates under study, as well as complex index of refraction $n + ik$ and strain derivatives for the metal films.

at zero time. For the other, evolved waveforms this constructive interference does not take place and concomitantly the expected signals are significantly smaller. Furthermore, the simulated reflectometry signals originating from the chromium and aluminium films have an opposite sign, which is a consequence of the different signs of the elasto-optic coefficients, as shown in Table 8.1.

8.3 Experimental setup

8.3.1 Introduction

Most picosecond ultrasonics setups are built around a commercial modelocked Ti:sapphire oscillator, and take advantage of high-frequency modulation techniques and lock-in signal recovery. Sophisticated signal recovery methods are indispensable for picosecond ultrasonics, as acoustic vibrations produce only minute changes in the optical reflectivity, typically of the order of the strain amplitude reached ($10^{-5} - 10^{-6}$ in conventional picosecond ultrasonics). The sensitivity of the setup further depends on the elasto-optic coupling strength of the reflecting film at the selected probe wavelength. In some metals, for example in copper, this coefficient is nearly zero at the wavelength of a Ti:sapphire oscillator (~ 800 nm). In these situations, however, acoustic pulses may be detected through the surface displacement, using interferometric techniques. Mach-Zehnder[5–7], Michelson [8, 9] and Sagnac [10–14] interferometers have been successfully applied in ultra-fast pump-probe setups. However, in many cases, interferometry may be avoided

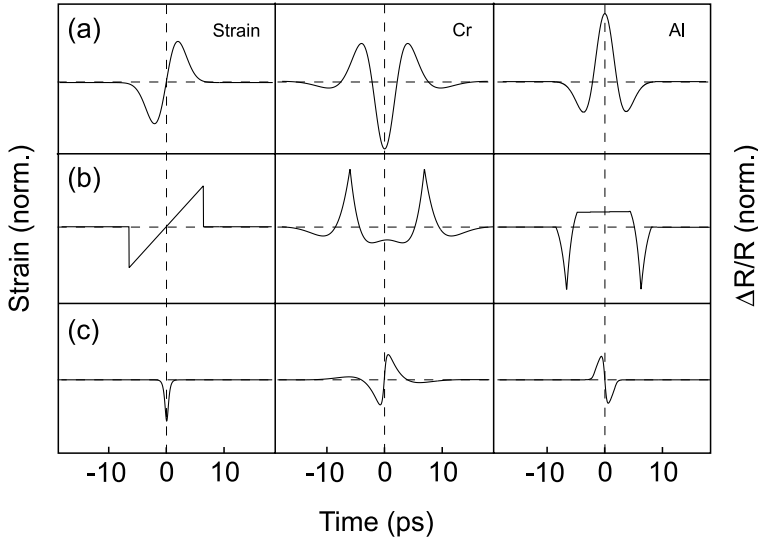


FIGURE 8.1 Calculated transient reflectivity signals for typical strain waveforms: (a) normal bipolar pulse, (b) N-shaped pulse (shockwave), and (c) Single ultrafast strain soliton. Vertical scale (a-c) is normalized to the maximum strain amplitude, with convenient multiplication constants for Cr- and Al-reflectivity traces.

and reflectometry provides with sufficiently large signals.

Low-repetition rate, amplified Ti:sapphire lasers have up to this point not been applied in picosecond ultrasonics experiments. Our aim is to detect high-amplitude, ultrashort strain pulses generated using high-power laser pulses in a low-repetition rate pump-probe reflectivity experiment. To construct such a setup with sufficient sensitivity to detect the inherently small, strain-induced modulations is quite a challenge for a 1-kHz regenerative amplifier. Several fundamental principles play a decisive role here:

1. **Low-frequency noise:** It is well-known that the intensity noise of the pump laser and the inevitable mechanical vibrations of the setup reduce significantly at high frequencies. A low-frequency modulation experiment therefore inherently suffers from a larger noise than a high-frequency experiment.
2. **Poisson noise:** When each individual event produces a statistical fluctuation S of a signal I , it is useful to average over a large number N of such

independent events, as the fluctuation S grows with $N^{1/2}$, while the signal I is proportional to N . Assuming an identical fluctuation per event, the 80-MHz system has 8×10^4 more events per second, signal averaging thus gives a 3×10^2 better improvement of the signal-to-noise ratio than the 1-kHz system.

However, there are some advantages of a low-repetition setup that may be used to compensate for some of the above limitations:

1. **Pulse-based corrections:** The repetition rate is low enough to allow fast electronics to keep track of the individual events and to correct for pulse-to-pulse fluctuations. A reference detector can be used to correct for the statistical fluctuations of the setup, partly eliminating the intensity fluctuations of the laser.
2. **High-sensitivity analysis:** The long time between subsequent events allows for high-sensitivity sampling of the obtained signals. The digital voltmeters that we will use can read out voltages over a short (μs) gate period with an accuracy of up to 5 digits per shot, allowing for an excellent sensitivity in the data acquisition process.

8.3.2 Principle of operation

In this section we describe the principle of operation of the pump-probe setup developed for our 1-kHz Ti:sapphire regenerative amplifier system. The approach to the data-acquisition using our discrete sampling method is compared to the usual lock-in signal-recovery techniques. We present both time- and frequency-domain arguments to show that the described method is preferable in a low-repetition rate, ultrafast experiment.

First, let us consider the idea behind lock-in detection. When an 80-MHz optical pulse train is detected by a photodiode with a response time slower than the fundamental period, it will generate a dc voltage proportional to the average illumination intensity. If a small, pump-induced change is to be detected in this pulse train, one usually modulates the pump at a frequency f , well within the response bandwidth of the detector. A square modulation function [see Fig. 8.2(a)] will produce sidebands around the dc-component in the form of a harmonic $1/n$ -sequence of the modulation frequency f . For the extraction of these sidebands, one uses a lock-in amplifier, that can determine the electric power P in a selected

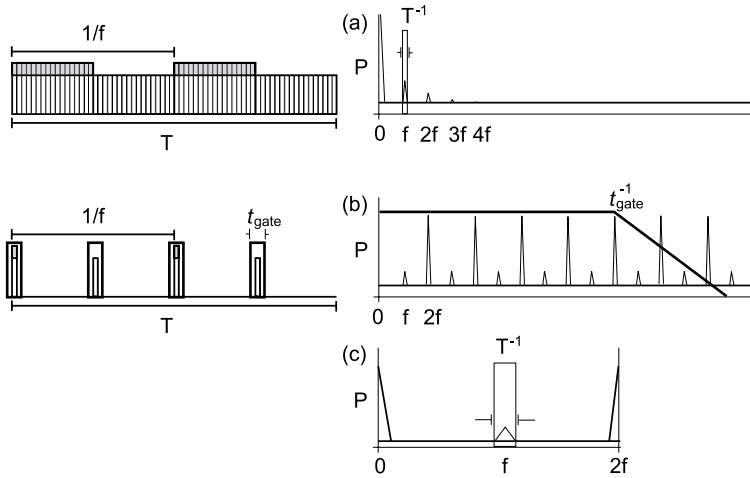


FIGURE 8.2 Principle difference between lock-in signal extraction (a) and discrete sampling method (b,c). (a) High repetition-rate pulses with low-frequency modulation and detection (left) gives spectrum with single modulation frequency, suitable for lock-in detection (right). (b) Low repetition-rate, short pulses (left) give frequency comb with many modulation sidebands. Gated detection with sampling rate $2f$ results in folding of spectrum into a ‘zone’ $[0,2f]$ [see (c)], and reduction of noise by factor $(2ft_{\text{Gate}})^{-1/2}$ relative to lock-in detection (see text).

frequency bandwidth proportional to T^{-1} , where T denotes the integration time. As the signal itself is a sharp peaked function while the noise is a constant background level, the r.m.s. signal-to-noise ratio of the voltage modulation, i.e. of $\Delta R/R$, is proportional to $T^{-1/2}$. For a flat spectrum of background noise, the total noise rejection is given by the square root of the ratio of the lock-in bandwidth T^{-1} to the total photodetector bandwidth.

In case the repetition period of the pulses is larger than the detector response time, as for a train of ultrashort pulses with a low repetition frequency, we find a completely different picture. We then observe a frequency comb consisting of many harmonics of the fundamental repetition frequency, defined here as $2f$ [see Fig. 8.2(b)]. The exact number of these harmonics, say Q , is given by the ratio of the repetition period and the response time of the detector. If we apply now a modulation of the intensity at a frequency f , each harmonic in the comb will produce sidebands. Now to extract the signal at f using a lock-in detector would be a waste of potential, as it will only recover the amplitude of the first harmonic in the

spectrum, that is Q times lower, while the background noise remains the same. A much better approach is to recover the amplitude of *all* modulation peaks in the spectrum but with a very narrow bandwidth. This can be accomplished by the following procedure. First, one measures the intensities of the individual pulses using a triggered voltmeter with a gate width t_{Gate} [see Fig. 8.2(b)]. In fact, by sampling at a fixed frequency $2f$ we fold back the entire frequency spectrum onto the interval $[0, 2f]$ [as shown in Fig. 8.2(c)]. As in this process the phase is maintained, random fluctuations average out to a background growing only proportional to $Q^{1/2}$, the number of periods that are folded back. The peak intensity at f , however, will grow *linearly* proportional to the number of peaks Q . If we now subtract pairs of subsequent pulses with and without pump-induced effect, we recover the frequency component at f in the folded zone, with a signal-noise-ratio of $\Delta R/R$ again determined by the integration time $\propto T^{-1/2}$.

8.3.3 Setup

Figure 8.3 shows the experimental configuration for the pump-probe reflectometry experiments. We use the amplified Ti:sapphire system operating at 1 kHz as an energy source (pump) for ultrafast excitation of the sample. The pump beam is chopped at 1/4th of the repetition frequency, prescribed by the limited response time of the digitizing electronics in the detection stage. Therefore, subsequent pairs of two pulses are intermittently transmitted or reflected by the mechanical chopper blades, that are in turn synchronized to the amplifier electronics. Directly after the chopper, part of the pump light is reflected to a fast (nanosecond) photodetector, that is used to trigger the data acquisition system. The rest of the pump radiation is weakly focused onto the sample, i.e. to create strain pulses, where the intensity can be tuned by translation of the 1.6-m focusing lens.

As a probe we can choose to employ either a small fraction of the 1-kHz pulse train of the amplified laser, or, alternatively, pick the synchronized output of the 80-MHz seed oscillator of the regenerative amplifier. The repetition rate of this optical output is reduced and synchronized with the 1-kHz of the pump laser by means of a commercial pulse picker. By adjusting the timing of the acousto-optic output coupler inside the pulse picker, large delays between pump and probe can be set with discrete steps of 12.5 ns, the period in the modelocked pulse train. To cover the intermediate time delays between these 12.5-ns steps, we constructed an octuple-pass, 0.5-m long delay line, that can be controlled mechanically. After adjusting and fixing this delay line to the desired value, accurate scans can

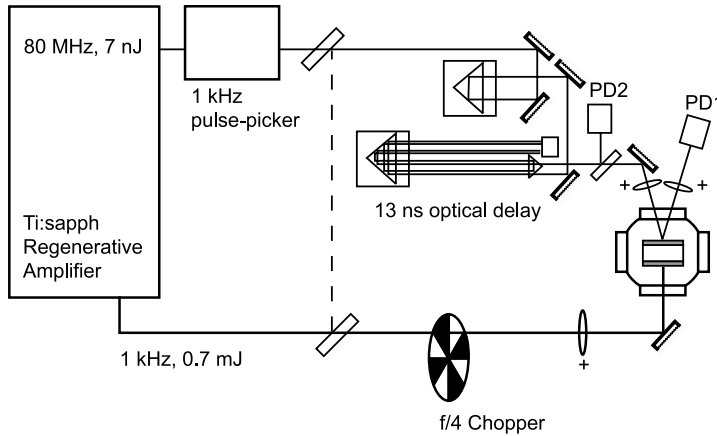


FIGURE 8.3 Experimental setup for pump-probe reflectometry experiments with long time delays, in the configuration where the probe is incident onto the sample at the opposite crystal surface as the pump. A pulse picker is used to select a single pulse of the 80-MHz train, synchronized to the 1-kHz pump, and at a well-defined time delay. The 4-m long, octuple-pass delay line is adjusted to cover the 12.5-ns time delay between the modelocked laser pulses. The short delay line is used to make computer-controlled scans.

be made over a ~ 1 -ns window by means of a 20-cm long, computer-controlled optical translation stage.

Prior to focusing onto the sample, a small part of the probe beam is split off and directed to a photodetector and used as a reference for pulse-based noise reduction. The rest of the probe beam is focused to a small spot (~ 0.1 mm in diameter) onto the sample. The sample may either be a transparent crystal covered on one side by a metallic film, or a crystal with metallic films deposited on the two opposite faces (the latter configuration is not used in this thesis). The probe beam can be directed onto the sample either at the same side or the opposite side as the pump beam, but is always kept under a small angle to prevent spurious pump light from entering into the detection system. The reflected probe light is collected using a lens and imaged onto a photodetector, of which the output is used to recover the pump-induced reflectivity changes of the sample.

The electronic signals from both the probe- and reference-detectors are sent to two independent digital multimeters. The detectors are used in photovoltaic mode to reduce shot noise and dark current contributions. Further, the decay time of the photoinduced voltage is adjusted to $20 \mu\text{s}$, the optimum length of the multimeters,

by means of a 100-k Ω load resistance at the multimeter input. The digital multimeters are controlled by a computer using IEEE (GPIB) communication ports and are set to measure and digitize DC voltage over a fixed time interval (gate), that can be tuned continuously down to 0.5 μ s. However, the accuracy of the ADC-conversion gradually decreases from 7 to 4.5 digits when reducing the gate window below 10 μ s. The multimeters were found to be limited in their measurement cycle for gated DC voltage measurements to a maximum repetition rate of about 0.7-kHz. Therefore it was decided to operate the whole setup at 0.5 kHz, and thus to modulate the pump beam at 0.25 kHz. Each multimeter can be set to work independently for a complete acquisition period of several seconds, and produces an array of measurement data that is subsequently transferred to the computer. However, for the pulse-based correction scheme to work, the multimeters have to be synchronized by an external trigger. This is provided by a 4-channel digital delay generator, that also is controlled by the computer using a GPIB connection. By appropriately setting the trigger moment of this unit, the two multimeters can be made to start measuring at the same time and produce synchronized arrays of probe- and reference-data. After being read out by the computer, the following computations are carried out to obtain the corrected probe signal: for each probe and reference pulse pair p_i, r_i the ratio $\eta_i = p_i/r_i$ is calculated, then the difference $\eta_{i+1} - \eta_i$ between a pulse with and without pump-effect is calculated to obtain the pump-induced signal. This difference is averaged over all events and finally multiplied by a factor correcting for the difference in illumination of probe and reference diodes, extracted from the ratio of the averages of probe- and reference-pairs for odd i , i.e. in absence of the pump pulse.

8.3.4 System performance

In order to demonstrate the operation of the pump-probe setup we performed several experiments on metallic layers of chromium and aluminium at room temperature. Figure 8.4 shows the effect of the pulse-based correction scheme for an extremely noisy data set, taken using the 1-kHz output of the amplified laser as a probe. We obtain a reduction of the background noise of a factor 50 and achieve an ultimate sensitivity of 2×10^{-5} in the reflectivity change $\Delta R/R$. The noise of the uncorrected probe and reference data originates from a combination of laser fluctuations and acoustical vibrations. The former strongly depends on the optimization of the amplified system and is largely beyond our control. The laser is specified to an accuracy of 1% in the energy fluctuation per shot, which results

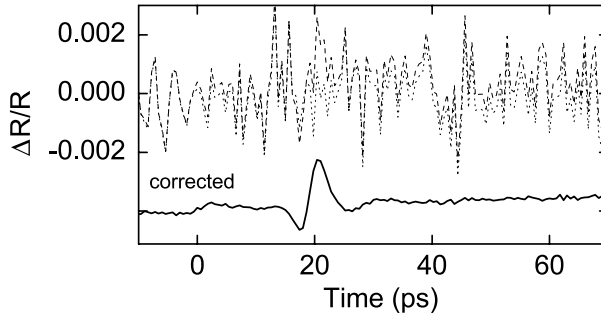


FIGURE 8.4 Typical probe (dash), reference (dots), and corrected signal (solid) trace for an acoustic pulse in a 100-nm Cr / 5-nm Al-film for *sapphire-side* pump, *metal-side* probe configuration. A 50-fold reduction of the noise, from $\sim 10^{-3}$ to 2×10^{-5} in the signal, is achieved using an acquisition time of 0.8-s per data point.

in a relative noise background of 5×10^{-4} over 500 shots. Spurious contributions may also originate from the long optical delay lines, in combination with the angular fluctuation ('pointing jitter') inherent to the amplified laser system. The above fluctuations can be lower by a factor of ~ 5 when all components are well optimized, but has never reached below a minimum of 6×10^{-3} per pulse. Thus, in all practical situations, the pulse-based correction scheme turns out an absolute prerequisite to obtain the low background noise necessary for strain pulse detection.

8.4 Experiments

8.4.1 Characterization of strain pulses

In the analysis of our Brillouin scattering data of Chapter 4, we have relied on numerical simulations of the development of an initial wavepacket into a train of solitons. The exact shape and width of this input pulse was at that point not yet experimentally checked in the time domain, although there existed some literature on the ultrafast excitation of chromium films [3, 15, 16]. To verify the behavior at high-intensity excitation and for our films, we first used our pump-probe setup to determine the pulse echoes from the sample used in our Brillouin experiments. This was done in the configuration where both pump- and probe-pulses were incident on the metal film from the air. However, the acoustic reflection

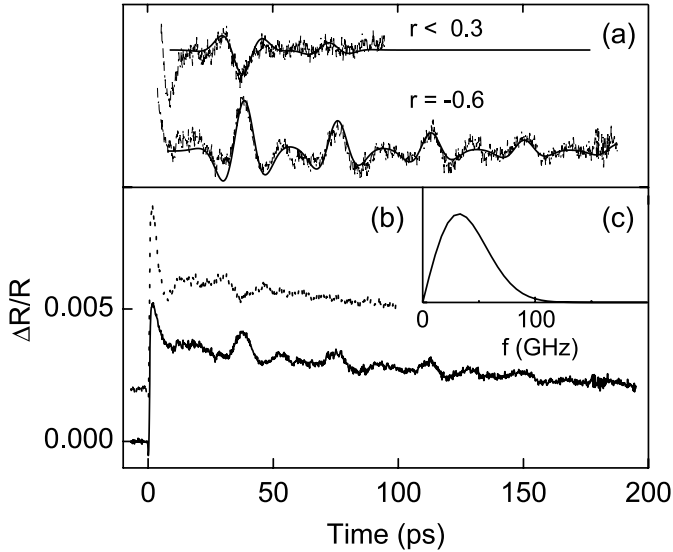


FIGURE 8.5 Pump-probe reflectivity data for front-side excitation and detection of a 100-nm chromium film on lead molybdate (line) and sapphire (dash) single crystals. (a) Signals after subtraction of slow background. Lines denote fits to data according to Eq. (8.1). (b) Original data, including electronic background. (c) Amplitude-spectrum of the strain wavepackets obtained from fitting the data of (a).

at the chromium-sapphire interface turned out to be very small, and the acoustic echoes could barely be detected. Therefore, we also performed an experiment on a chromium film evaporated onto a piece of lead molybdate, that is expected to give stronger acoustic echoes from the crystal-chromium interface. For an interface that is flat on the scale of the typical strain wavelength, we may estimate the acoustic reflection coefficient from the impedance law [17]:

$$R_{ij} = \frac{Z_j - Z_i}{Z_j + Z_i}, \quad (8.3)$$

where $Z_i = \rho c_0$ is the acoustic impedance of the material i . The typical values for the metals and substrates in this experiment are shown in Table 8.1, and predict a reflection coefficient of 0.11 for the Cr- Al_2O_3 interface and -0.26 for the Cr- PbMoO_4 interface. The experimentally obtained traces, shown in Fig. 8.5, give the expected result. Indeed, there is a 180° phase difference between the echoes

observed from two samples, but the absolute reflection coefficients are higher in the experiment than expected from the theoretical considerations. This may be due to a reduced mechanical attachment of the metal films onto the substrate. Nevertheless, for the sapphire sample the reflections are small enough to justify our simple interpretation of the Brillouin experiment, disregarding the presence of acoustic echoes in the input strain pulse.

The trains of reflected pulses can be simulated using the formulas for transient reflectometry of Sec. 8.2. Here, the exact magnitude of the optical and opto-elastic material constants may depend on the deposition parameters and on the quality of individual films and have been adjusted within 10% of their literature values to fit the experiment (see Table 8.1). Good agreement has been obtained with the experimental traces of Fig. 8.5(a), where the electronic background has been subtracted, for a Gaussian derivative strain waveform with time constant $\tau_g = 7$ ps. This is in agreement with the initial strain waveform used in our simulations for the Brillouin experiment [c.f. 4.2]. The frequency spectrum of this resulting waveform is shown in the inset of Fig. 8.5(c) and compares well with that obtained in the low-intensity experiments [3], be it that our spectrum seems to peak at a slightly lower frequency (30 GHz instead of ~ 40 GHz). This may indicate a slightly larger diffusion of energy within the electron-phonon interaction time, due to the exceptionally strong nonequilibrium excitation of the electron gas by the high-power laser pulses. However, a detailed analysis of these effects lies beyond the scope of this thesis.

As a second issue, we wish to investigate if there could be a better material than chromium to detect the ultrashort strain pulses after they have developed in the bulk of a crystal. The skin depth of chromium is twice longer than that of aluminium, which has the highest κ of all metals [c.f. Fig. 8.6(c)]. Therefore, an aluminium thin-film may be more sensitive to higher acoustic frequency components, and thus more suitable to detect ultrashort strain solitons. As a try-out, we compared the response of a 100-nm chromium film with a similar film, but coated by a 5 ± 2 -nm thin layer of aluminium. In both cases, the substrate is a 100- μm sapphire crystal, with the c axis aligned perpendicular to the surface. We excite the films from the sapphire-chromium side, therefore the generated strain pulses should be the same in both configurations. The reflectivity is probed at the outside, and thus is sensitive to the elasto-optic response of the outer metals, i.e. Cr or Al. This configuration has the additional advantage that the *original* strain pulses can be detected, rather than the echoes. Another feature is the virtual absence of

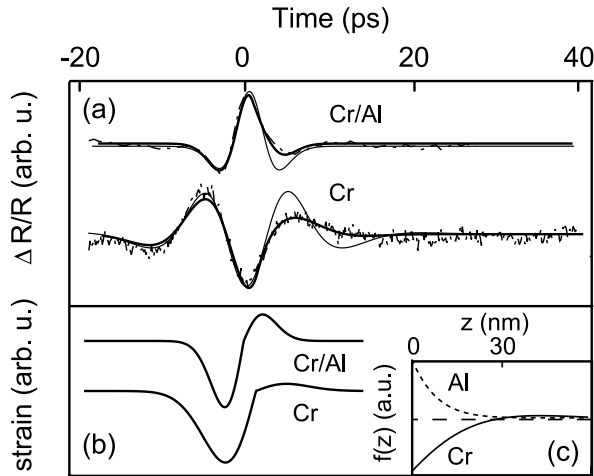


FIGURE 8.6 (a) Pump-probe reflectivity data for crystal-side pump and surface probe, in case of a normal 100-nm chromium film (Cr) and one that is covered with a 5-nm top layer of aluminium (Cr/Al). Lines are fits to Eq. (8.1), for symmetric (thin line) and asymmetric (thick line) waveforms, the latter shown in (b). (c) Response functions $f(z)$ for chromium and aluminium.

an electronic or thermal background, as the Cr-film is much thicker than the electronic diffusion length. The deposited heat diffuses through the film in the form of high-frequency phonons and arrives much later than the ballistic strain packets [as will be shown in Fig. 8.7]. Figure 8.6(a) shows the reflectivity traces for the two samples, denoted by Cr and Cr/Al. Strikingly, the polarity of the two signals is inverted with respect to each other, which is a result of the sign of the elasto-optic coefficients (c.f. Table 8.1). Further, it is observed that the detected waveforms are not symmetric. For a normal, bipolar pulse (thin line), the reflectivity signal would consist of two equal lobes on both sides of the maximum, and clearly is inconsistent with the experimentally observed behavior, both for the Cr and Cr/Al case. However, the chromium-sapphire interface is not a free surface, therefore the initial compression pulse will not be reflected as it would at the outside of the sample.

Indeed, the experimental traces can be explained well by the strain waveforms shown in Fig. 8.6(b). Strikingly, the obtained wavepacket still is bipolar, which is in contradiction to the impedances of Table 8.1 and the echoes of Fig. 8.5. We expect that, during the ultrafast excitation process at the sapphire-chromium

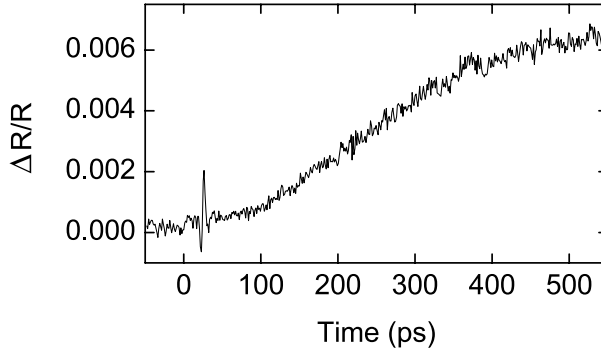


FIGURE 8.7 Long-time pump-probe reflectivity data for crystal-side pump and surface probe of a 100-nm Cr/5-nm Al film on sapphire. Wiggle at 20 ps is the coherent strain waveform, slow increase is due to heat transport through the film.

interface, the loss of volume due to the compression of the chromium lattice is compensated by an expansion of the sapphire substrate. We also observe that the width of the strain pulse in Fig. 8.6(b) for the chromium film is $\tau_g = 4.5$ ps. This value is significantly smaller than that obtained in Fig. 8.5, and may be explained by the reduction of the optical skin depth by a factor of ~ 1.6 , due to the refractive index of the neighboring sapphire. Strikingly, the width obtained from the data of the Cr/Al film is only 3.5 ps. This difference can impossibly be due to the generation mechanism as the films are identical at the chromium-sapphire interface. We conclude that this is an artefact from the very small thickness of the Al-layer. Therefore part of the reflectivity signal is caused by the underlying chromium, that has an opposite sign of the elasto-optic coupling parameter. Unfortunately, we must conclude that the combination of two metal films with opposite sign of the elasto-optic effect does not make a good detector for strain pulses.

Finally, Fig. 8.7 shows the effect of diffusive transport of heat through the metal film, again in the configuration where the excitation takes place at the sapphire-chromium interface, and the detection is done at the thin aluminium-overlayer on top of the 100-nm chromium-film. We observe the ballistic strain wavepacket arriving at 20 ps from the initial excitation (that can be observed as a small step in the reflectivity), followed by a gradually increase due to the arrival of a high-frequency heat pulse from the excitation spot. This effect persists over the entire length of the 4-m delay line, and eventually reduces by the cooling of the metal film to its surroundings, on a time scale of microseconds (c.f. Chapters 6

and 7). The observed behavior is comparable to the behavior observed earlier after the excitation of an embedded quantum well by Baumberg *et al.* [18].

8.5 Conclusions and Prospects

Extensive attempts to observe the strain pulses after propagation over long distances in sapphire did not yield any positive results up to now. One may wonder why nothing could be observed and ask whether there is any technical or fundamental reason for the signal to remain hidden. To find a small, strain-induced signal of picosecond duration after tens of nanoseconds delay requires both a good spatial and temporal overlap between the optical probe pulses and the acoustic wavepackets. The spatial overlap seems not the problem, as the acoustic beam is of the order of millimeters in diameter. The time delay for synchronization of the arrival of the soliton and the probe pulses is more difficult to find, but can generally be estimated within 1 ns using a fast photodetector and an oscilloscope.

There are some additional effects that will affect the visibility of the wavepackets after long-distance propagation. For the N-wave, it is seen that the reflectivity peaks at the steep fronts and remains low in between. At elevated temperatures, the fronts smear out and thus the reflectivity signal will also become flatter. Considering the strain soliton, it is narrow with respect to the optical skin depth, and therefore its induced signal will be lower than that of a broader pulse by the ratio of its width to the width of the response function. A 0.2-ps strain soliton will in the chromium be only 1.2 nm wide, which is on the scale of the interatomic distance and particularly of surface corrugations. Inevitably this will cause small fluctuations in the arrival time due to the surface roughness. Further, the material nanostructure may have a large effect on the observed signal. The reflectivity signal is bipolar and mirror-symmetric and will therefore tend to average out under the effect of time fluctuations. That is, if the solitons manage to enter the metal film anyway. Even for a very well polished sapphire plate, the simple impedance law will not apply to THz phonons, that will scatter diffusively from this interface (see Chapter 7) rather than transmit into the metal film. It may therefore well be that below a certain limit, ultrashort strain solitons cannot be detected using pump-probe reflectometry on a metallic transducer.

If the above argument is true, we may have to consider alternative methods of detecting ultrashort strain pulses in the time-domain. One avenue that will suffer less from the limitations of material roughness is the use of epitaxially

grown structures. Although some things can be done using grown structures on top of very-well polished sapphire plates ('epi-grade'), the materials of choice may be silicon or gallium arsenide. One particularly promising idea is to use a two-dimensional quantum well on top of such a material as a probe for acoustic strain. It is well-known that the exciton absorption- and emission lines undergo very large frequency-shifts that are proportional to the applied strain. This would circumvent the problem of the derivative signal in the conventional reflectometry experiment, which would be extremely useful in the case of ultrashort solitons. Another method that does not suffer from this sign problem is interferometric detection of surface displacement. As this method has some contributions that are sensitive to the surface only [10], one may even try to detect the displacement of the substrate itself, without having to deposit additional layers.

References

- [1] H.-Y. Hao and H. J. Maris, *Phys. Rev. B* **64**, 064302 (2001).
- [2] C. Thomsen, H. T. Grahn, H. J. Maris, and J. Tauc, *Phys. Rev. B* **34**, 4129 (1986).
- [3] T. Saito, O. Matsuda, and O. B. Wright, *Phys. Rev. B* **67**, 205421 (2003).
- [4] B. Perrin, Private Communication.
- [5] L. Sarger et al., *J. Opt. Soc. Am.* **B11**, 995 (1994).
- [6] B. Perrin, B. Bonello, J.-C. Jeannet, and E. Romatet, *Prog. in Nat. Sc.* **S6**, 444 (1996).
- [7] O. B. Wright, B. Perrin, O. Matsuda, and V. E. Gusev, *Phys. Rev. B* **64**, 081202 (2001).
- [8] Y. Shen and P. Hess, *J. Appl. Phys.* **82**, 4758 (1997).
- [9] C. J. K. Richardson, M. J. Ehrlich, and J. W. Wagner, *J. Opt. Soc. Am.* **B16**, 1007 (1999).
- [10] D. H. Hurley and O. B. Wright, *Opt. Lett.* **24**, 1305 (1999).
- [11] M. Nikoonahad, S. Lee, and H. Wang, *Appl. Phys. Lett.* **76**, 514 (2000).
- [12] J.-Y. Duquesne and B. Perrin, *Phys. Rev. B* **68**, 134205 (2003).
- [13] B. Perrin, *Systèmes Femtosecondes* (Publications de l'Universit de Saint-Etienne, 2001), p. 65.
- [14] B. Perrin, C. Rossignol, B. Bonello, and J.-C. Jeannet, *Physica* **B263-264**, 571 (1999).
- [15] T. Saito, O. Matsuda, and O. Wright, *Physica* **B316-317**, 304 (2002).
- [16] O. B. Wright and K. Kawashima, *Phys. Rev. Lett.* **69**, 1668 (1992).
- [17] B. A. Auld, *Acoustic Fields and Waves in Solids*, vol. 1 (Robert E. Krieger Publishing Company, 1990), 2nd ed.
- [18] J. J. Baumberg, D. A. Williams, and K. Köhler, *Phys. Rev. Lett.* **78**, 3358 (1997).

APPENDIX A

NUMERICAL MODELLING OF THE KdV-BURGERS EQUATION

A.1 Introduction

The Korteweg-de Vries equation is a nonlinear partial differential equation (PDE) that is integrable, meaning that analytical solutions can be obtained for any initial value or boundary condition imposed on the system. In practice, however, solutions can be written down in concise form only for the initial stage of development of the dispersive shock front [1–5], and in the limit $t \rightarrow \infty$ [6–8] for the soliton part of the wavepacket. Closed analytical forms have not been obtained for the radiative tail, emerging from the part of the bipolar initial waveform where dispersion pulls apart the nonlinear structures. Further, at higher temperatures the role of thermal damping becomes important, leading to the combined KdV-Burgers equation, that is nonintegrable. Therefore, in this thesis it is chosen to compute the development of the initial pulse using numerical simulations of the KdV-Burgers equation.

Constructing a numerical solution for a nonlinear, dispersive wave equation with initial conditions is a specialized topic in itself. Especially the combination of a large nonlinear and small dispersive term requires a high level of stability and efficiency of the algorithm. As an example, the simulation of soliton train development over ~ 1 cm propagation distance in sapphire requires a co-moving time array of around 10^6 points, and over 10^5 iteration steps to obtain stable solutions, using the three-level time scheme of Sec. (A.2). In these extreme conditions, it is important that the scheme is fast, for example, the amount of computational effort between N^2 and N^3 operations is of order $N \approx 10^6$ for the above example. This already eliminates the most simple of PDE solving methods, namely that of brute-force inversion of the finite difference matrix (which is an N^3 -process). In the

course of this project we have tried three different implementations of nonlinear PDE-solving routines, two of them based on fast Fourier transforms (FFT) [9, 10] and one using finite difference techniques [11]. Of these, only two turned out to be stable enough at the high mesh sizes and nonlinearity under study to perform simulations. The leapfrog method of Ref. [9], due to its intrinsic unstableness as mentioned in [12, 13], turned out inappropriate for our current problem. The results of Chapter 4 were obtained using the three-level time scheme suggested by Balogh *et al.* [11]. However, the implementation by Driscoll [10], which was attempted at a later stage, turned out to be stable for courser grids ($N \approx 10^5$). In practice, this resulted in a reduction of computational effort of about a factor of 5, roughly from 96 to a more convenient 24 hours on the 833-MHz DEC-Alpha server used for the simulations. Moreover, the efficiency gain and method of implementation allowed for a simple extension to 2-dimensional problems, including the effects of diffraction. In the following two sections we will describe the two schemes into more detail.

A.2 Constant volume method, three-level time scheme

We start from the KdV-Burgers initial value problem

$$s_t - \epsilon s_{zz} + \beta s_{zzz} + \frac{\alpha}{2\rho c_0} s s_z = 0 \quad (\text{A.1})$$

$$s(z, 0) = \psi(z),$$

with definitions of nonlinearity $\alpha < 0$, dispersion $\beta > 0$ and viscosity $\epsilon > 0$ according to Chapter 2. The first step is to integrate the equation symmetrically around a grid point, resulting in

$$\int_w^e s_t dz - \epsilon s_{zz}|_w^e + \beta s_{zzz}|_w^e + \alpha/2\rho c_0 \frac{1}{2} s^2|_w^e = 0, \quad (\text{A.2})$$

Where w, e denote half the distance between subsequent points on the left ('west') and right ('east') side of the point of evaluation. The first term can be approximated to second order accuracy by polynomial fitting of the function s over three time levels:

$$\begin{aligned}
s^{(+1)} &= a(+1)^2 + b(+1) + c \\
s^{(0)} &= c \\
s^{(-1)} &= a(-1)^2 + b(-1) + c .
\end{aligned} \tag{A.3}$$

Solving for $\{a, b, c\}$ gives $c = s^{(0)}$, $b = (s^{(+1)} - s^{(-1)})/2$ and $a = (s^{(+1)} - 2s^{(0)} + s^{(-1)})/2$. The first order time derivative can now be approximated by filling in the constants in the polynomial expansion and evaluating at $t = 1$:

$$s_t^{(+1)} = 2a + b = (3s^{(+1)} - 4s^{(0)} + s^{(-1)})/2k , \tag{A.4}$$

where k denotes the increment in time. It should be noted that, for an implicit scheme it is important to keep as much terms as possible at the highest time level. Therefore the nonlinear part of the PDE will be approximated as

$$\frac{1}{2}s_w^{2|e} = \frac{1}{2}u^{n+1}u_w^{n|e} . \tag{A.5}$$

The spatial derivatives are calculated using the common discretization at the highest time level. Note that the integration takes place around the grid points i , therefore the evaluation takes place at positions $w = (s_i + s_{i-1})/2$ and $e = (s_{i+1} - s_i)/2$ [12], resulting in the difference equation

$$\begin{aligned}
h \frac{3s^{n+1} - 4s^n + s^{n-1}}{k} - \epsilon \frac{s_{i+1}^{n+1} - 2s_i^{n+1} + s_{i-1}^{n+1}}{h} + \beta \frac{s_{i+2}^{n+1} - 2s_{i+1}^{n+1} + 2s_{i-1}^{n+1} - s_{i-2}^{n+1}}{2h^2} \\
+ \frac{\alpha}{2\rho c_0} \left(\frac{1}{8}(s_{i+1}^{n+1} + s_i^{n+1})(s_{i+1}^n + s_i^n) - \frac{1}{8}(s_i^{n+1} + s_{i-1}^{n+1})(s_i^n + s_{i-1}^n) \right) = 0 . \tag{A.6}
\end{aligned}$$

This equation can be easily rewritten in the form of a vector equation $L(\vec{S}^n)S^{n+1} = b\vec{S}^n + c\vec{S}^{n-1}$, where \vec{S} denotes the spatial grid of strain values, and $L(\vec{S}^n)$ is a band diagonal matrix containing both the linear and nonlinear finite difference terms. The initial conditions have to be applied via two initial state vectors, $\vec{S}^{n=0}$ and $\vec{S}^{n=1}$. The latter may be estimated using a simple Euler-forward iteration, or with small enough time steps can even be set to $\vec{S}^{n=1} = \vec{S}^{n=0}$. The solution of the matrix equation can be done efficiently using standard inversion algorithms for sparse matrices [14], that use order N^2M operations, with N the number of points in the mesh and M the width of the band in the matrix ($M = 5$ in our system).

A.3 Fourth-order composite Runge-Kutta algorithm

The other approach for solving the KdV-Burgers initial value problem is considerably more involved than the finite volume scheme of Sec. A.2, but is far more stable and efficient. The method, developed by Driscoll [10, 13] is built around a fourth-order Runge-Kutta scheme in Fourier domain, with a spectral decomposition into 'slow' and 'stiff' modes. The philosophy behind this approach is, that the highest order derivatives, that require the finest grid for stability, are all contained in the linear part of the PDE. Therefore, the equation is separated into linear and nonlinear operators as follows

$$s_t(z, t) = N(s) + Ls(z, t) , \quad (\text{A.7})$$

with $N(s)$ and L the nonlinear and linear operators, respectively. One can choose to solve these terms either in real-space or Fourier domain on an individual basis. A useful choice for our situation is the evaluation of the nonlinear term in spatial domain and the linear term in spectral domain. This yields the following equation

$$\tilde{s}_t(\xi, t) = i\xi F[(F^{-1}\tilde{s})^2] + \tilde{\lambda}(k)\tilde{s} . \quad (\text{A.8})$$

Here we have considered again the array of space-points of the strain as a vector \vec{s} , with Fourier transform \tilde{s} . ξ denotes the wavevector and $\tilde{\lambda}$ is a diagonal matrix containing the (complex) eigenvalues of the linear operator. For the KdV-Burgers equation, these are given by

$$\tilde{\lambda} = -\epsilon\xi^2 - i\beta\xi^3 . \quad (\text{A.9})$$

We now proceed with the splitting of the spectrum into slow and stiff modes and evolve them using their own particular schemes: and explicit, fourth order Runge-Kutta scheme for the slow modes and an implicit scheme for the stiff modes. The former, explicit scheme is less consuming but has also limited stability, while the implicit method has high stability but requires additional matrix multiplications. We proceed by writing for the two different subsystems the PDE in the form

$$\begin{aligned} \dot{\tilde{y}} &= \tilde{f}(\tilde{y}, \tilde{z}) + \tilde{\lambda}\tilde{y} \\ \dot{\tilde{z}} &= \tilde{g}(\tilde{y}, \tilde{z}) , \end{aligned} \quad (\text{A.10})$$

Where \tilde{y} , \tilde{z} denote the stiff and slow parts of the spectrum, respectively. The functions \tilde{f} and \tilde{g} indicate the operators that are evaluated using the explicit iteration method, which for the stiff modes is the nonlinear term and for the slow modes both the linear and nonlinear operators.

The details of the implementation of implicit and explicit Runge-Kutta algorithms may be found in Driscoll [10]. We give here the resulting recipe for a single iteration step for the functions \tilde{y} and \tilde{z}

$$\begin{aligned}
Y_1 &= \tilde{y}_n \\
Z_1 &= \tilde{z}_n \\
Y_2 &= \left(1 - \frac{1}{3}k\lambda\right)^{-1} \left(\tilde{y}_n + \frac{1}{2}k\tilde{f}(Y_1, Z_1) + \frac{1}{6}k\tilde{\lambda}Y_1\right) \\
Z_2 &= \tilde{z}_n + \frac{1}{2}k\tilde{g}(Y_1, Z_1) \\
Y_3 &= (1 - k\lambda)^{-1} \left(\tilde{y}_n + \frac{1}{2}k\tilde{f}(Y_2, Z_2) + \frac{1}{2}k\tilde{\lambda}Y_1 - k\tilde{\lambda}Y_2\right) \\
Z_3 &= \tilde{z}_n + \frac{1}{2}k\tilde{g}(Y_2, Z_2) \\
Y_4 &= \left(1 - \frac{1}{3}k\lambda\right)^{-1} \left(\tilde{y}_n + k\tilde{f}(Y_3, Z_3) + \frac{2}{3}k\tilde{\lambda}Y_3\right) \\
Z_4 &= \tilde{z}_n + \frac{1}{2}k\tilde{g}(Y_3, Z_3) \\
y_{n+1} &= y_n + \frac{1}{6}k \left[\tilde{f}(Y_1, Z_1) + \tilde{f}(Y_4, Z_4) + \tilde{\lambda}(Y_1 + Y_4) \right] \\
&\quad + \frac{1}{3}k \left[\tilde{f}(Y_2, Z_2) + \tilde{f}(Y_3, Z_3) + \tilde{\lambda}(Y_2 + Y_3) \right] \\
z_{n+1} &= z_n + \frac{1}{6}k \left[\tilde{g}(Y_1, Z_1) + \tilde{g}(Y_4, Z_4) \right] + \frac{1}{3}k \left[\tilde{g}(Y_2, Z_2) + \tilde{g}(Y_3, Z_3) \right] .
\end{aligned} \tag{A.11}$$

A criterium for the spectral separation into \tilde{y} and \tilde{z} may be based on the stability range of the explicit Runge-Kutta algorithm. The definition of slow modes is given by Driscoll as the solution of the equation $|\tilde{\lambda}(k)| < 2.8c_0h/k$. In our simulations it was found that this criterium resulted in divergence of the simulated traces after $\sim 10^4$ time increments. The reason why this occurs, while Ref. [10] states that the threshold should be adequate for all situations, remains unclear at this point. It should be noted that the algorithm has not been tested before with these large grids and long simulation times. It was however found that good convergence could be obtained using the implicit RK4-scheme for all frequency components, i.e. by setting the criterium to zero.

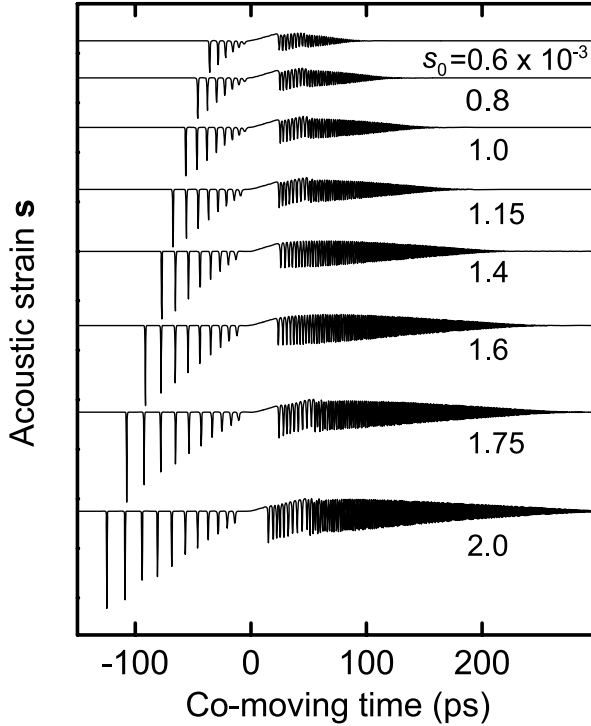


FIGURE A.1 Time-domain traces at $z = 1$ mm of the simulated acoustic wavepacket for different values of the initial strain amplitude s_0 . Results are obtained using the KdV-Burgers equation at zero damping, from the finite volume method of Sec. A.2.

A.4 Simulated wavepacket propagation in sapphire

For completeness, we show in this section the entire set of simulations at intermediate and low temperatures as obtained for comparison with the Brillouin scattering data of Chapter 4. The typical development is represented in the form of time-domain traces at a travelled distance in the crystal of $z = 1$ mm. Figure A.1 shows the simulated waveforms at different values of the initial strain amplitude s_0 , ranging between 0.6 and 2.0×10^{-3} . Scaling of the amplitude over more than a factor of 3 results in an increasing number of solitons, ranging from 6 up to 11, in the strain packet. In all traces, except the two at initial strains of 1.4 and 1.6×10^{-3} , a reflection of 10% from the chromium-sapphire interface was included in the simulation. Although one observes a difference in the leading part of the

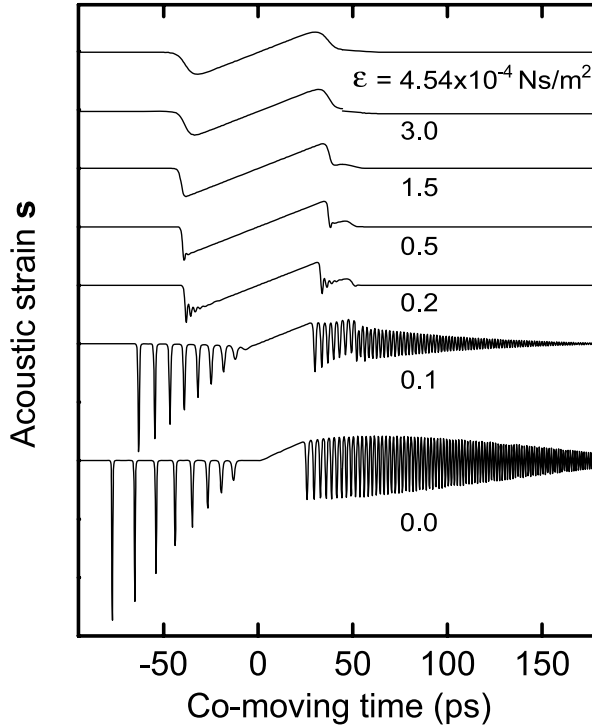


FIGURE A.2 Time-domain traces at $z = 1$ mm of the simulated acoustic wavepacket for different values of the viscosity ϵ . Results are obtained using the KdV-Burgers equation at an initial strain $s_0 = 1.4 \times 10^{-3}$, using the finite volume method of Sec. A.2.

trailing radiation between the situations with and without reflection, this has no effect in the calculated low-frequency Brillouin scattering contributions.

In another set of simulations, the value of the damping parameter ϵ is varied between 4.54×10^{-4} Ns/m², the viscosity of sapphire at room temperature, and zero. The results of these calculation a summarized in Fig. A.2, showing again the developed packets at $z = 1$ mm. One can observe clearly the transition from the overdamped to the dispersion-dominated regime, between $\epsilon = 0.1$ and 0.2×10^{-4} Ns/m². This transition region is characterized by the formation of dispersive shocks, described analytically in Refs. [1, 6]. Note that a difference exists in between the lower two simulations in Fig. A.2, which indicates that, at $\epsilon = 0.1 \times 10^{-4}$ Ns/m², the solitons can initially develop, but are attenuated upon propagation through the crystal.

References

- [1] G. B. Whitham, *Linear and Nonlinear Waves* (Wiley, 1974), 1st ed.
- [2] P. D. Lax, *Pure & Appl. Math.* **36**, 253 (1983).
- [3] P. D. Lax, *Pure & Appl. Math.* **36**, 571 (1983).
- [4] P. D. Lax, *Comm. Pure Appl. Math.* **36**, 809 (1983).
- [5] O. C. Wright, *Comm. Pure Appl. Math.* **46**, 423 (1993).
- [6] V. I. Karpman, *Non-linear waves in dispersive media* (Pergamon Press, 1975), 1st ed.
- [7] N. J. Zabusky and M. D. Kruskal, *Phys. Rev. Lett.* **15**, 240 (1963).
- [8] C. S. Gardner, J. M. Greene, M. D. Kruskal, and R. M. Miura, *Phys. Rev. Lett.* **19**, 1095 (1967).
- [9] E. Infeld, A. Senatorski, and A. A. Skorupski, *Phys. Rev. E* **51**, 3183 (1995).
- [10] T. A. Driscoll, *J. Comp. Phys.* **182**, 357 (2002).
- [11] A. Balogh and M. Krstic, *IEEE Trans. Autom. Control* **45**, 1739 (2000).
- [12] J. H. Ferziger and M. Perić, *Computational methods for fluid dynamics* (Springer Verlag, 1999), 2nd ed.
- [13] B. Fornberg and T. A. Driscoll, *J. Comp. Phys.* **155**, 456 (1999).
- [14] W. H. Press, S. A. Teukolsky, W. T. Vetterling, and B. P. Flannery, *Numerical Recipes in Fortran 77* (Cambridge University Press, 1992), 2nd ed.

APPENDIX B

TRANSITION MATRIX ELEMENT OF THE RUBY SPECTROMETER

B.1 Introduction

In this appendix we will derive the matrix element of the $\bar{E}(^2E) - 2\bar{A}(^2E)$ phonon transition used in chapters 6 and 7 for the interpretation of the phonon-induced R_2 luminescence. We will focus on the situation of uniaxial longitudinal strain along the a axis, which is the configuration that yields the strongest interaction between the longitudinal phonons and the two-level medium. The problem of phonon-induced transitions in the 2E state was addressed by Blume *et al.* [1] and Geschwind *et al.* [2] in the context of deriving a quantitative expression for the spontaneous emission lifetime T_1 from the $2\bar{A}(^2E)$ state to the metastable $\bar{E}(^2E)$ level in case of spin-flip and nonspin-flip transitions. In this derivation, static strain data on the R_1 and R_2 line positions [3] were used to estimate the off-diagonal matrix elements involved in the phonon transition.

In the derivation of the matrix element of the $\bar{E}(^2E) - 2\bar{A}(^2E)$ single-phonon transition we rely on the papers by Blume *et al.* [1]. However, we must consider that the results are all order-of-magnitude estimates, which may vary within a range of roughly a factor of 10. We may however use some of the experimental knowledge obtained by measuring the spin-flip and nonspin-flip relaxation rates which have since then become available with reasonable accuracy. This may be used to correct the expressions for the matrix elements to some extent and obtain a more reliable estimate. First, however, we will briefly review the original derivation using ligand-field theory.

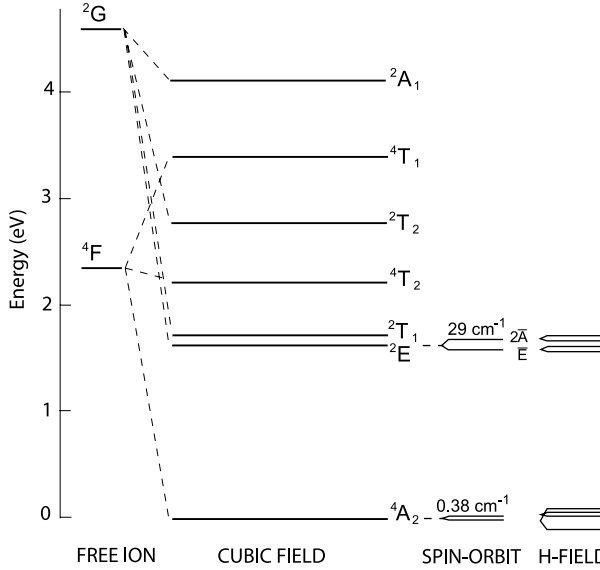


FIGURE B.1 Energy-level diagram of Cr^{3+} in the Al_2O_3 host lattice, after Ref. [4].

B.2 Ligand field calculation

In the crystal field theory of $\text{Al}_2\text{O}_3:\text{Cr}^{3+}$ one uses that the Cr^{3+} -ion is located on the trigonal axis, surrounded by an octahedron of nearest-neighbor O^{2-} ions.

It has been shown that the Hamiltonian for the d -electrons of the Cr^{3+} -ion in Al_2O_3 can be written in the form [4, 5]

$$H_{\text{tot}} = H_{\text{oct}} + H_{\text{trig}} + H_{\text{SO}} + H_{\text{strain}}. \quad (\text{B.1})$$

The first three terms correspond to the static contributions from the octahedral field, the trigonal field, and spin-orbit interactions, respectively. The trigonal and spin-orbit terms are significantly smaller than the octahedral term and may be treated as perturbations. In the following we will follow the standard group-theoretical notations for the irreducible representations of the octahedral and trigonal symmetry groups (see e.g. Refs. [6, 7] for an introduction). The three electrons that are connected to the crystal field of the lattice construct a set of states referred to as t_2^3 . In this collection of states, there are several multiplets, denoted as 4A_2 , 2E , 2T_1 , 4T_2 , 2T_2 , 4T_1 , and 2A_1 [c.f. Fig. B.1]. Within the 2E multiplet,

the spin-orbit interaction splits the levels into two Kramers doublets, $\bar{E}(^2E)$ and $2\bar{A}(^2E)$, that are the important levels of this discussion. The degeneracy of the Kramers levels may be lifted using a magnetic field, allowing for a separate study of spin-flip and nonspin-flip transitions.

The dynamic orbit-lattice interaction term H_{strain} can be expanded into the orbital operators of the irreducible representations Γ of the point group at the ion site, with the corresponding component of the dynamic strain, as [8, 9]

$$H_{\text{strain}} = \sum_{\Gamma, m} V(\Gamma, m) \epsilon(\Gamma, m), \quad (\text{B.2})$$

where $V(\Gamma, m)$ denotes the orbital operator, $\epsilon(\Gamma, m)$ the dynamic strain component, and m the number of components in the group Γ . The transition rate from $2\bar{A}$ to \bar{E} with emission of a phonon may be expressed into matrix elements of H_{strain} using the Golden Rule

$$w_{2\bar{A} \rightarrow \bar{E}} = 2\pi/\hbar \sum_{\Gamma, m} |\langle \bar{E} | V(\Gamma, m) | 2\bar{A} \rangle|^2 \times |\langle n+1 | \epsilon(\Gamma, m) | n \rangle|^2 \rho_E, \quad (\text{B.3})$$

where ρ_E denotes the density of states of the phonons at 29-cm^{-1} and the phonon occupation number n approximates zero at pumped helium temperatures. To evaluate all terms in this expression amounts to the calculation of all matrix elements of orbital operators of components (Γ, m) between the initial and final states. From the Wigner-Eckart theorem, we can factorize these matrix elements into

$$\langle \Gamma' m' | V(\Gamma, m) | \Gamma'' m'' \rangle = \Gamma^{-1/2} \langle \Gamma' | V_0(\Gamma) | \Gamma'' \rangle \langle \Gamma m | \Gamma' m' \Gamma'' m'' \rangle, \quad (\text{B.4})$$

where $V_0(\Gamma)$ denotes the reduced matrix element of the representation Γ , and the last term on the right is a Clebsch-Gordan coefficient.

In a perfect t_2^3 configuration (i.e. octahedral symmetry), the only types of vibrations of the octahedron that have to be considered are those of E and T_2 symmetry [5] (i.e. corresponding to tetragonal and rhombic distortions [10]). However, the matrix elements connecting the states in the 2E manifold via (E, T_2) symmetric vibrations turn out to be zero [1]. In order to obtain nonzero transition matrix elements, it is necessary to mix the unperturbed states by a first order contribution from spin-orbit coupling and trigonal field. More specifically, this involves the admixture of trigonal (2T_2) states into the wavefunctions, that will couple the levels to first order through T_2 symmetric vibrational modes of the oc-

tahedron (2T_1 -mixing does not provide nonzero elements up to first order [8]). First order perturbation theory leads to the following modified wavefunctions for the electronic 2E quartet [1]

$$\begin{aligned}
 |2\bar{A}'_+\rangle &= |u_+ + \frac{1}{2}\rangle + \alpha |x_+ + \frac{1}{2}\rangle - \beta |x_- - \frac{1}{2}\rangle \\
 |2\bar{A}'_-\rangle &= |u_- - \frac{1}{2}\rangle + \beta |x_+ + \frac{1}{2}\rangle + \alpha |x_- - \frac{1}{2}\rangle \\
 |\bar{E}'_+\rangle &= |u_- + \frac{1}{2}\rangle + \beta |x_0 - \frac{1}{2}\rangle - \gamma |x_- + \frac{1}{2}\rangle \\
 |\bar{E}'_-\rangle &= |u_+ - \frac{1}{2}\rangle - \gamma |x_+ - \frac{1}{2}\rangle - \beta |x_0 + \frac{1}{2}\rangle
 \end{aligned} \tag{B.5}$$

$$\alpha = \left(\frac{\zeta}{\sqrt{6}\Delta} + \frac{\sqrt{6}K}{\Delta} \right), \quad \beta = \frac{\zeta}{\sqrt{3}\Delta}, \quad \gamma = \left(\frac{\zeta}{\sqrt{6}\Delta} - \frac{\sqrt{6}K}{\Delta} \right).$$

Here u_+ and u_- denote the octahedral basis of 2E (the unperturbed wavefunctions), x_- , x_+ , and x_0 the trigonal basis of 2T_2 , K, ζ are the trigonal field and spin-orbit parameters, respectively [1, 11], and $\Delta = 6734 \text{ cm}^{-1}$ is the energy splitting between the 2E and T_2 states. Using these wavefunctions, the off-diagonal elements $\langle 2\bar{A}' | H_{\text{strain}} | \bar{E}' \rangle$ can be calculated up to first order by taking into account only matrix elements linear in the perturbation (i.e. of type $\langle u_j \pm \frac{1}{2} | \dots | x_i \pm \frac{1}{2} \rangle$). To accomplish this it is useful to write the strain Hamiltonian H_{strain} in the irreducible representations of the octahedral system [9]:

$$H_{\text{strain}} = H_{A_1} + H_E + H_{T_2}. \tag{B.6}$$

Here H_{A_1} denotes the uniform compression (diagonal) part of the Hamiltonian, that preserves octahedral symmetry and thus produces no effect in the splitting of the levels. Again, also the matrix element coupling the trigonal 2T_2 electronic states to the 2E -manifold via the group of E -vibrations is zero [8], which leaves only the term H_{T_2} in Eq. (B.6) to be considered. By using Eq. (B.4), one can simply evaluate the remaining matrix elements in terms of the Clebsch-Gordan coefficients connecting the E to the 2E and 2T_2 basis sets (that can be found in the tables of Ref. [8]), in combination with a reduced matrix element $V(T_2)$. Eventually this results in the expression for the nonspin-flip transitions

$$\langle \bar{E}'_{+-} | H_{T_2} | 2\bar{A}'_{+-} \rangle = -\frac{2K}{\Delta} V(T_2) s_+ = -Q s_+. \tag{B.7}$$

with the abbreviation $Q = \frac{2K}{\Delta} V(T_2)$. The parameter s_+ denotes the component of the applied strain in the corresponding x_+ -mode of the T_2 -basis. The reduced

matrix element $V(T_2)$ has been obtained from experimental data for the $\bar{E} - 2\bar{A}$ -level splitting for strain along the c axis. The strain-induced change in $R_2 - R_1$ -splitting was measured to be $0.55 \text{ cm}^{-1}/\text{GPa}$ in static strain experiments [3, 12], and $0.44 \text{ cm}^{-1}/\text{GPa}$ in shock wave experiments [10]. Following the argumentation by Blume *et al.* [1], this yields a value for $V(T_2) \approx 2.4 \times 10^4 \text{ cm}^{-1}$ per unit of trigonal strain. The magnitude of s_+ can be derived simply from the uniaxial strain s by transforming to a trigonal basis, leading to [10]

$$s_+(T_2) = \frac{1 - i\sqrt{3}}{4} \frac{s}{3}, \quad (\text{B.8})$$

where the complex nature of the strain is a consequence of the mathematical construction. For applied stress along the c -axis, the transformation to trigonal strain components yields $s_+ = 0$ [9, 10], which explains the zero coupling of longitudinal phonons in this crystallographic direction, as observed in Ref. [13] and by us in Chapter 7. A uniaxial strain s propagating along the a axis will thus contain a trigonal component $|s_+| = q_+ s$, with $q_+ \approx 0.29$ the reduction factor obtained from Eq. (B.8). Given the known values for the material constants $\zeta \approx 180 \text{ cm}^{-1}$ and $K \approx 250 \text{ cm}^{-1}$ [11, 14], we obtain an estimate for the matrix element for nonspin-flip transitions of

$$\left| \langle \bar{E}'_{+-} | H_{T_2} | 2\bar{A}'_{+-} \rangle \right| = \hbar \chi_0 s \approx 450 s \quad [\text{cm}^{-1}/\text{uniaxial strain}]. \quad (\text{B.9})$$

We have thus obtained an estimate of the strain coefficient χ_0 in the Rabi frequency of $\hbar \chi_0 = |Q q_+| \approx 450 \text{ cm}^{-1}$.

From the matrix element, one can obtain an estimate for the spontaneous emission lifetime and the resonant phonon mean free path. Following Geschwind *et al.* [2], one can write the transition rate $w_{2\bar{A} \rightarrow \bar{E}}$ in first order time dependent perturbation theory as

$$w_{2\bar{A} \rightarrow \bar{E}} = \frac{2\pi}{\hbar} Q^2 | \langle n+1 | s_\omega | n \rangle |^2 \rho_E. \quad (\text{B.10})$$

Using the cubic orientational average of the phonon modes introduced by Van Vleck [5], Blume *et al.* [1] arrive at an approximation for the nonspin-flip spontaneous emission rate of

$$w_{2\bar{A} \rightarrow \bar{E}} = \frac{Q^2 \omega^3}{30\pi\rho\hbar} \left(\frac{1}{c_l^5} + \frac{3}{2c_t^5} \right), \quad (\text{B.11})$$

with c_t, c_l the velocities of the transverse and longitudinal phonons, respectively. Filling in the value for $Q \approx 1600 \text{ cm}^{-1}$ yields a decay rate $w_{2\bar{A} \rightarrow \bar{E}} \approx 10^9 \text{ s}^{-1}$ or a decay time $T_1 \approx 1 \text{ ns}$.

We should realize that the above method is a very rough estimate, and that there are several assumptions made to arrive at an expression for χ_0 . The connection of the strain-dependent lineshift data with the nondiagonal matrix element $V(T_2)$ assumes that the reduced matrix element in the lineshift data is the same as that in the transition rate. Blume *et al.* [1] estimate a spin-flip transition rate which is two times smaller than the experimentally observed one. Secondly, the ratio of spin-flip to nonspin-flip rates is calculated to be 60, while experimentally this ratio is only about 15. This discrepancy is not surprising, as there is a large variation in values in the literature for the constants ζ and K , that determine this ratio [11, 14, 15]. Furthermore, Van Vleck [5] cautions that the approximation for the matrix element of lattice coordinates $\langle n+1 | s_\omega | n \rangle$ is probably the weakest link in the expression for the relaxation rates. It falsely assumes that the amplitudes of vibrations are the same for all atoms in the lattice. Therefore, we argue that the largest error may not be in the calculation of the orbital matrix element, but rather in the orientational average. Therefore, if we consider the error in the spin-flip rate to be caused by the phonon statistics, we may still identify the spin-flip matrix element with the diagonal element obtained from the lineshift data [2], and with the factor of 15 between the experimentally obtained lifetimes, we then arrive at an approximation of the nonspin-flip matrix element Q which is about 4 times larger than the spin-flip element of $\sim 200 \text{ cm}^{-1}$. Combined with the factor q_+ this yields a Rabi frequency of $\hbar\chi_0 \approx 250 \text{ cm}^{-1}$. We have chosen to use this lower estimate in the calculations of Chapters 6 and 7.

B.3 Resonant phonon mean-free path

We now present some estimates for the absorption of resonant 29-cm^{-1} phonons in the resonant medium consisting of excited Cr^{3+} -ions. The mean free path \bar{l}_r for the resonant phonons in a two-level medium excited to a concentration N^* can be derived along different paths. Our first attempt starts from the rate equations governing the equilibrium of spin and phonon baths, that are on speaking terms through the crystal-field interaction. From the principle of detailed balance for the electronic and phonon subsystems, an important relation can be derived between the spontaneous emission lifetime and the resonant absorption time $\tau_r = \bar{l}_r/c_0$,

given by [13]

$$\tau_r/T_1 = D(\omega)\Delta\omega/N^* , \quad (\text{B.12})$$

with the Debye density of states $D(\omega)\Delta\omega = V\omega^2\Delta\omega/2\pi c_0^3 \approx 3 \times 10^{16} \text{ cm}^{-3}$. This directly provides an estimate for the resonant mean free path of $\bar{l}_r \approx 0.2 \mu\text{m}$ for TA phonons at the typical $N^* = 10^{18} \text{ cm}^{-3}$ for the experiments of Chapter 6.

Another approach for the determination of the absorption length \bar{l}_r involves the solution to the coupled equations for the electronic system and the elastic continuum. Derivations for the coupled spin-phonon system have been obtained by Jacobsen and Stevens [16], Shiren [17], and recently by Tilstra *et al.* [18]. Shiren derived an explicit expression for the absorption coefficient, given by

$$\bar{l}_r^{-1} = \frac{2\pi N^* \chi_0^2 \omega T_1}{\rho \hbar c_0^3} . \quad (\text{B.13})$$

Note the analogy with the optical case [19], when replacing ϵ_0 by ρc_0^2 , and the dipole moment μ by χ_0 . Equation (B.13) results in an estimate of $\bar{l}_r \approx 2.4 \mu\text{m}$ for LA and $\bar{l}_r \approx 0.4 \mu\text{m}$ for TA phonons, at $N^* = 10^{18} \text{ cm}^{-3}$. These results compare well with those of the detailed balance equation, indicating that our estimate of the Rabi frequency is very reasonable.

References

- [1] M. Blume, R. Orbach, A. Kiel, and S. Geschwind, *Phys. Rev.* **139**, A314 (1965).
- [2] S. Geschwind, G. E. Devlin, R. L. Cohen, and S. R. Chinn, *Phys. Rev.* **137**, A1087 (1965).
- [3] A. L. Schawlow, *Advances in Quantum Electronics* (Columbia University Press, 1961), p. 50.
- [4] S. Sugano and Y. Tanabe, *J. Phys. Soc. Jpn.* **13**, 880 (1958).
- [5] J. H. van Vleck, *Phys. Rev.* **57**, 426 (1940).
- [6] L. D. Landau and E. M. Lifschitz, *Quantum Mechanics, Non-relativistic Theory* (Pergamon Press, 1965), 2nd ed.
- [7] F. A. Cotton, *Chemical Applications of Group Theory* (Wiley, 1971), 2nd ed.
- [8] Y. Tanabe and H. Kamimura, *J. Phys. Soc. Jpn.* **13**, 394 (1958).
- [9] A. L. Schawlow, A. H. Pikisis, and S. Sugano, *Phys. Rev.* **122**, 1469 (1961).
- [10] S. M. Sharma and Y. M. Gupta, *Phys. Rev. B* **43**, 879 (1991).
- [11] R. M. Macfarlane, *J. Chem. Phys.* **39**, 3118 (1963).
- [12] E. Feher and M. D. Sturge, *Phys. Rev.* **172**, 244 (1968).

-
- [13] A. A. Kaplyanskii and S. A. Basun, in *Nonequilibrium Phonons in Nonmetallic Crystals*, ed. W. Eisenmenger and A. A. Kaplyanskii (North Holland, 1986) p. 373.
 - [14] R. M. Macfarlane, *J. Chem. Phys.* **47**, 2066 (1967).
 - [15] M. H. F. Overwijk, PhD Thesis, University of Utrecht (1990).
 - [16] E. H. Jacobsen and K. W. H. Stevens, *Phys. Rev.* **129**, 2036 (1963).
 - [17] N. S. Shiren, *Phys. Rev. B* **2**, 2471 (1970).
 - [18] L. G. Tilstra, A. F. M. Arts, and H. W. de Wijn, *Phys. Rev. B* **68**, 144302 (2003).
 - [19] L. Allen and J. H. Eberly, *Optical Resonance and Two-Level Atoms* (General Publishing Company, 1987), 2nd ed.

APPENDIX C

ESTIMATES FOR THE ROLE OF THE RAREFACTION TAIL

C.1 Introduction

In the analysis of the Brillouin scattering data we have until this point assumed that the dispersive tail in the soliton wavepacket does not play a major role in the evolution of the low-frequency part of the spectrum. In Fig. 5.4(b) it was observed that the tail mainly consists of frequencies above several hundreds of gigahertz. Further, in the analysis of the strain-induced R_2 luminescence we have also considered only the excitation of TLS by the solitons in the wavepacket. In this appendix we have collected all our calculations on the contributions of the radiative tail, to show that it does not significantly contribute to either the Brillouin or the ruby experiments. The calculations support all our earlier interpretations presented in Chapters 4 to 7 in terms of the properties of the train of ultrashort strain solitons.

C.2 Brillouin scattering contributions

In this section we will compute the individual contributions of the soliton train and radiative tail to the Brillouin-scattered intensity. The shape of the dispersive tail, as shown e.g. in Fig. 5.4(a) and Fig. A.2, should not be confused with the purely linear dispersive forms of Ref. [1], where the initial pulse itself is short enough to induce dispersive spreading even in the low-amplitude regime. In the current experiments, the initial frequency components of the wavepacket are below 100 GHz, which is too low for dispersion to play a role in the linear regime within the propagation length of our crystal. The strain amplitude, however, is extremely high (up to 0.2%), ensuring a significant nonlinear steepening mechanism.

The difference in development of the compression and rarefaction parts of the

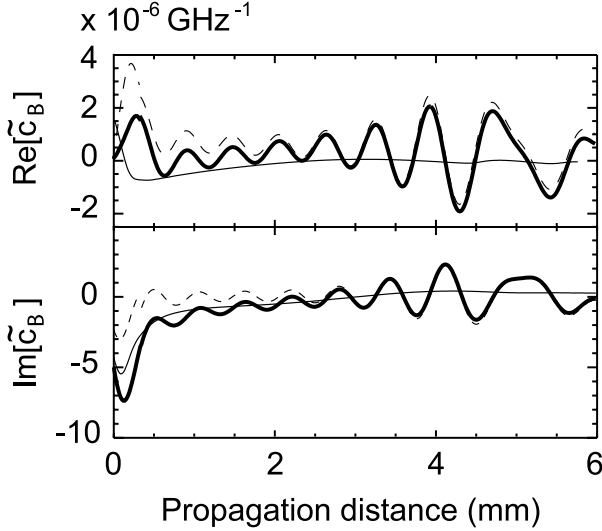


FIGURE C.1 Real and imaginary parts of Fourier component \tilde{c}_B (thick line) at the Brillouin frequency of 22 GHz, and separated into soliton (dash) and radiative tail (thin line) contributions.

bipolar strain pulse is caused only by the relative signs of the nonlinear and dispersive parts of the propagation equation. In the compressional front of the packet, nonlinearity counteracts the dispersion, leading to soliton formation, while at the tensile edge they cooperate in pulling apart the wavepacket. Only after the tail has been stretched out over an appreciable distance by dispersion, the strain amplitude decreases, and the propagation becomes approximately linear. The point at which the dispersive action becomes apparent in the self-steepening process coincides for both sides of the packet [2], leading to the same high-frequency content in the tail and in the soliton train. In contrast with the solitons, that remain nonlinear over the entire travelled distance, the stretching of the radiative tail leads to linear propagation and effectively decouples the terahertz spectrum from the low-frequency part, ‘freezing’ in the contribution of the tail in the Brillouin-scattered intensity.

To analyze the contributions to the Brillouin scattering signal in a more quantitative way, we separated a simulated wavepacket into its two basic components. The development of the soliton train and the radiative tail were individually monitored over time and their low-frequency Brillouin intensities separately com-

puted. In this procedure we considered the complete, complex form of the relevant Fourier components, to ensure that the coherent sum of the separate contributions produces the total scattered intensity. A typical evolution pattern of the Fourier coefficient of strain, \tilde{c}_B , at 22 GHz, separated into its soliton- and tail-induced components, is shown in Fig. C.1. The small discontinuity in the traces around 0.4 mm is due to the replacement beyond that point of the soliton train in the simulation by the analytical form of Ref. [2]. This procedure reduces significantly the required computational efforts without affecting the accuracy of our simulated wavepacket. From the figure, we can easily distinguish the different roles played by the soliton train and radiative tail in our Brillouin signal. The influence of the latter is limited to the first millimeter of propagation only, where the self steepening mechanism has not yet upconverted all of the acoustic energy in the tail into the terahertz range. It is not involved in the typical oscillation pattern in the Brillouin intensity, but rather yields a small additional level decreasing with distance. The oscillations in the soliton trace of Fig. C.1 can indeed be attributed purely to the spatial resonances in the train, moving at different velocities, as was stated in Chapters 4 and 5 [3].

Finally, we have analyzed the separate influence of the soliton and tail contributions in the simulated Brillouin scattering data. We find that the influence of the radiative tail is appreciable only during the first hundreds of micrometers of propagation, after which it decays rapidly to zero. This confirms the expectation, that the semi-linear trailing radiation consists mainly of components in the high-frequency part of the phonon spectrum.

C.3 TLS-excitation by the dispersive tail

In this section we calculate the excitation of the electronic two-level systems presented in Chapter 6 by the dispersive radiation in the soliton wavepacket. We once more consider a typical dispersive tail from the KdV equation, as shown in Fig. C.2(a). To investigate which part of this wavepacket is resonant with the two-level system, we calculate locally the spectrum by means of short-time Fourier transforms over a moving window of 17 ps temporal width. This results in a time-dependent spectrum, as shown in Fig. C.2(b). The time window for the transform limits the spectral resolution to ~ 60 GHz, which is small enough to distinguish some spectral features of the packet. Clearly, after the first 50 ps of the tail, that consists of some debris, the spectrum consists of a narrow band of frequencies that

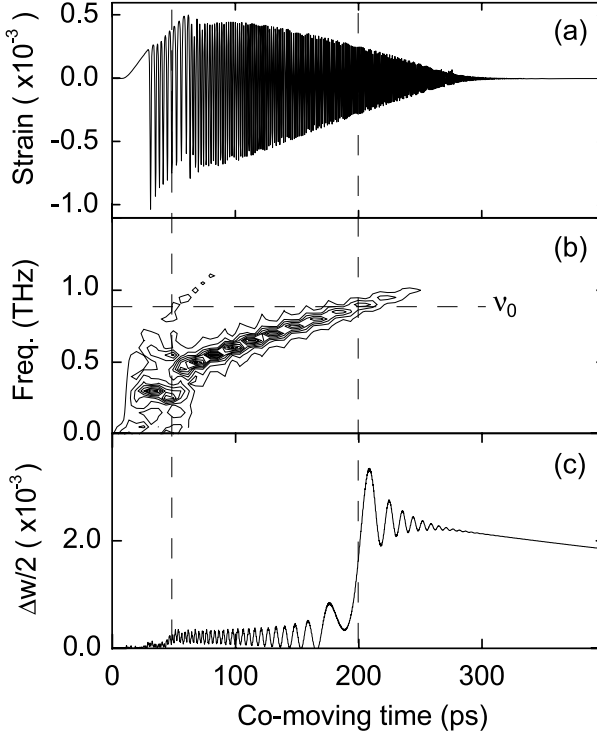


FIGURE C.2 (a) Dispersive tail at $z = 1.0$ mm propagation distance in the crystal, for an initial strain $s_0 = 1.75 \times 10^{-3}$. (b) Time-dependent Fourier transform of waveform of (a). Horizontal line (dash) denotes resonance frequency ν_0 . (c) TLS-excitation $\Delta W/2$ for the simulated wavepacket of (a). Vertical line (dash) denotes temporal position of resonance of the wavepacket.

shifts to higher frequencies towards the end of the wavepacket. This frequency-distribution over the wavepacket (or 'chirp') results from the combined action of the nonlinearity and phonon dispersion, which causes the higher frequencies to propagate slower. We can estimate the effect of linear dispersion from the difference in sound velocity $\Delta c(\omega) = c_0 - \beta\omega^2/c_0^2$, which for 0.87-THz phonons amounts to a relative velocity change of $\Delta c/c_0 = -8.9 \times 10^{-4}$. In the moving frame system, this corresponds to a walk-off of 80 ps, after propagation over 1 mm in the crystal. In Fig. C.2(b) it is observed that the position of the 0.87-THz phonons is located at 200 ps, much further than can be accounted for by linear dispersion alone. The additional walk-off can be attributed to the nonlinearity in the initial wavepacket

development, that results in quasistable nonlinear structures propagating to the right in the moving frame system.

We will leave the details of this behavior to future studies and focus now on the excitation of a two-level system by the dispersive tail. We applied the Bloch model developed in Sec. 6.3 to the wavepacket of Fig. C.2(a) and obtained the excited population $\Delta w/2$ by projection of the resulting Bloch vector on the vertical axis. The result is shown in Fig. C.2(c) and demonstrates clearly the resonant character of the interaction. The state vector starts to tilt exactly at the point where the 0.87-THz component appears in the wavepacket, as expected from the analogy with envelope waves in coherent optics [4]. Figure C.2(c) predicts excitation of the electronic system by the radiative tail up to values of $\Delta w/2 \approx 2 \times 10^{-3}$ which is of the same order of magnitude as predicted for the soliton trains of Sec. 6.3. However, there is an important effect that causes the soliton contribution to dominate in the integrated R_2 luminescence. As discussed in the previous section of this appendix, the radiative part of the wavepacket is rapidly reduced in amplitude by the spreading out of the strain over a large time window, entering the linear propagation regime. Therefore, the nonlinear refill mechanism does not work on the tail and a spectral hole will be formed like in the case of a heat pulse. Thus, after the first few resonant mean free paths, the absorption of radiation from the tail stops, while the soliton train continues to feed 29-cm^{-1} phonons via spontaneous emission to the bottlenecked phonon cloud. One may even argue to which extent these resonant phonons will be able to reach the core of the bottlenecking zone at all. It is known [5] that resonant 29-cm^{-1} -phonons will be diffusively reflected by the excited cloud of Cr^{3+} and do not contribute to the bottleneck. We conclude that coherent excitation by the radiative tail may be safely neglected with respect to the soliton train.

We finally consider the scenario in which the radiative tail grows to the extent that it contains enough resonant components to excite the Bloch vector to angles of the order of π . This situation is not purely academic, as the nonlinearity produces more and more high-frequency components in the tail when larger initial strain amplitudes are used. Thus, for some strain values exceeding the current experimental window it may well be that enough 0.87-THz components are produced to form a 2π -pulse. This pulse now would be able to propagate through the excited zone without losing its energy, i.e. the electronic state would be excited and de-excited by the same pulse. The topic of self-induced transparency or even phonon amplification in these systems will be an issue of future studies.

References

- [1] H.-Y. Hao and H. J. Maris, *Phys. Rev. B* **63**, 224301 (2001).
- [2] V. I. Karpman, *Non-linear waves in dispersive media* (Pergamon Press, 1975), 1st ed.
- [3] O. L. Muskens and J. I. Dijkhuis, *Phys. Rev. Lett.* **89**, 285504 (2002).
- [4] L. Allen and J. H. Eberly, *Optical Resonance and Two-Level Atoms* (General Publishing Company, 1987), 2nd ed.
- [5] M. J. van Dort, J. I. Dijkhuis, and H. W. de Wijn, *Phys. Rev. B* **41**, 8657 (1990).

SAMENVATTING

De experimenten in dit proefschrift houden zich bezig met geluidspulsen van extreem korte tijdsduur. Sinds enige jaren worden deze drukpakketjes met succes ingezet voor de karakterisatie van dunne lagen en nanostructuren: zij zijn in staat om door te dringen tot dieper liggende lagen, die niet direct bestudeerd kunnen worden met licht. Door middel van de weerkaatsingen van het geluidspakket aan deze structuren kan een beeld worden geconstrueerd, zoals ook gebeurt in conventionele akoestische echoscopie. De drukgolven worden gevormd door middel van de absorptie van licht in het bovenste laagje van een metaalfilm. De toepassing van extreem korte, intense laserpulsen zorgt voor een kortstondige, sterke verwarming van dit laagje, wat resulteert in een lokale vervorming van het materiaal. Deze vervorming reist vervolgens in de vorm van een drukpakket door de te bestuderen structuren.

Geluid is een golfverschijnsel, waarbij lokale dichtheidsverstoringen in een medium zich voortplanten met een eindige snelheid. De overdracht van impuls vindt plaats door middel van botsingen tussen de deeltjes, en zo kan het geluid zich voortbewegen als een rimpeling door het stilstaande medium. De frequentie, of toonhoogte, van het geluid wordt bepaald door de afstand tussen de pieken en dalen van de geluidsgolf. Indien de verstoring slechts gedurende korte tijd plaatsvindt, wordt het geluid ervaren als een knal, tik of puls. Dit komt omdat we de toonhoogte van de golf niet meer goed kunnen bepalen binnen de beperkte pulsduur. De puls bestaat dan als het ware uit een heleboel verschillende frequenties, en wordt daarom ook wel een golfpakket genoemd. Om de kortst mogelijke puls te genereren maakt het veel uit in welk materiaal het geluid zich voortbeweegt. In lucht is de afstand tussen de moleculen vrij groot en zijn de onderlinge botsingen niet zo sterk, wat leidt tot een geluidssnelheid van ‘slechts’ enkele honderden meters per seconde. In een vloeistof zitten de atomen al veel dichter op elkaar:

de geluidssnelheid is dan ook zo'n duizend meter per seconde. In een vaste stof, tenslotte, zijn de atomen zeer sterk met elkaar verbonden: hun onderlinge afstand is van de orde van 0,1 nanometer en de bijbehorende geluidssnelheid kan oplopen tot tienduizend meter per seconde voor de hardste materialen, zoals saffier en diamant.

De kortst mogelijke golf die mogelijk in een materiaal kan voorkomen wordt bepaald door de afstand tussen de atomen. Dit kan gemakkelijk worden ingezien aangezien er nooit meer dan een halve trillingsperiode tussen twee atomen kan zitten. Het ligt dan ook voor de hand dat de kortst mogelijke pulsen zich alleen kunnen voortbewegen in een vaste stof. Deze hoogfrequentie vibraties in een kristal worden ook wel fononen genoemd en vormen de basis van wat wij ervaren als warmte. Deze warmte levert echter ook een probleem op voor de drukpulsen in onze studie: de trillingen in het drukpakket worden gedempt door verstrooiingen aan de achtergrondruis van thermische fononen. Allereerst moet dus alle overtollige warmte uit het materiaal 'gevroren' worden. Dit gebeurt door het materiaal onder te dompelen in vloeibaar helium met een temperatuur van slechts enkele graden boven het absolute nulpunt. Voor de voortplanting van extreem korte pulsen is echter nog een hindernis te overwinnen: ten gevolge van interne reflecties van de golven aan het kristalrooster reizen de hoge frequenties in het golfpakket een klein beetje langzamer dan de lage frequenties. Deze zogenaamde dispersie resulteert in het langzaam uit elkaar lopen van het golfpakket tot een langgerekte structuur van langzame naar snelle trillingen. Het lijkt dus onmogelijk om zeer korte geluidspulsen stabiel te laten reizen over macroscopische afstanden.

Echter, onder de extreme omstandigheden van het beschreven experiment ontwikkelt zich nog een effect, dat kan compenseren voor dispersie. Doordat in het korte golfpakket de druk lokaal zeer hoog is, beïnvloedt de puls zelf de krachten tussen de atomen. Een andere manier om dit in te zien is om het kristal te beschouwen als een netwerk van bollen, verbonden door veertjes. Het bovenstaande argument betekent dat de stijfheid van de veertjes afhangt van de mate waarin ze samengedrukt worden. Aangezien de geluidssnelheid direct bepaald wordt door deze veerconstante, leidt dit ertoe dat de piek van de golf harder reist dan het golffront. Het pakket heeft dus de neiging om over zichzelf heen te vallen, net als een golf in de branding. In een kristal breekt de golf echter niet, omdat de atomen vast zitten op hun roosterpositie, maar er ontstaat wel een zeer steil schokfront.

De ontwikkeling van een beginpuls naar zo'n schokgolf gaat gepaard met de vorming van zeer hoge frekwenties aan het schokfront. Maar deze frekwenties reizen juist langzamer tengevolge van dispersie, waardoor het front verstoord wordt. De gecompliceerde wisselwerking van schokvorming en dispersie kan maar op één manier aflopen: de vorming van solitonen. Deze exotische objecten zijn stabiele pulsjes waarin een dynamische balans is ontstaan tussen de twee competitieve elementen van schokvorming en dispersie. Deze balans zorgt voor een ongekennde robuustheid en zelfs een regenererend vermogen van de solitonen onder invloed van externe verstoringen. Het kan worden aangetoond dat iedere willekeurige (compressieve) beginpuls in het kristal uiteindelijk opbreekt in een trein van deze solitonpakketjes, waarbij de breedte en amplitude van een soliton in deze trein uitsluitend wordt bepaald door enkele fundamentele materiaalconstanten en de maximale druk in de beginpuls.

In dit proefschrift hebben we de ontwikkeling bestudeerd van een picoseconde (pico- is 10^{-12}) drukgolf tot een trein van ultrakorte solitonen in een saffierkristal bij enkele graden boven het absolute nulpunt (-273.15 ° C). Om de pulsen te detecteren maken we gebruik van verschillende methoden. De hoofdstukken 3 t/m 5 behandelen een techniek die bekend staat als Brillouin lichtverstrooiing. Hierbij wordt licht van een welbepaalde golflengte verstrooid aan geluidsgolven in het kristal. Het drukpakket werkt eigenlijk als een reflecterend spiegelkje dat met de geluidssnelheid door het materiaal reist. Door deze snelheid krijgt het gereflecteerde licht een frekwentieverschuiving mee, analoog aan het bekende Doppler-effect. Deze verschuiving kan gebruikt worden om het licht spectraal te scheiden van de achtergrond. De intensiteit van het Brillouin-verstrooide licht kan vervolgens worden gebruikt om informatie te verkrijgen over de ontwikkeling van het golfpakket tijdens zijn reis door het saffier.

De hoofdstukken 6 en 7 laten zien wat er gebeurt als we de ultrakorte solitonen combineren met een *resonant* medium. Hiervoor maken we gebruik van een optisch gepompt robijnkristal, dat een groot aantal Cr^{3+} -centra bevat die kunnen koppelen aan het drukveld. Bij deze wisselwerking wordt een energiekwantum overgedragen van de geluidsgolf naar de elektronen in het ion. Deze koppeling is coherent, wat betekent dat er geen fase-informatie verloren gaat in de overdracht. Het ion gaat in feite meetrillen op de maat van de geluidsgolf en zendt vervolgens deze straling ook weer uit in de vorm van nieuwe drukgolven. Dit samenspel kan gebruikt worden, enerzijds om de resonante component van de solitonen te bestuderen, en anderzijds om geluidsgolven te *versterken* door middel van over-

dracht van energie vanuit het elektronische systeem naar het drukpakket. We zijn er in geslaagd om de interactie tussen de elektronen-niveau's en de solitonen in kaart te brengen. Hierbij wordt gebruik gemaakt van het feit dat, naast fonon-emissie, het aangeslagen chroom-ion ook een foton (lichtkwantum) kan uitzenden na de wisselwerking met het akoestische veld. Het blijkt dat de ionen fungeren als een absorberend medium voor een zeer smal frekwentiebandje in het spectrum van de solitonen. Echter, doordat de solitonen voortdurend regenereren, wordt de populatie binnen dit bandje telkens aangevuld vanuit de rest van het akoestische spectrum. Dit resulteert in een zeer efficiënte energieoverheveling vanuit de solitonpuls naar het elektronische niveau-systeem, en uiteindelijk in de demping van de solitonen over een afstand van enkele millimeters in het gepompte robijn.

Hoofdstuk 8 tenslotte beschrijft nog een andere methode om de korte geluidspulsen in beeld te brengen. Hierbij wordt een metaalfilm stroboscopisch belicht met een tweede laserpuls (probe), op een welgedefinieerd moment na het aanslaan van de metaalfilm met de eerste puls (pomp). Met deze pomp-probe methode kunnen zeer kleine veranderingen van de reflectie van de film worden geregistreerd, bijvoorbeeld tengevolge van een drukpakket. We hebben deze opstelling gebruikt om de precieze vorm te bepalen van de initiële drukgolf, die de basis vormt voor de experimenten in het gehele proefschrift. Als uitbreiding van de methode hebben we geprobeerd om de probe te verplaatsen naar de overkant van het kristal, om zo de gevormde solitonpuls in het tijdsdomein te registreren. Dit blijkt echter een veel moeilijker probleem, voornamelijk omdat zo'n lange reisafstand onherroepelijk leidt tot kleine variaties in de aankomsttijd. Bovendien moet dit exacte moment teruggevonden worden over een lange periode, wat gelijk staat aan het zoeken van een speld in een hooiberg. Helaas is op het moment van schrijven deze speld nog niet gevonden.

Voor de toekomst ligt de uitdaging in het vinden van toepassingen van deze ultrakorte solitonen in andere gebieden van de fysica. De zeer korte golflengte van de pulsen en hun hoge intensiteit maakt het in principe mogelijk om nanostructuren in beeld te brengen of zelfs te maken. Een andere mogelijke toepassing is het gebruiken van de ultrakorte drukpuls om dynamische, drukafhankelijke processen te bestuderen. Uiteindelijk zal de versterking van drukpuls met behulp van resonante centra kunnen leiden tot de realisatie van een fononlaser, naar analogie van de optische laser.

DANKWOORD

Voor veel lezers vormt het onderstaande stukje het leukste deel van het proefschrift. Dit is dan ook de plek voor een persoonlijke noot aan diegenen die op bijzondere wijze betrokken zijn geweest bij het onderzoek. Dit proefschrift had nooit tot stand kunnen komen zonder het geweldige enthousiasme en de begeleiding van mijn promotor, Jaap Dijkhuis. De grote mate van vrijheid die hij gaf om binnen het lab eigen paden te verkennen bood een uitdagende werksfeer en leidde soms tot verrassende resultaten. De mogelijkheid om op ieder moment binnen te lopen voor discussie maakte het vervolgens relatief makkelijk om deze data in korte tijd te verwerken tot een serie leuke artikelen. Deze efficiënte maar op zijn tijd vermoeiende werkwijze had als aangename bijkomstigheid dat al vroeg in het onderzoek de mogelijkheid bestond om in het buitenland presentaties te geven. Ik denk dat het behaalde resultaat dan ook aan alle betrokkenen voldoening heeft gegeven. Furthermore, I thank Andrey Akimov for the long-lasting collaboration and his efforts, during his visits, with the experiments and the paper on ruby. Je remercie Bernard Perrin et Fabrice Vallée pour l'invitation à visiter leurs laboratoires.

Een experimenteel onderzoek valt of staat met een goede technische ondersteuning. Gelukkig zorgden Cees de Kok en Paul Jurrius ervoor dat er steeds weer nieuwe opstellingen verzezen. Hoewel de ideeën elkaar in hoog tempo opvolgden en vaak alweer veranderden terwijl de lasers nog maar net neergezet waren, wisten zij keer op keer een verzameling oude en nieuwe spullen te combineren tot een optimaal werkend geheel. De honderden liters vloeibaar helium, in hoog tempo opgeslurpt door de cryostaat Dikke Bertha, werden altijd op tijd afgeleverd door Nico en Jan. Ik bedank hiervoor ook Johan Keijzer, die naast de cryogene zaken altijd klaar stond om verse chroomlagen op te dampen als ik ze er weer af had geschoten. Hans Gerritsen stelde ons een pulse-picker beschikbaar voor het

gebruik in de tijdsopgeloste pomp-probe experimenten. Clarien Derks bedank ik voor haar secretariële ondersteuning. Frans Wollenberg tenslotte ben ik erg erkentelijk voor zijn leerzame en gedegen aanpak, helaas moesten we zijn fenomenale kennis al kort na aanvang van het project missen.

Voor het nodige vermaak tussen de metingen door waren er natuurlijk de mede-promovendi en studenten. De versmelting van de twee groepen 'Atom Optics' en 'Ultrafast Dynamics' bleek niet te berusten op onderlinge overeenkomsten, maar verrijkte het laboratorium wel met enkele markante personen. Dries, Erik, Michiel, Carolijn, Richard en Driss zorgden gezamenlijk voor een significante verhoging van het humoristische gehalte op de gang. Natuurlijk uit ik ook bewondering voor Peter, Jitse en Frits, die dit clubje nog enigszins onder controle proberen te houden. De balans werd uitstekend in evenwicht gehouden door de mensen aan de andere kant van de gang. Jeroen, Lennart, Dima, Xinyan en Peter bedank ik dan ook voor de serieuze werkomgeving, de laatste wens ik succes met het overnemen van het roer op het solitonen-schip. De fanatieke tafeltennisduels met Robert zorgden er in ieder geval voor dat dit boekje niet nòg dikker is geworden. Dima, thanks for the many useful discussions and for being such good company on our fast journey through New Zealand.

Het aantal studenten in de vakgroep is in een paar jaar tijd flink toegenomen en dit heeft een verfrissende werking gehad. Ik bedank Gijs, Erik, Sivaji en Inge voor hun bijdrage aan de experimenten en de gezelligheid in het lab. Hil bedank ik voor het inzicht dat hij met zijn model heeft gegeven in de theorie van solitonen in meer dimensies. Het is jammer dat niet alle mooie resultaten een plaatsje in dit proefschrift hebben gekregen. Verder natuurlijk hulde aan alle studenten die hebben gezorgd voor een bruisende sfeer.

Naast het geven van werkcollege bleek het Quantum-I team, bestaande naast ondergetekende uit Sander en Duncan, een goede combinatie tijdens de A-Eskwadraat bowlingavond. Helaas is dit successteam enigszins in het slop geraakt na het laatste college. Voor de organisatie van het werkcollege, alsmede voor een van de meest cruciale beslissingen van mijn carrière, ben ik Toine Arts erg veel dank verschuldigd.

Hoewel het spartaanse leven van een promovendus niet veel ruimte overlaat, mag er af en toe ook nog ontspannen worden, variërend van fitness met de Paak tot zinloos onderuit hangen voor de buis, in de bovenste verdieping van het fraterhuis. In huize Bob is het altijd goed toeven, en vergezeld van medebari Maarten werd er menig Kolonistenavondje gelegd onder het genot van breezers en Rammstein. De

aanwezigheid van Myrene, Titia, Anne-Fleur, Gert-Paul, Solomon en vele andere oud-huisgenoten bracht de gezelligheid terug van een echt studentenhuis. Natuurlijk wil ik ook de Fraters hartelijk danken voor hun jarenlange gastvrijheid, en met name Leo Brouwers voor zijn onaflatende interesse en steun.

Een andere vorm van ontspanning is het zingen in een koor. Een redelijk constante factor waren de mensen van Capella Occento. Met name Angelique, Bregje, Barbara, Jochem, Tijmen en Chris wil ik bedanken voor alle avonturen van de afgelopen jaren. Tussendoor is er dan ook nog af en toe een Nederlands Studenten Kamerkoor, met iedere keer weer nieuwe gezichten en moderne koormuziek onder leiding van Maria. Al deze mensen vormden op hun eigen manier een radertje in het ontstaan van dit proefschrift.

Sinds de fononconferentie is een goede samenwerking ontstaan met Gijsbert op het gebied van 'losgaan'. Vergezeld van de maten, wordt hierbij tot in de kleine uurtjes doorgefeest in de betere dansgelegenheden. Gijsbert ben ik verder erkentelijk voor het zorgvuldig doorlezen en corrigeren van het manuscript. Gedanst heb ik ook met veel plezier op de wekelijkse salsa-feesten, waarbij ik met name Els, Femke en Ilse waardeer voor hun trouwe aanwezigheid en enthousiasme.

Tenslotte bedank ik natuurlijk mijn paranimfen, Margrit en Suzanne, voor hun belangrijke bijdrage. Mijn ouders bedank ik voor hun onvoorwaardelijke steun en betrokkenheid.

PUBLICATIONS AND CONFERENCE VISITS

This thesis is based on the following publications:

- Otto L. Muskens and Jaap I. Dijkhuis, *High-amplitude, ultrashort strain solitons in sapphire*, Phys. Rev. Lett. 89(28), p. 285504 (2002)
- O. L. Muskens and J. I. Dijkhuis, *Propagation of ultrashort acoustic wave packets in PbMoO₄ studied by Brillouin spectroscopy*, Physica, **B316-317**, p. 373 (2002)
- O. L. Muskens and J. I. Dijkhuis, *Propagation and diffraction of picosecond acoustic wave packets in the soliton regime*, in *Optical Solitons: Theory and Experimental Challenges*, ed. K. Porsezian, Springer Verlag, Heidelberg, pp. 391-405 (2003)
- Otto L. Muskens, Andrey V. Akimov, and Jaap I. Dijkhuis, *Coherent interactions of terahertz strain solitons and electronic two-level systems in photoexcited ruby*, Phys. Rev. Lett. 92(3), 035503 (2004)
- O. L. Muskens, S. Purushothaman, A. V. Akimov, and J. I. Dijkhuis, *The 29-cm⁻¹ ruby phonon detector as a probe for ultrashort strain solitons*, J. Lumin. to be published (2004)
- O. L. Muskens and J. I. Dijkhuis, *Ultrashort strain soliton formation in sapphire and ruby*, J. Lumin. to be published (2004)
- Otto L. Muskens and Jaap I. Dijkhuis, *Development of trains of ultrashort strain solitons in sapphire and ruby*, Proc. SPIE to be published (2004)

Some of the work described in this thesis will be presented in the book: *Ultrafast Phenomena in Semiconductors and Nanostructures*, ed. K. T. Tsen, to be published (2005)

Parts of the work in this thesis have been presented on the following international conferences:

- 10th International Conference on Phonon Scattering in Condensed Matter, *Phonons 2001*, Hanover (NH), USA (2001)
- International Symposium on Optical Solitons: Theory and Experiments, *OSTE2002*, Cochin, India (2002) (*invited*)
- 16th International Symposium on Nonlinear Acoustics, *ISNA16*, Moscow, Russia (2002)
- International Conference on the Excited State of Solids, *DPC'03*, Christchurch, New Zealand (2003)
- Ultrafast Phenomena in Semiconductors and Nanostructures XIII, *SPIE Photonics West '04*, San Jose (CA), USA (2004) (*invited*)
- 11th International Conference on Phonon Scattering in Condensed Matter, *Phonons 2004*, St. Petersburg, Russia (2004) (*invited*)

Further, results were presented in form of oral contributions to the annual meetings of the FOM 'Werkgemeinschaft van de gecondenseerde materie', Veldhoven (2001) and (2003), and in physics colloquia given at the university 'Pierre et Marie Curie', Paris (2003) and the university of Bordeaux (2003).

CURRICULUM VITAE

De schrijver van dit proefschrift werd geboren op 3 februari 1977 te Winterswijk. Van 1988 tot 1994 doorliep hij het voorbereidend wetenschappelijk onderwijs aan de RKSG Marianum in Groenlo. Daaropvolgend studeerde hij natuurkunde aan de Universiteit Utrecht, met als keuzevakken gecondenseerde materie en theoretische fysica. Tijdens zijn afstudeerproject verrichte hij experimenteel onderzoek naar niet-evenwichts fononen in amorf silicium en de niet-lineaire optica van goudnanodeeltjes, uitgevoerd in de vakgroep ‘Ultrafast Dynamics’ onder begeleiding van prof. dr. Jaap Dijkhuis. Het doctoraalexamen Experimentele Natuurkunde werd in december 1999 behaald (met genoegen). Zijn wetenschappelijke pad werd voortgezet in dezelfde groep, als onderzoeker in opleiding bij de stichting Fundamenteel Onderzoek der Materie, waarbij hij onder meer werkte aan de ontwikkeling van ultrakorte druk-solitonen, het onderwerp van dit proefschrift. Naast het experimentele onderzoek gaf hij onderwijs aan tweede jaars studenten natuurkunde, in de vakken Optica, Quantummechanica I, Vaste Stoffysica en Thermische en Statistische Fysica. Verder begeleidde hij enkele studenten bij het verrichten van hun experimentele onderzoeksproject.